UNIVERSITÀ DELLA CALABRIA

UNIVERSITÀ DELLA CALABRIA

Dipartimento di Fisica

Dottorato di Ricerca in
Scienze e Tecnologie Fisiche, Chimiche e dei Materiali in convenzione con il CNR

CICLO
XXX

Mathematical analysis of experimental data and the existence of weak solutions in nonlinear equations

Settore Scientifico Disciplinare
FIS/02: Fisica teorica, modelli e metodi matematici

Coordinatore: Ch.mo Prof. Vincenzo Carbone

Vincenzo Carbone

Supervisore: Ch.mo Prof. Pierluigi Veltri

Pierluigi Veltri

Co-Supervisore: Dr. Raffaele Marino

Raffaele Marino

Dottorando: Dott.ssa Elisa De Giorgio

Elisa De Giorgio

Alla mia famiglia,
mia roccia e mio rifugio.

Abstract

The local emergency of *Beltrami flows* is a fundamental characteristic of the fluid turbulence dynamics (Navier-Stokes equations), where the formation of singularities starting from smooth initial data, *i.e.* the breakdown of regularity in the solutions, can individuate the onset of the turbulent behaviour. This property of nonlinear interactions has been used as a basic ingredient in the formal proof of Onsager conjecture, about the existence of weak solutions of Euler equations which do not conserve kinetic energy of the flow. The breakdown from smooth to weak solutions and the energy dissipation phenomenon can be possibly found also in magnetohydrodynamics (MHD) when progressively increasing Reynolds and magnetic Reynolds numbers. Thus a deep study of these phenomena of local formation of strong correlations between the dynamical variables of the systems could give important elements for understanding which mathematical conditions characterise the singularity emergence in weak solutions of MHD ideal case. In order to deal with these problems a multidisciplinary approach, embedding experimental data analysis and mathematical rigorous study, is needed. In this thesis both approaches have been carried out. An *ad hoc* data analysis have been identified for investigating the dynamics described by particular nonlinear partial differential equations that can generates wide modes cascades and thus turbulence (MHD equations and Hasegawa-Mima equation). In addition the problem of investigating the second order regularity of solutions to particular degenerate nonlinear elliptic equations has been discussed.

Abstract

La locale formazione dei così detti *flussi di Beltrami* rappresenta una delle caratteristiche principali della dinamica dei flussi turbolenti (equazioni di Navier-Stokes). In particolare la formazione di singolarità a partire da dati iniziali regolari (cioè la rottura della regolarità delle soluzioni) può dare inizio al comportamento turbolento nei fluidi. Tale proprietà, basata sulle interazioni non lineari, è tra i principi cardine della dimostrazione della congettura di Onsager sull'esistenza di soluzioni deboli delle equazioni di Eulero che non conservano l'energia cinetica totale del sistema.
Il passaggio da soluzioni regolari a deboli e il fenomeno di dissipazione dell'energia possono manifestarsi anche in magnetofluidodinamica (MHD), quando si ha un aumento progressivo sia dei numeri di Reynolds che dei numeri di Reynolds magnetici. Perciò uno studio approfondito di questi fenomeni, dove si ha l'insorgenza di forti correlazioni locali fra le variabili dinamiche del sistema, può fornire elementi importanti per comprendere quali condizioni matematiche caratterizzano la formazione di singolarità nelle soluzioni deboli nel caso MHD ideale. Per affrontare al meglio questi problemi è necessario un approccio multidisciplinare dove le analisi di dati sperimentali e la formulazione di una struttura matematica rigorosa coesistono.
In questo lavoro di tesi entrambi gli approcci sono stati affrontati. In particolare un'analisi dati *ad hoc* è stata costruita al fine di studiare la dinamica descritta da specifiche equazioni differenziali alle derivate parziali non lineari dove, sotto opportune ipotesi, si ha l'insorgenza di fenomeni turbolenti. Inoltre si è discusso il problema della regolarità di secondo ordine di soluzioni di particolari equazioni ellittiche degeneri non lineari.

Acknowledgements

Un sentito grazie va al mio Supervisore, Prof. Pierluigi Veltri, per avermi guidato nel mio percorso di ricerca con ottimismo trasmettendomi la sua profonda esperienza professionale ed umana.

Ringrazio il mio Supervisore, Dr. Raffaele Marino, per la sua massima disponibilità e professionalità.

Un grazie particolare va alla Prof.sa Anna Maria Canino per avermi accompagnata e seguita sin dai primi anni del mio percorso universitario con i suoi preziosi consigli.

Un ringraziamento speciale è rivolto al Prof. Berardino Sciunzi per il suo fondamentale aiuto, la sua massima disponibilità e tutto il tempo dedicatomi.

My sincere thanks also go to Dr. Nicolas Plihon and Victor Désangles for providing me the opportunity to join their highly professional team at the Laboratoire de Physique of the Ecole Normale Supérieure de Lyon, and giving me precious suggestions and help for writing this PhD thesis.

Un profondo ringraziamento va a tutta la mia famiglia, in particolar modo a mio padre, mia madre e mia sorella Raffaella. Non sarei mai riuscita a completare questo percoso senza il vostro amore e sostegno.

Ringrazio le mie dolci coinquiline Raffaella e Aida, tornare a casa ed abbracciarvi ha reso perfetta anche la giornata più dura. Vi voglio bene.

I thank with all my heart Peter, for his unconditional support and his foundational help.

Ringrazio Davide per avermi accompagnato in questi tre anni e aver sempre creduto in me.

Grazie a Massimo (Max), Vincenzo, Domenico e Giuseppe per le risate, i consigli e l'affetto di questi anni. Sono fortuata ad avere amici come voi al mio fianco.

Un particolare ringraziamento, infine, va a Maria Francesca ed Egle per esserci sempre state con il loro immenso affetto.

Contents

List of Figures

Introduction

In 1949 Onsager [114] formulated his famous conjecture according to which in incompressible fluid flows Hölder continuous weak solutions of Euler equations conserve kinetic energy only when their Hölder exponent is $\alpha > \frac{1}{3}$. A first proof of Onsager conjecture for Hölder exponent $\alpha > \frac{1}{3}$ has been given by Eyink [43], restricting however the study to a particular function class. Later Constantin *et al.* [26] have provided a complete and simplified proof extending the Eyink's results.
The case $\alpha \leqslant \frac{1}{3}$ has been an open problem since, recently, De Lellis *et al.* have provided a rigorous mathematical proof [35, 11, 12]. The given demonstration is constructive and a key role for building up an Hölder continuous (with $\alpha \leqslant \frac{1}{3}$) weak solution of Euler equation which does not verify the energy conservation relation has been played by the phenomenon of local *Beltramisation* of the flow, *i.e.* local formation of structures where velocity and vorticity field are strongly correlated. In particular the given proof is based on the construction of a sequence of Euler equations' approximated solutions which, letting the error to zero, converges to an exact solutions in the space $\mathcal{C}^0$. Meanwhile, these approximations are exact solutions of Navier-Stokes systems of equations which describe the dynamical evolution of a fluid in the presence of dissipative terms (Reynolds stress). The sequence is built up reducing progressively the dissipative terms, such that the sequence terms follow the recursive formulation

$$v_{k+1}(x,t) = v_k(x,t) + W(v_k(x,t), \mathring{\mathrm{R}}_k(x,t); \omega_k x, \omega_k t) + \text{ correction}$$

where W is a vectorial field consisting of periodic Beltrami flows in the variables (x,t) at the frequency ω_k, modulated in amplitude and phase depending on v_k and $\mathring{\mathrm{R}}_k$, and the correction term guarantees that v_{k+1} is divergence-free.
The idea of introducing at each iterating step a term formed by a superposition of Beltrami solutions weakly interacting is strictly related to the phenomenology of fluid turbulence. In fact, the local emergency of *Beltrami flows* is a fundamental characteristic of the fluid turbulence dynamics (Navier-Stokes equations), where the formation of singularities starting from smooth initial data, *i.e.* the breakdown of regularity in the solutions, can individuate the onset of the turbulent behaviour. Therefore, a deep study on the fundamental conditions that permit the formation of weak solutions in dissipative flows may give a key for better understanding the

formation and the evolution of these solutions when the dissipative terms tend to zero.

The breakdown from smooth to weak solutions and the energy dissipation phenomenon can be possibly found also in magnetohydrodynamics (MHD) when progressively increasing Reynolds and magnetic Reynolds numbers [6]. Actually the ideal MHD equations can be seen as the limit of the dissipative incompressible ones when dissipative terms tend to zero (existence of a generalised Beale-Kato-Majda theorem). In addition, properties equivalent to the Beltramisation of fluid flows could be locally observed. Thus a deep study of these phenomena where local formation of strong correlations between the dynamical variables of the systems could give important elements for understanding which mathematical conditions characterise the singularity emergence in weak solutions of MHD ideal case.

In order to deal with these problems a multidisciplinary approach is needed. In fact, it is important to combine both an experimental approach, where laboratory, numerical and even space data are analysed using refined mathematical tools, and a rigorous mathematical approach, where a strong framework is built up in order to establish the conditions that guarantee the existence and the uniqueness of weak solutions in the case of nonlinear partial differential equations.

In this thesis we have faced the two approaches. In particular, ad hoc data analysis have been identified for investigating the dynamics described by particular nonlinear partial differential equations that can generate wide modes cascades and thus turbulence (MHD equations and Hasegawa-Mima equation). In addition, the problem of investigating the second order regularity of solutions to particular degenerate nonlinear elliptic equations has been discussed.
This work is divided in three sections.
In section I we present a systematic study focused on understanding if and how phenomena similar to the local emergence of Beltrami flows in fluids occur on rapid ideal times in 2D MHD incompressible turbulent flows. This eventual occurrence is related to the development of intermittency. In particular, we want to assess in which manner the ideal quadratic invariants play a role in determining the nature of the structures produced by nonlinear interactions, by shaping these coherent structures in the very beginning of a decaying turbulence when dissipative terms have not yet developed their effects.
In section II a description of the data analysis performed on an ongoing experimental project, the Von-Kármán plasma (VKP) experiment, based in the Laboratoire de Physique at the Ecole Normale Supérieure de Lyon, is presented. In particular we want to understand how the generated plasma column behaves when plasma dynamics characterised by the presence of drift wave modes occurs for magnetic field above a certain threshold. Preliminary results are showed.
This work is the result of a collaboration between the Laboratoire de

Physique of the Ecole Normale Supérieure de Lyon and the Laboratoire de Mécanique des Fluides et d'Acoustique (LMFA) of the Ecole Centrale de Lyon.
Finally in section III we deal with both the local and global regularity theory for nonlinear degenerate elliptic equations in divergence form.

Part I

Coherent structures in MHD turbulence

Introduction

Fluid turbulence is characterised by the local emergence of *Beltrami flows*, i.e. structures where velocity and vorticity field are strongly correlated, as long as nonlinear interactions take place, producing smaller and smaller scales [106, 50, 45]. This property of nonlinear interactions has been used as a basic ingredient in the formal proof of the Onsager conjecture [114, 25], about the existence of weak solutions for Euler equations which do not conserve kinetic energy of the flow [108, 35, 11]. It is then worth investigating if a similar behaviour is found inside magnetohydrodynamic (MHD) incompressible turbulent flows in order to derive which mathematical properties characterise ideal turbulent flows, *i.e.* turbulent flows where dissipative terms tend to zero.

The formation of large scale correlated structures (*self-organization*), as the result of the relaxation processes occurring on very long times in MHD incompressible turbulent flows, has been the object of a lot of theoretical and numerical studies, which have shown that the properties of these structures could be predicted assuming that dissipative terms minimize the total energy of the turbulent flow, holding constant some ideal quadratic (rugged) invariants. In 3D these invariants are cross helicity and magnetic helicity [100, 61, 62, 93, 57, 18, 145, 137], while in 2D they are cross helicity and magnetic potential [57, 60, 120, 17, 145, 141].
The properties of the coherent structures predicted by these studies have also been observed in solar wind data [39, 61, 95, 120].
Matthaeus *et al.* [96] have shown that in both 2D and 3D incompressible MHD simulations dynamical alignment of velocity and magnetic field that occurs over rapid time scales (of the order of some eddy turnover time) [132].

The occurrence of coherent structures inside turbulence [145] has also been discussed in relation to the phenomenon of spatial intermittency [50]. Nonlinear interactions give rise to a cascade towards smaller scales which is not self similar. In particular the Probability Distribution Functions of fluctuations (of the dynamical variable) at a given length display larger and larger tails with respect to a Gaussian Distribution as the lengths become smaller and smaller. This behaviour, which has been described as multifractal [115], is now interpreted in terms of the occurrence at small scales of coherent structures, which are superposed on a background of random fluctuations [151].

In this section we present a systematic study focused on understanding if and how phenomena similar to the local emergence of *Beltrami flows* in fluids occur on rapid ideal times in 2D MHD incompressible turbulent flows. This eventual occurrence is related to the development of intermittency. In particular we want to assess in which manner the ideal quadratic invariants play a role in determining the nature of the structures produced by nonlinear interactions, by shaping these coherent structures in the very beginning of a decaying turbulence when dissipative terms have not yet developed their effects [34].

In order to give a brief introduction to the theoretical background in which MHD theory can be formulated, in Chapter 1 we present the basic properties of MHD theory obtaining MHD system of equations via a phenomenological approach, and in Chapter 2 we describe the basic phenomena of MHD turbulence, with particular attention to the phenomenon of self-organisation of turbulent flows and the appearance of intermittency.

Chapter 3 is devoted to the exposition of the wavelet analysis technique, which has been used as a fundamental tool for detecting and analysing the coherent structures that characterise intermittent turbulent flows.

Finally in Chapter 4, we present in detail the analysis performed in the case of 2D incompressible MHD turbulent system and the results obtained. To try to assess the general validity of our results, the analysis has been performed for some different simulations, varying resolution and initial parameters.

Chapter 1

Basic properties of magnetohydrodynamics

Magnetohydrodynamics (MHD) is the macroscopic theory aimed at describing the behaviour of electrically conducting fluids [7, 68]. The term macroscopic indicates that the involved spatial scales are larger than the intrinsic length scales of the plasma, which are the Debye length[1] and the Larmor radii[2] of different charged particles species [3].

In this chapter an introduction to general properties of MHD formulation is given: a derivation of the MHD equations is presented, followed by a discussion of the related conservation laws, with particular attention to the ideal invariants, *i.e.* the integral quantities that are conserved in the nondissipative (ideal) system; finally, for a better understanding of the MHD dynamic turbulence (chapter 2), the MHD system of equations is rewritten using the Elsässer fields.
All the equations presented here are in dimensional form using Gaussian units. Only in the end of the dissertation non-dimensionalisation in term of the Alfvén time is reported.

1.1 The MHD equations

The MHD equations are derived using a macroscopic formulation valid for any electrically conducting fluid. Another possible approach is through the kinematic equations for both ions and electrons [9].

[1] The Debye length is defined by $\lambda_D = \sqrt{\frac{\epsilon_0 k_B T_e}{n_e q_e^2}}$, where ϵ_0 is the permittivity of free space, k_B is the Boltzmann constant, T_e, n_e and q_e are the temperature, the density and the charge of electrons respectively.

[2] The Larmor radius (or gyroradius) is the radius of the circular motion of a charged particle in the presence of a uniform magnetic field, *i.e.* $r_g = \frac{m v_\perp}{|q| B}$ with m the mass of the charged particle, $v_\perp$ the component of the velocity perpendicular to the uniform magnetic field imposed, q the charge of the considered particle and B the module of the imposed magnetic field.

Let δV be a fluid element with mass $\rho\delta V$, where ρ is the mass density. The forces acting on the fluid element are the following.

- The thermal pressure force. Considering conditions close to local thermodynamic equilibrium valid, the pressure tensor results isotropic, *i.e.* $p_{ij} = p\delta_{ij}$ and it exerts, on the surface of the fluid element, the force
$$-\oint p \, d\boldsymbol{S} = -\delta V \nabla p \tag{1.1.1}$$
where $d\boldsymbol{S} = \mathbf{n} \, dS$ is the surface element.

- The gravitational force
$$\delta V \rho g = -\delta V \rho \nabla \phi_g \tag{1.1.2}$$
where ϕ_g indicates the gravitational potential. In this dissertation this force is usually omitted. As a matter of fact in a magnetised plasma gravity is often negligible if compared with the Lorentz force.

- The magnetic force. In an electromagnetic field, the force acting on a particle of charge q_i is the Lorentz force. Thus the force on a macroscopic fluid element is given by the sum of the forces acting on every particle, $\delta q\mathbf{E} + \delta\mathbf{J} \times \mathbf{B}/c$, where c is the speed of light in vacuum, δq is the net charge and $\delta\mathbf{J} = \mathbf{j}\delta V$ is the electric current carried by the fluid element with $\mathbf{j}$ the current density.
In dense fluids the property of quasi-neutrality is valid, *i.e.* $\delta q \simeq 0$. In fact, electrostatic field guarantees the charge neutrality over macroscopic distances. Hence the only contribution presents in the magnetic force is the macroscopic Lorentz force
$$\delta V \, \frac{1}{c} \, \mathbf{j} \times \mathbf{B} \tag{1.1.3}$$

- The viscous force. The viscosity acting on the surface of the volume element is defined by
$$\oint \boldsymbol{\sigma}^{(\mu)} \cdot d\mathbf{S} = \delta V \nabla \cdot \boldsymbol{\sigma}^{(\mu)} \tag{1.1.4}$$
where $\boldsymbol{\sigma}^{(\mu)} = \{\sigma_{ij}^{(\mu)}\}$ is the viscous-stress tensor, such that
$$\sigma_{ij}^{(\mu)} = \mu \left[(\delta_t v_j + \delta_t v_i) - \frac{2}{3}\delta_{ij} \nabla \cdot \boldsymbol{v} \right] = \mu \left(\nabla^2 \boldsymbol{v} + \frac{1}{3} \nabla \nabla \cdot \boldsymbol{v} \right) \tag{1.1.5}$$
and μ is the dynamic viscosity, which is assumed constant and can be used for defining the kinematic viscosity, $\nu = \mu/\rho$[3].

[3] Usually in real plasmas the viscous-stress tensor is not isotropic.

Thus the force balance becomes

$$\rho\frac{d\boldsymbol{v}}{dt} = \rho\left(\partial_t + \boldsymbol{v}\cdot\nabla\right)\boldsymbol{v} = -\nabla p + \frac{1}{c}\,\boldsymbol{j}\times\boldsymbol{B} + \mu\left(\nabla^2\boldsymbol{v} + \frac{1}{3}\nabla\nabla\cdot\boldsymbol{v}\right) \quad (1.1.6)$$

Equation (1.1.6) describes the equation of motion of the fluid element under study.

Ampère's law gives the relation between the current density $\boldsymbol{j}$ and the magnetic field, *i.e.* $\nabla\times\boldsymbol{B} = \frac{4\pi}{c}\boldsymbol{j}$. Here the displacement current is not included because it is a term of order $\frac{v^2}{c^2}$ with respect to the term $\nabla\times\boldsymbol{B}$ and it can be neglected in the nonrelativistic case (fluid velocity is much smaller than the light velocity). Substituting Ampère's relation in (1.1.3) we have

$$\frac{1}{c}\,\boldsymbol{j}\times\boldsymbol{B} = -\frac{1}{8\pi}B^2 + \frac{1}{4\pi}\boldsymbol{B}\cdot\nabla\boldsymbol{B} = -\nabla\cdot\mathcal{T}^M \quad (1.1.7)$$

where $\mathcal{T}^M = \{T^M_{ij}\}$ is the magnetic stress tensor, with $T^M_{ij} = \frac{1}{8\pi}B^2\delta_{ij} - \frac{1}{4\pi}B_iB_j$. Observing that the first term in the magnetic stress tensor acts as the isotropic pressure, an expression for the total pressure can be given by

$$P = p + \frac{B^2}{8\pi} \quad (1.1.8)$$

where the parameter $\beta = \frac{8\pi p}{B^2}$ identifies the strength of the magnetic field in a plasma.
Thus (1.1.6) can be rewrite as following

$$\rho\frac{d\boldsymbol{v}}{dt} = -\nabla P + \frac{1}{4\pi}\boldsymbol{B}\cdot\nabla\boldsymbol{B} + \mu\left(\nabla^2\boldsymbol{v} + \frac{1}{3}\nabla\nabla\cdot\boldsymbol{v}\right) \quad (1.1.9)$$

The dynamics of the magnetic field can be described combining Faraday's law and Ohm's law. In fact, from the first relation we have

$$\partial_t\boldsymbol{B} = -c\nabla\times\boldsymbol{E} \quad (1.1.10)$$

For a fluid at rest Ohm's law in the simplest case is $\boldsymbol{E} = \boldsymbol{j}\sigma$, where σ is the electrical conductivity. If the reference frame considered is now the laboratory one, the fluid element results moving with speed $\boldsymbol{v}$ and then the new electric field is obtained by a Galilean transformation: $\boldsymbol{E}' = \boldsymbol{E} + \boldsymbol{v}\times\boldsymbol{B}/c$; consequently the generalised Ohm's law for a conducting fluid in motion is

$$\boldsymbol{E} + \frac{1}{c}\boldsymbol{v}\times\boldsymbol{B} = \frac{1}{\sigma}\boldsymbol{j} \quad (1.1.11)$$

Using (1.1.10) and (1.1.11) under the condition of uniform conductivity it is possible to derive the following induction equation for the magnetic field

$$\partial_t\boldsymbol{B} - \nabla\times(\boldsymbol{v}\times\boldsymbol{B}) = \eta\nabla^2\boldsymbol{B} \quad (1.1.12)$$

where $\eta = \frac{c^2}{4\pi\sigma}$ is the magnetic diffusivity. In addition, for the magnetic field the relation $\nabla\cdot\boldsymbol{B} = 0$ is valid.

The mass density ρ of the fluid obeys the following continuity equation

$$\partial_t \rho + \nabla \cdot \rho \boldsymbol{v} = 0 \tag{1.1.13}$$

Hence in the case of incompressible fluids ($\nabla \cdot \boldsymbol{v} = 0$) the mass density of the fluid is constant.

In order to close the system of equations

$$\begin{aligned} &\rho \left(\partial_t + \boldsymbol{v} \cdot \nabla\right) \boldsymbol{v} = -\nabla p + \frac{1}{c}\, \boldsymbol{j} \times \boldsymbol{B} + \mu \left(\nabla^2 \boldsymbol{v} + \frac{1}{3} \nabla \nabla \cdot \boldsymbol{v}\right) \\ &\partial_t \boldsymbol{B} - \nabla \times (\boldsymbol{v} \times \boldsymbol{B}) = \eta \nabla^2 \boldsymbol{B} \\ &\partial_t \rho + \nabla \cdot \rho \boldsymbol{v} = 0 \\ &\nabla \cdot \boldsymbol{B} = 0 \end{aligned} \tag{1.1.14}$$

an expression for the pressure is needed. In the MHD formulation we assume that variations of the thermodynamic state are sufficiently fast and, on large spatial scales, the dissipative effects can be neglected. Hence using the continuity equation (1.1.13) and the condition of adiabatic changes of state the relation for the pressure is

$$\partial_t p + \boldsymbol{v} \cdot \nabla p + \gamma p \nabla \cdot \boldsymbol{v} = 0 \tag{1.1.15}$$

with $\gamma = \frac{c_p}{c_v}$ the specific heat ratio.

For fluid velocities slow compared with the propagation speed of compressible waves propagating in the same directions, a possible limiting case is incompressibility, *i.e.* $\frac{d\rho}{dt} = 0$ or equivalently $\nabla \cdot \boldsymbol{v} = 0$. In this limit it is possible to assume the density of the fluid element constant, $\rho = \rho_0$ and, by taking the curl of the equation of motion (1.1.9), we obtain the equation for the vorticity $\boldsymbol{\omega} = \nabla \times \boldsymbol{v}$

$$\partial_t \boldsymbol{\omega} + \boldsymbol{v} \cdot \nabla \boldsymbol{\omega} - \boldsymbol{\omega} \cdot \nabla \boldsymbol{v} = \frac{1}{c\rho_0} \left(\boldsymbol{B} \cdot \nabla \boldsymbol{j} - \boldsymbol{j} \cdot \nabla \boldsymbol{B}\right) + \nu \nabla^2 \boldsymbol{\omega} \tag{1.1.16}$$

Calculating the vorticity with (1.1.16), the velocity is obtained solving Poisson's equation

$$\nabla^2 \boldsymbol{v} = -\nabla \times \omega \tag{1.1.17}$$

The incompressibility condition does not imply that the pressure is only advected, because it formally indicates $\gamma \to \infty$ in (1.1.15). In fact the pressure is now no longer an independent dynamic variable and its Poisson's equation can be determined performing the divergence of the nonlinear term in (1.1.9), *i.e.*

$$\nabla^2 P = -\nabla \cdot \left(\rho_0 \boldsymbol{v} \cdot \nabla \boldsymbol{v} - \frac{1}{4\pi} \boldsymbol{B} \cdot \nabla \boldsymbol{B}\right) \tag{1.1.18}$$

Thus solving the Poisson's equation for the pressure we have a closure for the system of equations (1.1.14).

1.2 Conservation laws

Equations

$$\begin{aligned} &\rho\left(\partial_t + \boldsymbol{v}\cdot\nabla\right)\boldsymbol{v} = -\nabla P + \frac{1}{4\pi}\boldsymbol{B}\cdot\nabla\boldsymbol{B} \\ &\partial_t\boldsymbol{B} - \nabla\times(\boldsymbol{v}\times\boldsymbol{B}) = 0 \\ &\nabla\cdot\boldsymbol{v} = 0; \nabla\cdot\boldsymbol{B} = 0 \end{aligned} \tag{1.2.19}$$

represent a closed set of equations known as incompressible ideal (nondissipative) MHD. Starting with them several conservation equations for the MHD theory can be deduced. These equations place constraints on the dynamics of the fluid and can be broken only when dissipative effects are introduced.
Conservation laws permit to obtain two different classes of invariants: those involving the fluid and magnetic variables and those involving only the magnetic filed, as showed in the next paragraphs.

1.2.1 Ideal fluid invariants

Let's consider the full set of MHD equations (1.1.14).

Continuity equation (1.1.13) guarantees that the mass enclosed in a constant volume V is constant if the normal velocity at the boundary S of the volume vanishes. Thus the mass M contained in a volume $V(t)$ moving with the fluid is conserved, *i.e.*

$$\frac{dM}{dt} = \int_V \partial_t\rho\, d^3x + \int_{\partial_t V}\rho\, d^3x = 0 \tag{1.2.20}$$

The equation of motion in the ideal case allows the formulation of the following global momentum balance relation for a fixed volume V

$$\frac{d}{dt}\int_V \rho\boldsymbol{v}\, d^3x = \oint_S \left(\rho\boldsymbol{v}\boldsymbol{v} + \left(p + \frac{B^2}{2}\right)\boldsymbol{I} - \boldsymbol{B}\boldsymbol{B}\right)\cdot d\boldsymbol{S} \tag{1.2.21}$$

where $\boldsymbol{I}$ is the identity matrix. The momentum of the plasma volume V is conserved if the normals $v_n\, B_n = 0$ and $p + B^2/2 = 0$.

In the case of an isolated system and in the limit of incompressibility ($\gamma \to \infty$), the energy law can be obtained using only the momentum and magnetic field equations, obtaining

$$\frac{dE}{dt} = -\oint_S d\boldsymbol{S}\cdot\boldsymbol{\Phi}_E - \boldsymbol{D}_E \tag{1.2.22}$$

with the energy E expressed as the sum of kinetic and magnetic energies, namely

$$E = \int_V dV\left(\frac{1}{2}\rho v^2 + \frac{1}{8\pi}B^2\right) \tag{1.2.23}$$

$\boldsymbol{\Phi}_E$ the flux energy (that does not contain dissipative terms)

$$\boldsymbol{\Phi}_E = \left(\frac{1}{2}\rho v^2 + p\right)\boldsymbol{v} + \frac{1}{4\pi}\boldsymbol{B}\times(\boldsymbol{v}\times\boldsymbol{B}) \tag{1.2.24}$$

and the quantity $\boldsymbol{D}_E$ that includes the energy dissipation contribute, *i.e.*

$$\boldsymbol{D}_E = \int_V dV\left(\frac{1}{\sigma}\boldsymbol{j}^2 + \mu\,\boldsymbol{\omega}^2\right) \tag{1.2.25}$$

Therefore in the ideal case (no dissipative effects present) the total energy of the system is conserved.

Another conserved quantity, in the case of homogeneous density $\rho = \rho_0 = 1$ and incompressibility, is the cross-helicity $H_c = \int_V \boldsymbol{v}\cdot\boldsymbol{B}\,dV$. In fact for H_c we find

$$\frac{dH_c}{dt} = -\oint_S\left(\boldsymbol{v}\cdot\boldsymbol{B}\boldsymbol{v} - \frac{v^2}{2}\boldsymbol{B} + p\boldsymbol{B}\right)\cdot d\boldsymbol{S} \tag{1.2.26}$$

which vanishes if $v_n = B_n = 0$ at the boundary. It is worth noting that cross-helicity conservation corresponds, in the case of the incompressible fluids, to the conservation of the kinetic helicity $H_v = \int \boldsymbol{v}\cdot\boldsymbol{\omega}d^3x$.

1.2.2 Ideal magnetic invariants

The magnetic flux and the magnetic helicity are purely magnetic invariants.

The magnetic flux is defined as

$$\Phi = \int_S \boldsymbol{B}\cdot d\boldsymbol{S} \tag{1.2.27}$$

where the surface integral is performed across a surface $S(t)$, bounded by a closed curve $s(t)$, co-moving with the plasma.
Integrating (1.1.12) over S and applying Stokes' theorem we get

$$\int_S \partial_t\boldsymbol{B}\cdot d\boldsymbol{S} = \oint_{s(t)}(\boldsymbol{v}\times\boldsymbol{B})\cdot d\boldsymbol{s} - \frac{c}{\sigma}\oint_{s(t)}\boldsymbol{j}\cdot d\boldsymbol{s} \tag{1.2.28}$$

where

$$\oint_S(\boldsymbol{v}\times\boldsymbol{B})\cdot d\boldsymbol{s} = \oint(\boldsymbol{v}\times\boldsymbol{B})\cdot d\boldsymbol{s}dt = -\oint\boldsymbol{B}\,(\boldsymbol{v}\times d\boldsymbol{s})\,dt = \int_{dS}\boldsymbol{B}\cdot d\boldsymbol{S} \tag{1.2.29}$$

Thus the balance relation for the magnetic flux is

$$\frac{d\Phi}{dt} = \int_S \partial_t\boldsymbol{B}\cdot d\boldsymbol{S} + \oint\boldsymbol{B}\,(\boldsymbol{v}\times d\boldsymbol{s})\,dt = -\frac{c}{\sigma}\oint_{s(t)}\boldsymbol{j}\cdot d\boldsymbol{s} \tag{1.2.30}$$

and if $\sigma\to\infty$ the magnetic flux is conserved.

We observe that a flux line can be defined bending the boundary curve s along the field lines, consequently the flux conservation (1.2.30) describes

the phenomenon of field lines frozen into the plasma. Thus field lines are nothing more then flux tubes of infinitesimal diameter that, in absence of resistivity, cannot be broken but just twisted by the action of the fluid. But it is worth to observe that in macroscopic plasma processes, even in the case of small resistivity, the field topology is rarely conserved, whereas the field lines tend to break and reconnect.

The magnetic helicity is defined as

$$H_m = \int_V \boldsymbol{A} \cdot \boldsymbol{B} d\boldsymbol{V} \tag{1.2.31}$$

where $\boldsymbol{A}$ is the magnetic vector potential such that $\boldsymbol{B} = \nabla \times \boldsymbol{A}$.
Quantity (1.2.31) is considered to be a well-suited measure of the complexity characterising the magnetic field when it is moving around the plasma.

Using Faraday's law and choosing $\boldsymbol{E} = c^{-1}\partial_t \boldsymbol{A}$, we have

$$\begin{aligned} \frac{dH_m}{dt} &= \int_V \left(\partial_t \boldsymbol{A} \cdot \boldsymbol{B} + \boldsymbol{A} \cdot \partial_t \boldsymbol{B}\right) d\boldsymbol{V} = \int_V \boldsymbol{A} \cdot \nabla \times (\boldsymbol{v} \times \boldsymbol{B})\, d\boldsymbol{V} \\ &= \oint_S (\boldsymbol{A} \cdot \boldsymbol{v}\boldsymbol{B} - \boldsymbol{A} \cdot \boldsymbol{B}\boldsymbol{v}) \cdot d\boldsymbol{S} \end{aligned} \tag{1.2.32}$$

If $B_n = v_n = 0$ the previous quantity vanishes, *i.e.* the magnetic helicity conservation is obtained.

Because the quadratic quantities E, H_c and H_m are conserved if dissipative terms are neglected, as shown above, they are called ideal invariants or rugged invariants, due to their capacity to survive to any Galerkin truncation [131].
Ideal invariants have an important role also in the case of homogeneous turbulent flows, where dissipative coefficients can't be totally neglected and periodic boundary conditions are considered. In fact they can provide important informations about the dynamical evolution of real dissipative turbulence [141].

In the 2D incompressible MHD description the representative system of equations is

$$\partial_t \omega + \boldsymbol{v} \cdot \nabla \omega = \frac{1}{c\rho_0} \boldsymbol{B} \cdot \nabla j + \nu \nabla^2 \omega \tag{1.2.33}$$

$$\partial_t a + \boldsymbol{v} \cdot \nabla a = \eta \nabla^2 a \tag{1.2.34}$$

where $\boldsymbol{v}$ and $\boldsymbol{B}$ both have zero z component, a, j and ω are the z components of respectively the vector potential, the electric current density and the fluid vorticity and the stream function ϕ is such that $\omega = -\nabla^2 \phi$.
Like the 3D case, the total energy and the cross-helicity are conserved. Although, because the magnetic helicity in 2D vanishes, the correspondent ideal invariant obtained from (1.2.34) is the mean square magnetic potential

$$A^2 = \int a^2 d^2x \tag{1.2.35}$$

1.3 Linear waves

MHD systems show various types of waves, or linear modes, even in the case of incompressible limit, in contrast with the incompressible hydrodynamics case where all the perturbations can be recorded as nonpropagating vortex or eddies.

Let's consider a homogeneous plasma embedded in a homogeneous magnetic field $\boldsymbol{B}_0$ characterised by constant pressure p_0 and density ρ_0. Equations (1.1.6), (1.1.12) and (1.1.15) are considered to be in the approximation of small perturbations, *i.e.* $\tilde{p} << p_0$ and $\tilde{\boldsymbol{b}} << \boldsymbol{B_0}$ and can be linearised. Thus applying a Fourier transform in both space and time, such that $\boldsymbol{f}(\boldsymbol{x},t) = \boldsymbol{f_1} e^{i(\boldsymbol{k}\cdot\boldsymbol{x}-\omega_0 t)}$ with ω_0 the frequency and i the imaginary unit, we have

$$-i\omega_0\rho_0\boldsymbol{v}_1 = -i\boldsymbol{k}\,p_1 + \frac{1}{4\pi}(i\boldsymbol{k}\times\boldsymbol{b}_1)\times\boldsymbol{B}_0 - \mu k^2\boldsymbol{v}_1 \tag{1.3.36}$$

$$-i\omega_0\boldsymbol{B}_1 = i\boldsymbol{k}\times(\boldsymbol{v}_1\times\boldsymbol{B}_0) - \eta k^2\boldsymbol{B}_1 \tag{1.3.37}$$

$$-i\omega_0 p_1 = -i\gamma p_0\boldsymbol{k}\cdot\boldsymbol{v}_1 \tag{1.3.38}$$

The former equations give a single equation for $\boldsymbol{v}_1$ where dissipation can be neglected, *i.e.*

$$\omega_0\rho_0\boldsymbol{v}_1 = \left(\frac{\boldsymbol{B}_0\times(\boldsymbol{k}\times\boldsymbol{B}_0)}{4\pi} + \gamma p_0\boldsymbol{k}\right)\boldsymbol{k}\cdot v_1 - \frac{1}{4\pi}\boldsymbol{k}\cdot\boldsymbol{B}_0\,(\boldsymbol{k}\times\boldsymbol{v}_1)\times\boldsymbol{B}_0 \tag{1.3.39}$$

Choosing a coordinate system such that $\boldsymbol{B}_0 = B_0\boldsymbol{e}_z$ and $\boldsymbol{k} = k_\perp\boldsymbol{e}_y + k_\parallel\boldsymbol{e}_z$, equation (1.3.39) presents both longitudinal (compressible) waves, identified by the terms $\propto \boldsymbol{k}\cdot\boldsymbol{v}_1$, and transverse (shear) waves, identified instead by the term $\propto \boldsymbol{k}\times\boldsymbol{v}_1$. It can be written in the new coordinate system, with the following matrix form

$$\begin{pmatrix} \omega_0^2 - k_\parallel^2 v_A^2 & 0 & 0 \\ 0 & \omega_0^2 - k_\perp^2 c_s^2 - k^2 v_A^2 & -k_\perp k_\parallel c_s^2 \\ 0 & -k_\perp k_\parallel c_s^2 & \omega_0^2 - k_\parallel^2 c_s^2 \end{pmatrix}\begin{pmatrix} v_x \\ v_y \\ v_z \end{pmatrix} = 0 \tag{1.3.40}$$

where $v_A = B_0/\sqrt{4\pi\rho_0}$ is the Alfvén velocity, $c_s = \sqrt{\gamma p_0/\rho_0}$ is the speed of sound and $k^2 = k_\parallel^2 + k_\perp^2$. The dispersion relation of (1.3.40) is

$$\left(\omega_0^2 - k_\parallel^2 v_A^2\right)\left[\omega_0^4 - \omega_0^2 k^2(c_s^2 + v_A^2) + k^2 k_\parallel^2 c_s^2 v_A^2\right] = 0 \tag{1.3.41}$$

Hence studying the three types of eigenmodes of (1.3.40), by solving (1.3.41), we have a characterisation of the linear modes, or waves, proper of the homogeneous MHD system.

Alfvén waves: The mode

$$\omega_0^2 = \omega_A^2 = k_\parallel^2 v_A^2 \tag{1.3.42}$$

defines the shear Alfvén wave, also known as Alfvén wave. The plasma motion, $\boldsymbol{v}_1 = \{v_x, 0, 0\}$, characterising this mode is either incompressible or transverse ($\boldsymbol{k} \cdot \boldsymbol{v}_1 = 0$). The magnetic perturbation $\boldsymbol{b}_1 = \pm\sqrt{4\pi\rho_0}\boldsymbol{v}_1$ is originated by the term $\boldsymbol{B} \cdot \nabla \boldsymbol{B}$ in the Lorentz force. It corresponds to an elastic deformation of the field lines and it is perpendicular to $\boldsymbol{B}_0$ as well as to the velocity.

Magnetosonic waves: The mode

$$\omega_0^2 = \omega_f^2 = \frac{1}{2}k^2\left(v_A^2 + c_s^2 + \sqrt{\left(v_A^2 + c_s^2\right)^2 - \frac{4v_A^2 c_s^2 k_\parallel^2}{k^2}}\right) \tag{1.3.43}$$

identifies the compressional Alfvén wave, usually known as fast magnetosonic wave. This is usually a compressible motion with high frequency and phase velocity $v_A^2 \leq \left(\frac{\omega_0}{k}\right)^2 \leq v_A^2 + c_s^2$ that reaches its highest value in the case of propagation perpendicular to $\boldsymbol{B}_0$, where the mode becomes longitudinal ($\boldsymbol{v}_1 \parallel \boldsymbol{k}$). When, on the contrary, propagation is only parallel, *i.e.*

$$\omega_f^2 = \frac{1}{2}k^2\left(v_A^2 + c_s^2 + |v_A^2 + c_s^2|\right) \tag{1.3.44}$$

two different situations can be distinguished:

- the small-β case with $v_A > c_s$, where the mode becomes completely transverse and tends to merge with the Alfvén wave;

- the high-β case with $v_A < c_s$, where the mode is completely longitudinal, such that it combines with the nonmagnetic sound wave $\omega_0^2 = k^2 c_s^2$.

Slow modes: The mode

$$\omega_0^2 = \omega_s^2 = \frac{1}{2}k^2\left(v_A^2 + c_s^2 - \sqrt{\left(v_A^2 + c_s^2\right)^2 - \frac{4v_A^2 c_s^2 k_\parallel^2}{k^2}}\right) \tag{1.3.45}$$

indicates the slow magnetosonic wave or simply "slow mode". It is a compressible mode with phase velocity $0 \leq \left(\frac{\omega_0}{k}\right)^2 \leq c_s^2$. In case of perpendicular propagation a quasi-static equilibrium change is obtained, since changes of B^2 and p have opposite phase ($\frac{\delta B^2}{8\pi} = -\delta p$). For parallel propagation, instead, the upper limit of the phase velocity is reached,

$$\omega_s^2 = \frac{1}{2}k^2\left(v_A^2 + c_s^2 - |v_A^2 + c_s^2|\right) \tag{1.3.46}$$

such that for $v_A > c_s$ the mode is the nonmagnetic sound wave and for $v_A < c_s$ the mode is the Alfvén wave.

1.4 Elsässer fields and Alfvén time normalisation

In the case of an incompressible plasma motion the most important contribution among the linear modes is given by the Alfvén wave. In the presence of Alfvén waves, velocity perturbations are parallel to the magnetic ones, *i.e.* $\boldsymbol{v}_1 = \pm\frac{\boldsymbol{b}_1}{\sqrt{4\pi\rho_0}}$ and it is convenient to rewrite the MHD system of equations in terms of the so called Elsässer variables

$$\boldsymbol{z}^{\pm} = \boldsymbol{v} \pm \frac{\boldsymbol{B}}{\sqrt{4\pi\rho_0}} \tag{1.4.47}$$

We introduce for MHD equations the following normalisation with respect to the Alfvén time $\tau_A = L/v_A$:

$$\frac{t}{\tau_A} = t, \quad \frac{x}{L} = x, \quad \frac{B}{B_0} = B, \quad \frac{p}{\rho_0 v_A^2} = p \tag{1.4.48}$$

where B_0 is a typical magnetic field, L a typical scale length and $v_A = \frac{B_0}{\sqrt{4\pi\rho_0}}$ is the corresponding typical Alfvén velocity. In accordance with this normalisation the magnetic diffusivity is defined as the inverse of the Lundquist number $S = \frac{Lv_A}{\eta}$.

Thus adding (1.1.12) and (1.1.9), subtracting (1.1.12) from (1.1.9) and rewriting the resulting equations in terms of variables $\boldsymbol{z}^{\pm} = \boldsymbol{v} \pm \boldsymbol{B}$ we have

$$\begin{gathered}\partial_t \boldsymbol{z}^{\pm} + \boldsymbol{z}^{\mp} \cdot \nabla \boldsymbol{z}^{\pm} = -\nabla P + \frac{1}{2}(\nu + \eta)\nabla^2 \boldsymbol{z}^{\pm} + \frac{1}{2}(\nu - \eta)\nabla^2 \boldsymbol{z}^{\mp} \\ \nabla \cdot \boldsymbol{z}^{\pm} = 0\end{gathered} \tag{1.4.49}$$

with P the total pressure.

In case of uniform magnetic field $\boldsymbol{B}_0$ and in the absence of dissipation, equations (1.4.49) can be linearised as follows

$$\partial_t \boldsymbol{z}^{\pm} \mp \boldsymbol{B}_0 \cdot \nabla \boldsymbol{z}^{\pm} = 0 \tag{1.4.50}$$

From equation (1.4.50) we notice that the field $\boldsymbol{z}^-$ describes Alfvén waves propagating along $\boldsymbol{B}_0$ direction, $\boldsymbol{z}^-(\boldsymbol{x} - \boldsymbol{B}_0 t)$, although $\boldsymbol{z}^+$ is related to Alfvén waves propagating in direction opposite to $\boldsymbol{B}_0$ direction, $\boldsymbol{z}^+(\boldsymbol{x} + \boldsymbol{B}_0 t)$. The introduction of Elsässer variables avoids the self-coupling in the nonlinear term of (1.4.49) leaving only the cross coupling of $\boldsymbol{z}^+$ and $\boldsymbol{z}^-$.

Now the ideal fluid invariants of the MHD system are expressed as

$$\begin{aligned}E &= \frac{1}{4}\int_V dV \left[\left(\boldsymbol{z}^+\right)^2 + \left(\boldsymbol{z}^-\right)^2\right] \\ H_c &= \frac{1}{4}\int_V dV \left[\left(\boldsymbol{z}^+\right)^2 - \left(\boldsymbol{z}^-\right)^2\right].\end{aligned} \tag{1.4.51}$$

Chapter 2

Magnetohydrodynamics turbulence

Generally for nonmagnetic fluids the transition to turbulence occurs at sufficient high Reynolds numbers ($R_e > 3300$), such that the critical value which defines the transition from a laminar flow to a turbulent one is exceeded [50]. Reynold number is usually defined as

$$R_e = \frac{Lv}{\nu} \tag{2.0.1}$$

where L is a typical mean gradient scale depending on the geometry of the system, v is an average fluid velocity and ν the kinematic viscosity.
A similar behaviour is also expected for electrically conducting magnetised fluids. In this case, however, it is necessary to introduce a new quantity called Reynolds magnetic number defined as

$$R_m = \frac{Lv}{\eta} \tag{2.0.2}$$

where η is the magnetic diffusivity. In fact MHD turbulence can be generated only in case of strongly dynamic systems, namely when R_m becomes large due to big fluid velocities generated by external stirring or by the occurrence of instabilities in the flow.

The dynamical state of turbulence can be characterised using the following set of quantities: the energy content per unit volume $E \sim v_0^2 \sim B_0^2$, the energy dissipation rate $\varepsilon = -\frac{dE}{dt}$, corresponding to the energy injection rate in case of stationary turbulence, and the dissipation coefficients ν, η. Hence we define a characteristic integral scale, with typical velocity $E^{1/2}$, as $L = E^{3/2}/\varepsilon$, such that the Reynolds numbers are

$$R_e = \frac{E^2}{\nu\varepsilon}, \qquad R_m = \frac{E^2}{\eta\varepsilon} \tag{2.0.3}$$

This chapter is mainly focused on the study of regimes with high Reynold numbers, where a fully developed turbulence can be observed. One of the

most important feature of high Reynolds number turbulence is the simultaneous presence of different spatial scales starting from the large scales, of the order of the system size, down to the small scales, where dissipation takes place.

In order to understand the occurrence of turbulent behaviours in the flow dynamic, *i.e.* how random motions are generated from smooth flows, the development of singular solutions for the ideal equations and instability excitation are briefly presented.
Moreover, the phenomenon of self-organisation in turbulent flows is analysed, illustrating the connection with selective dissipation of the ideal invariants of the system that leads to the formation of large scale magnetic structures where the phenomenon of dynamical alignment is present.
Spectral properties and an introduction to the theory of intermittency are presented too.

2.1 Transition to turbulence

We are interested in showing how the passage to turbulence is related to the development of singular solutions in the ideal fluid equations, in particular how finite-time singularities take place. The way in which the ideal solutions become singular gives some informations about the spatial structures present in the dissipative formulation.
In parallel, the process of small scale generation, and thus the formation of cascade dynamics, is also related to the generation of instabilities which arise while the system evolves starting from a smooth initial state.

2.1.1 Ideal equations and formation of singularities

As described by Kolmogorov [50], turbulence is characterised by a hierarchy of spatial scales that goes down to very small eddies when high Reynolds number is considered. Moreover in turbulent flows with high Reynolds number, the energy dissipation rate is observed to be approximately independent of viscous coefficients. Thus, for ideal flows in the limit of infinite Reynolds number, it is expected that ideal fluid equations, *i.e.* Euler equations

$$\partial_t \boldsymbol{v} + \boldsymbol{v} \cdot \nabla \boldsymbol{v} = -\nabla p, \;\; \nabla \cdot \boldsymbol{v} = 0 \tag{2.1.4}$$

develop phenomena of energy dissipation and singularities in the solutions [114, 2, 135]. The breakdown of regularity of solutions can indicate the onset of turbulent behaviour.

In this context classical (regular) solutions are no longer considered and weak solutions are introduced, *i.e.* non-smooth solutions defined in the Sobolev space $H^s(\mathbb{R}^m)$, consisting of all the functions whose distributional derivatives up to order $s > 0$ are in $L^s(\mathbb{R}^m)$, and that verify the local mass and the momentum balance relations for all the test functions [42].

Qualitative arguments and numerical experiments have shown that the phenomenon of singularities in three spatial dimensions is related to the concentration of vorticity on successively smaller sets [51, 21]. In fact the Beale-Kato-Majda theorem [2] establishes that if a smooth solution loses its regularity at some time t_*, then the maximum vorticity grows without bound as the critical time t_* approaches. Therefore, it is not possible that the solution displays other types of singularities (as those in the deformation tensor) before the vorticity becomes unbounded. This result shows that the maximum norm of the vorticity is capable of controlling the breakdown of smooth solutions in the 3D Euler equations, and it represents a necessary condition for the formation of singularities starting from smooth initial data.

In 1949 Onsager [114] formulated his famous conjecture according to which, in incompressible fluid flows, Hölder continuous weak solutions of Euler equations conserve kinetic energy only when their Hölder exponent is $\alpha > \frac{1}{3}$.
In the perspective of this dissertation, the first nontrivial example of pathological weak solutions has been constructed by Scheffer [127]: a vector field $\boldsymbol{v}(\boldsymbol{x}, t) \in L^2(\mathbb{R}^2 \times \mathbb{R}; \mathbb{R}^2)$ such that $\boldsymbol{v}(\boldsymbol{x}, t) \equiv 0$ for $|x|^2 + |t|^2 > 1$, has been considered. This solution breaks both uniqueness and energy conservation; it is identically zero for $t < -1$, but after the critical time it becomes nonzero and at $t = 1$ it vanishes again. In addition the kinetic energy is a non-monotonous and unbounded function of time.
A first proof of Onsager conjecture for Hölder exponent $\alpha > \frac{1}{3}$ has been given by Eyink [43], restricting however the study to a particular function class. Later Constantin *et al.* [26] have provided a complete and simplified proof extended the Eyink's results.
The case $\alpha \leqslant \frac{1}{3}$ has been an open problem since, recently, De Lellis *et al.* have provided a rigorous mathematical proof [35, 11, 12].

The breakdown from smooth to weak solutions and the energy dissipation phenomenon can be possibly found also in magnetohydrodynamics when progressively increasing Reynolds and magnetic Reynolds numbers [6].
As a matter of fact the Beale-Kato-Majda theorem and Onsager's energy conservation theorem can be extended to the ideal MHD formulation rewriting them in term of the Elsasser variables z^+ and z^- [13]. Indeed criteria for total energy conservation and helicity conservation for weak solution of ideal equations can be obtained, and thus it can be proven that if a smooth initial weak solution leads to a singularity in a finite time t_* then

$$\int_0^{t_*} ||\boldsymbol{\omega}||_\infty + ||\boldsymbol{j}||_\infty \, dt = \infty \tag{2.1.5}$$

where $\boldsymbol{\omega}$ is the vorticity field, $\boldsymbol{j}$ is density current and $||\cdot||_\infty$ is the norm in the space L^∞.
These results can establish a way of understanding the relation between the smoothness of the velocity field and the magnetic field in the ideal case.

2.1.2 Current sheets

In terms of the Elsasser variables (1.4.47) the ideal MHD equations have the following form

$$\partial_t \boldsymbol{z}^{\pm} + \boldsymbol{z}^{\mp} \cdot \nabla \boldsymbol{z}^{\pm} = -\nabla P, \quad \nabla \cdot \boldsymbol{z}^{\pm} = 0 \tag{2.1.6}$$

Taking the curl of (2.1.6), and defining the fields $\boldsymbol{\omega}^{\pm} = \boldsymbol{\omega} \pm \boldsymbol{j}$ we have

$$\partial_t \boldsymbol{\omega}^{\pm} + \boldsymbol{z}^{\mp} \cdot \nabla \boldsymbol{\omega}^{\pm} = \boldsymbol{\omega}^{\pm} \cdot \nabla \boldsymbol{z}^{\mp} + \sum_{i=1}^{3} \nabla z_i^{\pm} \times \nabla z_i^{\mp} \tag{2.1.7}$$

Comparing Euler equations expressed in terms of the vorticity field, *i.e.*

$$\partial_t \boldsymbol{\omega} + \boldsymbol{v} \cdot \nabla \boldsymbol{\omega} = \boldsymbol{\omega} \cdot \nabla \boldsymbol{v}, \quad \nabla \cdot \boldsymbol{v} = 0 \tag{2.1.8}$$

with (2.1.7) we observe the presence of a supplementary term. The presence of this supplementary term in (2.1.7) characterises the formation or the absence of current sheets in the flow.

In the 2D case the vorticity field and the current density field only have the z component while the velocity and magnetic field both have zero z components, thus (2.1.7) becomes

$$\partial_t \omega^{\pm} + \boldsymbol{z}^{\mp} \cdot \nabla \omega^{\pm} = \sum_{i=1}^{2} \nabla z_i^{\pm} \times \nabla z_i^{\mp} \tag{2.1.9}$$

where $\boldsymbol{z}^{\pm} = \boldsymbol{e}_z \times \nabla \phi^{\pm}$, $\nabla^2 \phi^{\pm} = \omega^{\pm}$ and $\phi^{\pm} = \phi \pm \psi$, with ϕ the stream function and ψ is the z-component of the vector potential.
Numerical simulations of (2.1.9) have revealed the presence of internal structures such as filaments of current density and locally generated quadrupole-like concentrations of vorticity at small spatial scales and in the neighbourhood of an active X-type neutral point for the magnetic field [94, 98, 118]. These structures are conventionally called current sheets, though they are also the location of intense vorticity. It has been shown that in the vicinity of the sheets (2.1.9) is essentially linear, thus an exponential growth of j and ω is observed.

The 3D case presents more difficulties because the vortex stretching term $\boldsymbol{\omega}^{\pm} \cdot \nabla \boldsymbol{z}^{\mp}$ in (2.1.7) generally cannot be neglected. Now, depending on which of the two terms on the right side of (2.1.7) is dominant, it is possible to have either a finite-time singularity appearing as a filamentary structure, or the exponential temporal behaviour characterised by a sheet-like structure (*i.e.* a similar phenomenon to the 2D MHD case) [119, 63].

2.1.3 Instabilities

It has been observed that even a slowly evolving flow can be characterised by rapid dynamics, which may be able to destroy the original flow pattern.

The occurrence of this phenomenon is usually associated with the effects of instabilities in the flow, which allow the exponential growth of a disturbance imposed on a stationary state. Thereby, in nonstationary flows, instabilities play a basic role in understanding the evolution of flow dynamics.

Plasmas are known to became unstable in the presence of strong velocity, pressure or magnetic field gradients, namely when the convective transport of momentum, heat or magnetic flux exceed the corresponding diffusive transport by viscosity, thermal conduction or resistivity. In these scenarios different types of instabilities can be identified, such as: the Kelvin-Helmholtz instability, guided by velocity shears; the Rayleigh-Taylor instability, related to the buoyancy force in stratified flows; the current-driven MHD instabilities in a magnetised plasma, with particular attention to the tearing instability.

2.2 Self-organisation

By self-organisation we mean the spontaneous formation of large-scale coherent structures, *i.e.* structures that persist in their form for long times such that a time-average statistic can be applied (temporal coherence) [145, 50].
It is important to point out the spontaneity of the phenomenon. Generally, systems characterised by fully developed turbulence exhibit large-scale structures, which reflect the properties of the turbulence in action as a simply response of the system geometry. On the contrary coherent structures spontaneously arise out of homogeneous turbulence, as the result of the relaxation processes occurring on very long times in MHD incompressible turbulent flows.

2.2.1 Selective decay

Numerous theoretical and numerical studies have shown that the properties of coherent structures, typical of self-organisation phenomenon, can be predicted using the presence of several ideal invariants of the system, precisely assuming that dissipative terms minimise the total energy of the turbulent flow, holding constant some ideal quadratic (rugged) invariants proper of the system [123].

In 2D hydrodynamic turbulence, applying a classical variational principle where the kinematic energy $E = \frac{1}{2}\int_S v^2 d^2x$ is minimised while holding the enstrophy $\Omega = \frac{1}{2}\int_S \omega^2 d^2x$ constant, it can be shown that the coherent structures are large-scale vortices [97].
In the 3D case, the mean helicity $H = \frac{1}{2}\int_V \boldsymbol{v}\cdot\boldsymbol{\omega}\; d^3x$ is the ideal invariant held constant and the resultant coherent structures are the so called Beltrami flows, namely structures characterised by local dynamical alignment between the velocity and the vorticity field [58].

In three-dimensional MHD incompressible flows, three quadratic (rugged) invariants can be identified: the total energy E, the cross-helicity H_c and

the magnetic helicity H_m (see section 1.2). The corresponding conservation relations (expressed in Alfvén time units) in the case of incompressibility and periodic boundary conditions are

$$\frac{dE}{dt} = \frac{d}{dt}\frac{1}{2}\int \left(v^2 + B^2\right) dV = -\eta \int j^2 dV - \nu \int \omega^2 dV \tag{2.2.10}$$

$$\frac{dH_c}{dt} = \frac{d}{dt}\int \boldsymbol{v}\cdot\boldsymbol{B}\; dV = -(\nu+\eta)\int \boldsymbol{j}\cdot\boldsymbol{\omega}\; dV \tag{2.2.11}$$

$$\frac{dH_m}{dt} = \frac{d}{dt}\int \boldsymbol{A}\cdot\boldsymbol{B} = -\eta \int \boldsymbol{j}\cdot\boldsymbol{B}\; dV \tag{2.2.12}$$

Observing that dissipation in turbulence occurs at small scales and that dissipative terms contain different order of spatial derivatives, it is possible to have different decay rates of the ideal invariants. In particular the decay of MHD turbulence is principally governed by two selective decay processes [100, 61, 62, 93, 57, 18, 145].

Under the constraint of constant helicity, considering an open, limited and regular domain $\Omega \subset \mathbb{R}^3$ and a Lagrangian multiplier λ, turbulence may relax to a state of minimum energy described by the following variational principle

$$\delta\left(\frac{1}{2}\int_\Omega \left(v^2 + B^2\right) dV - \frac{1}{2}\lambda \int_\Omega \boldsymbol{A}\cdot\boldsymbol{B}\; dV\right) = 0 \tag{2.2.13}$$

Variation with respect to $\boldsymbol{v}$ gives $\boldsymbol{v} = 0$, while variation with respect to $\boldsymbol{A}$ gives relation

$$\nabla\times\boldsymbol{B} - \lambda\boldsymbol{B} = 0 \tag{2.2.14}$$

Therefore the minimum-energy state is represented by a λ-constant force-free field, known as the linear force-free field. The Lorentz force in this case vanishes, $\boldsymbol{j}\times\boldsymbol{B} = 0$, such that $\nabla\times\boldsymbol{B} = \lambda\boldsymbol{B}$, where λ satisfies the condition $\boldsymbol{B}\cdot\nabla\lambda = 0$.

Another process of relaxation that can occur is related to the slow decay of the cross-helicity. In fact the integral on the r.h.s. of (2.2.11) is not positive definite, thus the cross-helicity may present a slower decay with respect to the decay of the total energy. If the total energy is minimised holding the cross-helicity constant and using η as Lagrangian multiplier, the characterisation of this process is achieved imposing the following variational problem

$$\delta\left(\frac{1}{2}\int_\Omega \left(v^2 + B^2\right) dV - \eta \int_\Omega \boldsymbol{v}\cdot\boldsymbol{B}\; dV\right) = 0 \tag{2.2.15}$$

Variation with respect to $\boldsymbol{v}$ or $\boldsymbol{B}$ gives

$$\begin{aligned} \boldsymbol{v} - \eta\boldsymbol{B} &= 0 \\ \boldsymbol{B} - \eta\boldsymbol{v} &= 0 \end{aligned} \tag{2.2.16}$$

Consequently the Lagrangian multiplier satisfies $\eta^2 = 1$, such that an alignment of $\boldsymbol{v}$ and $\boldsymbol{B}$ is verified locally , *i.e.*

$$\boldsymbol{v} = \pm \boldsymbol{B} \tag{2.2.17}$$

This relaxed state is called pure Alfvénic state, because it corresponds to a finite-amplitude Alfvén wave. It also represents the final state which turbulence decays if very slow collisional diffusion is neglected. In particular it can be seen that, in both 3D and 2D case, the dynamical alignment (between $\boldsymbol{v}$ and $\boldsymbol{B}$) is a direct consequence of the MHD equations, that occurs on rapid times of the order of some eddy turnover time [96, 132].

Which of these two relaxation process prevails over the other, depends on the initial values of the cross-helicity and the magnetic helicity. In a strong helical system the relaxed state is the linear force-free state, while in case of high cross-helicity (sufficiently large initial alignment) the final state is a purely Alfvénic state.

Let us analyse the 2D MHD case, here the quadratic (rugged) invariants are the total energy E, the cross-helicity H_c and the mean square magnetic potential A^2 (see section 1.2) [57, 60, 120, 17, 145, 141]
Considering a variational principle where the total energy is minimised under the constrain of both constant cross-helicity and mean square magnetic potential, *i.e.*

$$\delta \left(\frac{1}{2} \int_\Omega \left(v^2 + B^2 \right) dV - \eta \int_\Omega \boldsymbol{v} \cdot \boldsymbol{B} \; dV - \phi \int_\Omega a^2 dV \right) = 0 \tag{2.2.18}$$

the minimum-energy state is represented by a pure Alfvénic state when the variation with respect to $\boldsymbol{v}$ is considered, and by a state characterised by the following relation, if variation with respect to a is considered, such as

$$\begin{aligned} &\boldsymbol{v} - \eta \boldsymbol{B} = 0 \\ &j - \eta \omega - 2\phi a = 0 \end{aligned} \tag{2.2.19}$$

where j is the current density and ω is the vorticity, which have both z non-zero component.
The latter relations lead to states where local alignment of $\boldsymbol{v}$ and $\boldsymbol{B}$ and of j and a occurs.

2.3 Energy spectra

In this section a brief discussion concerning the spectral properties of dissipative turbulence is presented, starting from one of the fundamental properties of fully developed turbulence: the presence of a wide spectrum of scales [111].

2.3.1 Inertial range

Fluid turbulence at high Reynolds numbers is characterised by an inertial range energy spectrum, where the inertial range is defined as

$$k_i \ll k \ll k_d \tag{2.3.20}$$

with k_i the injection range, *i.e.* the large scales where turbulence takes place and which carry most of the energy, and k_d the dissipative range made by the smallest scales. Thus a wide inertial range is obtained for large Reynolds numbers such that the ratio k_d/k_i is high.

As described by Richardson cascade [124], the turbulent energy transfer is characterised by a cascade process in the k-spectrum space (the spectral transfer occurs from k_i to larger wavenumbers), based on both the assumptions of scale-invariance within the inertial range and locality (in terms of scales) of interactions [50].

In case of isotropic turbulence the spectra are the angle-integrated spectra,

$$E_k = \int E_{\boldsymbol{k}}\, d\tilde{\Omega}_{\boldsymbol{k}}$$
$$E = \int_0^\infty E_k\, dk$$

with $E_{\boldsymbol{k}} = \frac{1}{2}\langle|\hat{\boldsymbol{v}}_{\boldsymbol{k}}|^2\rangle$ the spectral energy and $\hat{v}_{\boldsymbol{k}}$ velocity field in the Fourier space.

Let us define ε_i the energy injection rate at $k \sim k_i$, ε_t the energy transfer rate (energy flux) in the inertial range and ε_d the energy dissipation rate at $k \sim k_d$. For stationary turbulent flow and in decaying turbulence it is possible to consider $\varepsilon_i = \varepsilon_t = \varepsilon_d = \varepsilon$, and to refer to ε as the flux energy rate.

Using the locality of the transfer process and applying a scaling argument, the energy spectrum in the inertial range for the 3D Navier-Stokes equations can be obtained.
Let us assume the inertial range formed by a discrete set of scales: $k_1 < k_2 < ... < k_N$, such that a generic fluid element (eddy) v_n has size l_n, $k_n = l_n^{-1}$ and the velocity v_l is defined by the velocity difference between two points separated by a distance l:

$$v_l = \Delta v(l) = v(x+l) - v(x) \tag{2.3.21}$$

The typical distortion or turnover time of an eddy v_n is $\tau_n \simeq l_n/v_n$, and corresponds to the energy transfer time between two eddies v_n, v_{n+1}.

Using the previous relations and the constancy of the energy flux,

$$\varepsilon = \frac{E_n}{\tau_n} = cost, \;\; \varepsilon \simeq \frac{v_n^3}{l_n} \tag{2.3.22}$$

we have that

$$v_n \simeq \varepsilon^{\frac{1}{3}} l_n^{\frac{1}{3}} \tag{2.3.23}$$

And thus we obtain the famous Kolmogorov spectrum [80, 111]

$$E_k = C_K \varepsilon^{\frac{2}{3}} k^{-\frac{5}{3}} \tag{2.3.24}$$

C_K is the Kolmogorov-Obukhov constant and it can be determined applying by a dynamic theory [82].

The argument used up until now is valid only in the case of direct energy cascade. However, in the 2D case, the cumulative enstrophy $\mathbf{\Omega_k} = \frac{1}{2}\langle|\hat{\boldsymbol{\omega}}_{\boldsymbol{k}}|^2\rangle$ exhibits a direct cascade while the energy presents also an inverse cascade, thus a modification of the preceding is required.
Let η_Ω be the enstrophy flux, such that

$$\eta_\Omega = \frac{\mathbf{\Omega}_l}{\tau_l} \simeq \left(\frac{v_l}{l}\right)^2 \tau_l^{-1} \simeq \frac{v_l^3}{l^3} \tag{2.3.25}$$

Consequently the energy spectrum for 2D Navier-Stokes equations is

$$E_k \simeq \eta_\Omega^{\frac{2}{3}} k^{-3} \tag{2.3.26}$$

We observe that, if the injection wavelength is much smaller than the system size ($k_i^{-1} \ll L$), the inverse energy cascade may be effective and in this case, for $k < k_i$, the energy spectrum is the Kolmogorov one (the cascade direction does not effect the argument used in the 3D case).

Now, let us discuss about the energy spectrum in the incompressible MHD case.
Due to the Alfvén effect generated by the dynamic alignment of velocity and magnetic field (see section 2.2.1), small scales fluctuations are not globally independent, considering their strong dependence on the large scale magnetic field, and they behave approximately as Alfvén waves $\boldsymbol{z}^{\pm}$.

Let us focus on the weak velocity and magnetic field correlation case, *i.e.* $z_l^+ \simeq z_l^- \simeq v_l \simeq B_l$. The interaction time of two Alfvén wave packets v_l is much shorter than the nonmagnetic turnover time, $\tau_A \ll \tau_l$, and it can be shown that the energy transfer time becomes $t_l \simeq \tau_l^2/\tau_A$ under the latter assumptions [37].
Using this new time in (2.3.22) we have

$$\varepsilon \simeq \frac{v_l^4 \tau_A}{l^2} \tag{2.3.27}$$

which gives

$$v_l^2 \simeq (\varepsilon v_A)^{\frac{1}{2}} l^{\frac{1}{2}} \tag{2.3.28}$$

$$E_k = \tilde{C}_K (\varepsilon v_A)^{\frac{1}{2}} k^{-\frac{3}{2}} \tag{2.3.29}$$

Relation (2.3.29) represents the inertial range energy spectrum for incompressible MHD turbulence and it is called Iroshnikov-Kraichnan spectrum

[77, 81].
Compared with the Kolmogorov spectrum (2.3.24) Iroshnikov-Kraichnan spectrum is less steep, due to the presence of the factor τ_l/τ_A, and it explicitly depends not only from the energy flux ε but also on the large scale quantity $v_A = B_0$ (with B_0 the mean magnetic field).

Spectrum (2.3.29) is generally valid in the 2D and 3D case, because they both present a direct cascade. The constant $\tilde{C}_k$ is although not universal, due to its dependence on the precise definition of the average field B_0 and thus on the geometry of the large scale eddies. Under the assumption of neglected weak finite interactions between Alfvén modes of comparable scale, the individual energy contributions E_k^V and E_k^M (related to the velocity field and the magnetic field respectively) for the Alfven waves $|\boldsymbol{v}| = |\boldsymbol{B}|$ is $E_k^V = E_k^M$ [8].

2.3.2 Dissipation range

With dissipation range we indicate the set of wavenumber $k \geq k_d$ where dissipation dominates.

In case of hydrodynamic turbulence the dissipation scale $l_d = k_d^{-1}$ is individuated by the condition for which the nonlinear transfer rate equals the dissipation rate,

$$\tau_l^{-1} = \frac{v_l}{l} = \frac{\nu}{l^2} \tag{2.3.30}$$

Combining (2.3.30) with (2.3.23) we obtain the so called Kolomorov micro-scale [79], *i.e.*

$$l_d = \left(\frac{\nu^3}{\varepsilon}\right)^{\frac{1}{4}} = l_K \tag{2.3.31}$$

In the MHD turbulence formulation the Alfvén effects should be considered, because they tend to weaken then nonlinear energy transfer such that

$$\left(\frac{\tau_A}{\tau_l}\right)\tau_l^{-1} = \frac{\nu}{l^2} \tag{2.3.32}$$

Assuming $v_l \simeq B_l$ and $\nu \simeq \eta$, which imply equal dissipation contributions $\varepsilon_\eta \simeq \varepsilon_\nu$, with

$$\varepsilon = \varepsilon_\nu + \varepsilon_\eta, \quad \varepsilon_\nu = \nu \int \omega^2 d^3x, \quad \varepsilon_\eta = \eta \int j^2 d^3x$$

and using (2.3.28), the modified Kolmogorov micro-scale is

$$l_d = \left(\frac{\nu^2 v_A}{\varepsilon}\right)^{\frac{1}{3}} = \tilde{l}_K \tag{2.3.33}$$

Therefore, the energy spectrum for uncorrelated MHD turbulent description is

$$E_k = v_A \nu \hat{E}(\hat{k}), \quad \hat{k} = k\tilde{l}_K \tag{2.3.34}$$

Notice that this formulation is valid in both the inertial and the dissipation range. In the inertial range the normalised spectrum $\hat{E}(\hat{k})$ assumes the Iroshnikov-Kraichnan spectrum as limiting form,

$$\hat{E}(\hat{k}) = \tilde{C}_K \hat{k}^{-\frac{3}{2}}, \;\; \hat{k} \ll 1 \tag{2.3.35}$$

while, in the dissipation range $\hat{k} > 1$, the spectrum is expected to fall off rapidly (an exponential decay has been obtained from nuemrical simulations).

For a deeper description of the energy spectrum in MHD turbulence see [7, 144, 116].

2.4 Intermittency

As shown in section 2.2, in turbulent flows self-organisation is a spontaneous phenomenon responsible for the formation of large scale turbulent eddies formation, such that, in the inertial range, their spatial distribution looks the same on any scale level. This representation is not fully complete, it doesn't take into account the presence in the flow dynamics of small scales structures that become increasingly sparse (intermittent) with the action of turbulence.

Here the phenomenon of intermittency in turbulent flows is introduced.

2.4.1 Intermittency vs self-similarity

Generally a system is called self-similar (or scale-invariant) if it is reproducible starting from a magnification of some of its parts. Examples of self-similarity are present both in nature, where this property is locally displayed (*i.e.* at certain scale range), and in mathematical systems, where we talk of exact self-similarity (ex. Koch's snow flake, Cantor-set, Julia sets etc.).

Let's consider the Brownian motion as an example of dynamical system connected to turbulence that exhibits a continuous self-similarity. In fact the Brownian motion curve is a random function $u(t)$, that preserves its general aspects (statistical properties) independently on the curve-portion considered, as shown in Figure 2.1.

When instead the Devil's staircase function (Figure 2.2) is considered, we notice that the previous property is no longer valid. In this case the smaller the window, the more carefully it must be positioned to produce a nontrivial function: two different magnification windows show two completely different behaviours of the function.

This function exhibits an example of intermittent behaviour: the fluctuations of a considered function do not show a statistical uniform distribution on a certain scale, but become increasingly sparse in time (or space) with decreasing scale size.

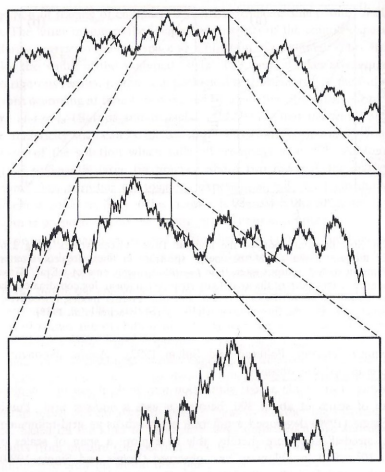

Figure 2.1: Portion of the Brownian motion curve and two successive magnifications, illustrating its self-similarity [50].

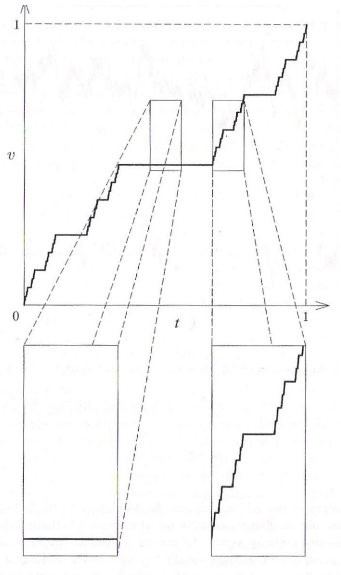

Figure 2.2: The Devil's staircase function [50].

In order to describe the fluctuations on scales l, and thus better characterise the intermittent behaviour, we introduce the concept of filtering. Considered a function $v(x)$, a cut-off wavenember K can be introduced such that $v(x)$ is split in two parts: the low-pass filter one $v_K^< = \sum_{k<K} v_k e^{ikx}$ and the high-pass filter one $v_K^> = \sum_{k>K} v_k e^{ikx}$, with $v = v_K^< + v_K^>$.
The high-pass filter contains all scales $l < K^{-1}$. Therefore, it is reasonable to suppose that, for a spectrum steeper than k^{-1}, the contribution of the high wavenumbers $k \gg K$ is negligible so that the high-pass filtered part represents the small range $l \lesssim K^{-1}$.

A useful measure of intermittency is given by the following quantity

called flatness (seldom kurtosis)

$$F_K = \frac{\langle \left(v_K^>\right)^4 \rangle}{\langle \left(v_K^>\right)^2 \rangle^2} \tag{2.4.36}$$

In fact under the assumption that fluctuations are present only during a particular fraction δ_K of space (or time), the averages in (2.4.36) are proportional to δ_K and $F_K \sim \delta_K^{-1}$. Thus flatness grows with increasing sparseness of the fluctuations of the signal.

We observe that, according to this definition of intermittency, neither Gaussian nor self-similar signals can be intermittent, because they have flatness independent of K. In particular in the Gaussian case we have that the Gaussian property is conserved by any linear operation including filtering, guaranteeing a flatness of constant value 3.

It is now worth asking if turbulence can be considered self-similar or intermittent. As shown by Kolmogorov theory (K41) [80, 79] a turbulent signal exhibits a self-similar behaviour. However if we perform a high-pass filtering on the signal with high enough wavenumber K, the emergence of intermittent features is observed (figure 2.3).

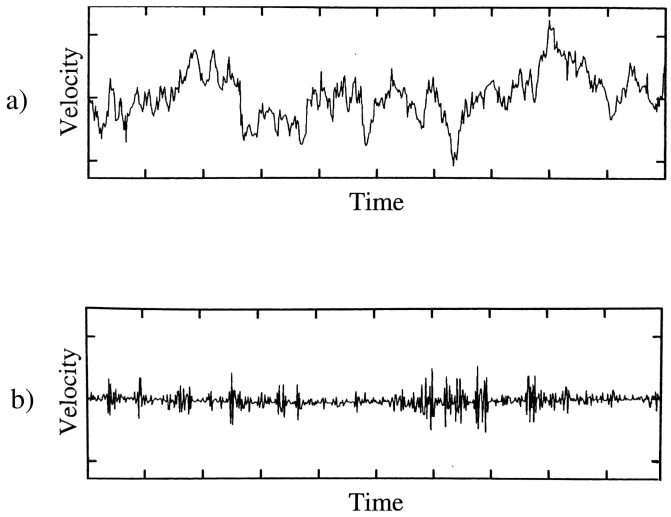

Figure 2.3: (a) Velocity signal from a jet with Reynolds number at Taylor scale of 700. (b) Velocity signal after the high-pass filtering: intermittent bursts are now visible [53].

The rate of intermittency becomes more important when the scale associated with K^{-1} is comparable or smaller than the Kolmogorov dissipative scale. Thus the appearance of intermittency is a property of the dissipation range and it does not represent a violation of the self-organisation representation presented in the K41 theory of the inertial range.

In order to describe in a clearer way the difference between self-similarity and intermittency, we have performed an MHD incompressible numerical

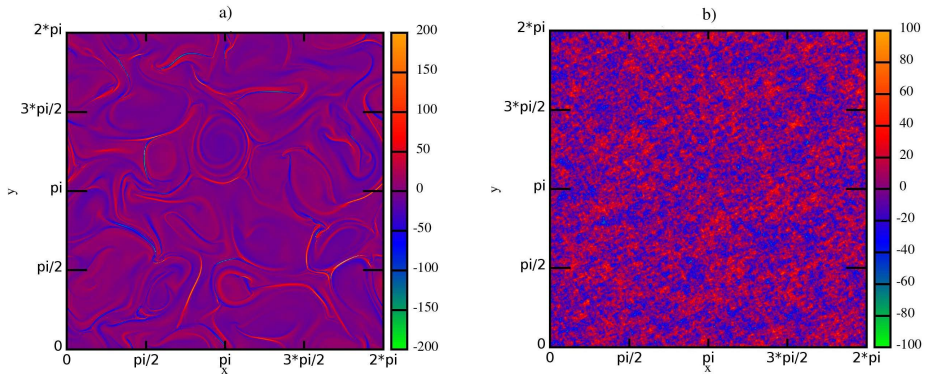

Figure 2.4: Contour plots of the current density: (a) 2D MHD turbulent state; (b) the corresponding random state with the same energy spectrum and dissipation length (MHD incompressible numerical simulation on a 2D spatial grid box of dimensions 2048^2 periodic on the boundary).

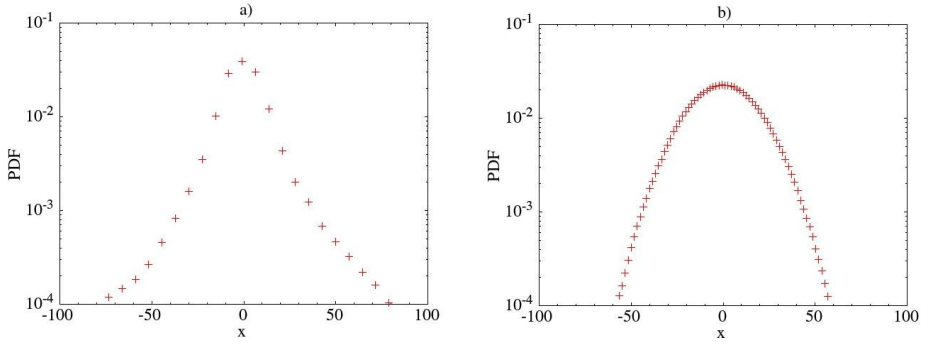

Figure 2.5: PDFs of the current density: (a) of the turbulent state in Figure 2.4(a); of the random state in Figure 2.4(b).

simulation on a 2D spatial grid box of dimensions 2048^2 periodic on the boundary. Let's consider the contour plots of the current density in the turbulence state (Figure 2.4(a)) and the corresponding random state with the same energy spectrum and dissipation length (Figure 2.4(b)). We observe that whereas in the turbulent state the dissipative eddies form separated and well defined current sheets structures, the dissipative small scales structures in the random state are space filling. In fact the behaviour of the random state is statistically uniform: its probability distribution function (PDF) exhibits a Gaussian distribution (Figure 2.5(b)). On the contrary the turbulent state, characterised by the occurrence of well organised structures, displays PDF with tails far from the Gaussian due to the formation of intermittent structures (Figure 2.5(a)). The sparseness of the distribution of small scales, the occurrence of well organised structures and the strongly non-Gaussian features of the PDFs of the dynamical variables are characteristic features of intermittency on dissipative scales in turbulence.

For a more detailed description of intermittency in both non-magnetised and magnetised turbulent flows we refer to [50, 7].

Chapter 3

Wavelet analysis

Wavelets are functions well localised in both physical and spectral space. The additional possibility of controlling both their smoothness (which determines the number of times they can be differentiated) and their number of vanishing moments (which determines the number of times they can be integrated) makes wavelet an efficient way of representing data which are neither completely particle-like nor wave-like (e.g. multi-scale localised structures). Thus wavelets are suitable for our purpose of detecting and analysing the coherent structures that characterise intermittent turbulent flows [49, 101, 44, 47, 46, 150, 151, 112].

Similar to Fourier transforms, wavelet transforms can be classified as either continuous or discrete. Here the continuous wavelet transform is introduced, followed by a description of discrete wavelet transform. An algorithm for the implementation of the orthogonal discrete wavelet transform in both two- and three-dimensional cases is also given.

3.1 Continuous wavelet transform

Given a a real square integrable function $f(x)$ (i.e. $\int_{-\infty}^{+\infty} f^2(x)dx < \infty$), its continuous wavelet transform $W(b,a)$ is defined as [64, 101]

$$W(b,a) = C_g^{-\frac{1}{2}} \frac{1}{\sqrt{a}} \int_{-\infty}^{+\infty} \psi\left(\frac{x-b}{a}\right) f(x)dx \tag{3.1.1}$$

where a is a scale dilatation, b is a position translation and $\psi(x)$ is the wavelet function, which satisfies the admissible condition

$$C_g = \int_{-\infty}^{+\infty} |K|^{-1} |\hat{\psi}(K)|^2 dK < \infty \tag{3.1.2}$$

with K the wavenumber and $\hat{\psi}$ the Fourier transform of $\psi(x)$, i.e. $\hat{\psi}(K) = \int_{-\infty}^{+\infty} \psi(x) e^{-ikx} dx$. The admissible condition (3.1.2) guarantees the locality of C_g in the Fourier space.

Thus the continuous wavelet transform $W(b,a)$ can be seen as the relative contribution of scales a to the function f at position b involving one

generating function $\psi(x)$ and providing translation and dilatation simultaneously, in order to reduce the spatial support at the same rate at which the scale is decreased (or the frequency is increased).

The admissible property for the wavelet function permits the inversion of the wavelet transform [65, 101], *i.e.*

$$f(x) = C_g^{-\frac{1}{2}} \int_0^{+\infty} \int_{-\infty}^{+\infty} a^{-\frac{1}{2}} \psi\left(\frac{x-b}{a}\right) W(b,a) \frac{db\ da}{a^2} \tag{3.1.3}$$

Also in the context of the wavelet transform, it is possible to generalise Parseval's theorem, where the equality between the total energy in physical space and wavelet space is considered as a particular case. In fact

$$\int_{-\infty}^{+\infty} f_1(x) f_2^*(x) dx = C_g^{-1} \int_0^{+\infty} \int_{-\infty}^{+\infty} W_1(b,a) W_2^*(b,a) \frac{dx\ da}{a^2} \tag{3.1.4}$$

where $*$ stands for the complex conjugate [65].

The previous definition of wavelet transform can be extended to vector functions $\mathbf{f}(x) = (f_i(x))_{i=1,\dots n}$. In this case the transform is a vector $\mathbf{W}(b,a)$ with the wavelet transform of its components given by $f_i(x)$.
In case of higher dimensions several possibilities in the extension of definition (3.1.1) can be considered. In addition to the dilations and translations, the (group of) rotations of non-isotropic wavelets can be considered [22, 32]. Here we will always consider only spherical symmetric wavelets (isotropic case).

3.2 Wavelet series

Similar to the continuous wavelet transform, a set of self-similar functions, whose dilations and translations provide simultaneous resolution in scale and position, can be considered. The bases used for the decomposition can be made orthogonal and complete, by choosing a logarithmically uniform spacing of scales with increasingly coarser spatial discretisation at larger scales. The conditions lead to the definition of the following basic functions [30, 92]

$$\psi_{[i]}^{(m)}(x) = a^{-\frac{1}{2}m} \psi\left(\frac{x - i\ b\ a^m}{a^m}\right) \tag{3.2.5}$$

where a is the base of the dilatation, b in the translation length in units of a^m, m and i are the variable scale and variable position index respectively. We note that net translation depends on the dilatation rate and, in general, this makes the choice of the parameters a and b non arbitrary [30]. Let us choose $a = 2$ and $b = 1$, such that all the scales $r_m = 2^m$ and all the translations $2^m i$ in multiple of the scale r_m are considered. This implies that all the wavelets considered obey, for every m, the relation $\Delta x_m \Delta\left(\frac{1}{r_m}\right) = 2^m\left(2^{-(m-1)} - 2^{-m}\right) = 1$.

Using the previous formulation, a one-dimensional function can be decomposed into a discrete set of function with scales and location modulation such as

$$f(x) = \sum_{m=-\infty}^{+\infty} \sum_{i=-\infty}^{+\infty} w^{(m)}[i]\psi^{(m)}(x - 2^m i) \tag{3.2.6}$$

where $w^{(m)}[i]$ are the discrete wavelet coefficients associated to $f(x)$, that depend on the position index i and the scale index m, and

$$\psi^{(m)}(x) = 2^{-\frac{1}{2}m}\psi\left(\frac{x}{2^m}\right). \tag{3.2.7}$$

Function $\psi(x)$ obeys the following constraint

$$\int_{-\infty}^{+\infty} \psi^{(m)}(x - 2^m i)\psi^{(n)}(x - 2^n j)dx = \delta_{ij}\delta_{mn} \tag{3.2.8}$$

where δ_{**} is the Kronecker delta. Thus function (3.2.7) is orthonormal to its own translations and its own dilatations.
Property (3.2.8) permits the computation of the discrete wavelet coefficients for the function $f(x)$ such as

$$w^{(m)}[i] = \int_{-\infty}^{+\infty} \psi^{(m)}(x - 2^m i)f(x)dx \tag{3.2.9}$$

Hence coefficient (3.2.9) can be seen as a measure of the contribution to the signal of scales 2^m in the neighbourhood of the point $2^m i$.

Another important consequence of the orthonormal property (3.2.8) is that the total energy of the function verifies relation

$$\int_{-\infty}^{+\infty} f^2(x)dx = \sum_{m=-\infty}^{+\infty} \sum_{i=-\infty}^{+\infty} \left(w^{(m)}[i]\right)^2. \tag{3.2.10}$$

In order to extend the theory of the one-dimensional wavelet series to higher dimensions, it is necessary to consider in a space n-dimensional separable basis functions of the form

$$\mathbf{\Psi}(\mathbf{x}) = \prod_{l=1,\ldots,n} \psi_l(x_l). \tag{3.2.11}$$

Like the one-dimensional formulation, scales of the form 2^m are used but now all the locations in the n-dimensional space have to be considered. In fact, it turns out that for a complete representation additional internal degrees of freedom must be considered, using for this purpose 2^{n-1} distinct basis functions. They complement the function formed by the product of the wavelets along the n Cartesian directions as in (3.2.11) [101].

3.2.1 Higher-dimensional cases

In this paragraph we analyse the representation of the wavelet transform in both the two- and three-dimensional cases. These representations are obtained by introducing a separable basis function of the form (3.2.11), with $n = 2$ in the 2D case and $n = 3$ in the 3D one.

Two-dimensional case

A two-dimensional decomposition with a complete and separable set of base functions can be achieved using three distinct basis function (indexed by q) [101]. In fact, let $\mathbf{x} = (x_1, x_2) \in \mathbb{R}^2$, and set $[\mathbf{i}] = [i_1, i_2]$ as the position index and m as the scale index, then we define the base functions

$$\Psi^{(m,q)}[\mathbf{x} - 2^m\mathbf{i}] = \begin{cases} \psi^{(m)}(x_1 - 2^m i_1)\ \psi^{(m)}(x_2 - 2^m i_2), & q = 1 \\ \psi^{(m)}(x_1 - 2^m i_1)\ \phi^{(m)}(x_2 - 2^m i_2), & q = 2 \\ \phi^{(m)}(x_1 - 2^m i_1)\ \psi^{(m)}(x_2 - 2^m i_2), & q = 3 \end{cases} \tag{3.2.12}$$

The function $\phi^{(m)}(\cdot)$ is the so called "smoothing function", which is defined as the translation and the dilatation of a single sampling function with fast decay away from the origin, $\phi(x)$, *i.e.*

$$\phi^{(m)}(x) = 2^{-\frac{m}{2}}\phi\left(\frac{x}{2^m}\right) \tag{3.2.13}$$

The smoothing function obeys the following specific conditions:

- orthonormality for each scale m, *i.e.*

$$\int_{-\infty}^{+\infty} \phi^{(m)}(x - 2^m i)\phi^{(m)}(x - 2^m j)\, dx = \delta_{ij} \tag{3.2.14}$$

- fixed the scale m, all the wavelet basis functions are perpendicular to the smoothing functions, *i.e.*

$$\int_{-\infty}^{+\infty} \phi^{(m)}(x - 2^m i)\psi^{(m)}(x - 2^m j)\, dx = 0 \tag{3.2.15}$$

Choosing the basis function as in (3.2.12) can be intuitively justified observing that we are picking up variations of scale 2^m that occur along all the possible combinations of the two Cartesian directions. For example for $q = 1$ we are considering all the variations that occur simultaneously in all the two directions (x_1, x_2), instead for $q = 2$ the only fluctuations considered are that ones along the x_2-direction.

With the appropriate choice of both the wavelet basis function and the smoothing function the following representation for a two-dimensional function $f(\mathbf{x})$ is obtained [1]

$$f(\mathbf{x}) = \sum_m \sum_{q=1}^{3} \sum_{(i_1,i_2)} w^{(m,q)}[i_1, i_2]\Psi^{(m,q)}[\mathbf{x} - 2^m\mathbf{i}] \tag{3.2.16}$$

Where the wavelet coefficients are computed using the following relation

$$w^{(m,q)}[i_1, i_2] = \int_{-\infty}^{+\infty} \int_{-\infty}^{+\infty} f(\mathbf{x}) \Psi^{(m,q)}[\mathbf{x} - 2^m \mathbf{i}] \, dx_1 \, dx_2 \tag{3.2.17}$$

Three-dimensional case

In the three-dimensional case the wavelet decomposition with a complete and separable set of base functions is reached using seven distinct basis function (indexed by q).
Let $[\mathbf{i}] = [i_1, i_2, i_3]$ be the position index, m the scale index and $\mathbf{x} = (x_1, x_2, x_3) \in \mathbb{R}^3$, we define the base functions as

$$\Psi^{(m,q)}[\mathbf{x} - 2^m \mathbf{i}] = \begin{cases} \psi^{(m)}(x_1 - 2^m i_1) \; \psi^{(m)}(x_2 - 2^m i_2) \; \psi^{(m)}(x_3 - 2^m i_3), & q = 1 \\ \psi^{(m)}(x_1 - 2^m i_1) \; \psi^{(m)}(x_2 - 2^m i_2) \; \phi^{(m)}(x_3 - 2^m i_3), & q = 2 \\ \psi^{(m)}(x_1 - 2^m i_1) \; \phi^{(m)}(x_2 - 2^m i_2) \; \psi^{(m)}(x_3 - 2^m i_3), & q = 3 \\ \psi^{(m)}(x_1 - 2^m i_1) \; \phi^{(m)}(x_2 - 2^m i_2) \; \phi^{(m)}(x_3 - 2^m i_3), & q = 4 \\ \phi^{(m)}(x_1 - 2^m i_1) \; \psi^{(m)}(x_2 - 2^m i_2) \; \psi^{(m)}(x_3 - 2^m i_3), & q = 5 \\ \phi^{(m)}(x_1 - 2^m i_1) \; \psi^{(m)}(x_2 - 2^m i_2) \; \phi^{(m)}(x_3 - 2^m i_3), & q = 6 \\ \phi^{(m)}(x_1 - 2^m i_1) \; \phi^{(m)}(x_2 - 2^m i_2) \; \psi^{(m)}(x_3 - 2^m i_3), & q = 7 \end{cases} \tag{3.2.18}$$

with $\phi^{(m)}(\cdot)$ the smoothing function defined in (3.2.13).

A proper choice of both the wavelet basis function and the smoothing function permits the following representation for a three-dimensional function $f(\mathbf{x})$ [30, 22]

$$f(\mathbf{x}) = \sum_m \sum_{q=1}^{7} \sum_{(i_1,i_2,i_3)} w^{(m,q)}[i_1, i_2, i_3] \Psi^{(m,q)}[\mathbf{x} - 2^m \mathbf{i}] \tag{3.2.19}$$

Where the wavelet coefficients are computed using the following relation

$$w^{(m,q)}[i_1, i_2, i_3] = \int_{-\infty}^{+\infty} \int_{-\infty}^{+\infty} \int_{-\infty}^{+\infty} f(\mathbf{x}) \Psi^{(m,q)}[\mathbf{x} - 2^m \mathbf{i}] \, dx_1 \, dx_2 \, dx_3 \tag{3.2.20}$$

3.3 Discrete wavelet transform

Consider a known function $f(x)$ on a discrete mesh grid x_i. In order to extend the previous dissertation to the discrete formulation, it is necessary to discretise both scale and spatial domains present in (3.1.1). One possible approach is to consider N grid points and thus discretise the two previous domain by N nodes (using a series of delta functions). Performing the wavelet transform of $f(x_i)$ we obtain N^2 wavelet coefficients, *i.e.* we have redundant information in the wavelet representation due to the over-complete description of $f(x_i)$. In this work we are interested in carrying out a statistical analysis of turbulent systems. Therefore, the redundant information present in the wavelet domain can produce spurious correlations (due to the transform applied to the data) which do not come from

the phenomenon described.
A way for avoiding this problem is to impose that the discretisation of both space and scale domains form a complete basis, in this manner the wavelet representation will be operated using only N wavelet coefficients. For this purpose it is possible to use discrete orthonormal wavelet transforms, which guarantee orthogonal basis functions and mutual independence of the wavelet coefficients. [103, 148].
It has been shown that a complete orthogonal basis can be constructed using for the scale discretisation a logarithmic uniform spacing, which has increasingly coarse spatial resolution at larger scales [30, 91, 103, 49].
In this work the wavelet basis chosen is the Haar basis

$$\psi^{(m)}(x - 2^m i) = 2^{-\frac{m}{2}} \psi\left(\frac{x - 2^m i}{2^m}\right) \tag{3.3.21}$$

where i is the position index, m the scale index and the mother Haar wavelet is defined as following

$$\psi(x) = \begin{cases} 1 & \text{for } 0 < x \leq \frac{1}{2} \\ -1 & \text{for } \frac{1}{2} < x < 1 \\ 0 & \text{otherwise} \end{cases} \tag{3.3.22}$$

Haar basis has been chosen due to both its differencing characteristics and its property of good localisation in the physical domain[90, 84].

3.3.1 One-dimensional case

Let $f(x)$ be a function sampled on a discrete mesh grid, $f(x_i) = f[i]$ with $x_i = ih,\ i = 1, ..., N = 2^M$ and h the mesh spacing. Its discrete wavelet transform at the discrete mesh points is given by

$$f[i] = \sum_{m=1}^{M} \sum_{j=1}^{2^{M-m}} w^{(m)}[j] \psi^{(m)}(i - 2^m j) \tag{3.3.23}$$

where $\psi^m(\cdot)$ is the wavelet base defined in (3.3.21) and $w^m(j)$ is the wavelet coefficient indexed by m for the scale and by j for the position, such that

$$w^{(m)}[j] = \sum_{i=1}^{M} f[i] \psi^{(m)}(i - 2^m j) \tag{3.3.24}$$

Wavelet transform (3.3.23) verifies a generalisation of the Parseval theorem, *i.e.* the total energy of the function obeys

$$\sum_{i=1}^{N} f[i]^2 = \sum_{m=1}^{M} \sum_{j=1}^{2^{M-m}} (w^{(m)}[j])^2 \tag{3.3.25}$$

From equation (3.3.25), the total energy density contained at each scale $r_m = 2^m h$ is given by

$$N^{-1} \sum_{j=1}^{2^{M-m}} (w^{(m)}[j])^2) \tag{3.3.26}$$

We can define the wavenumber corresponding to the scale r_m as

$$k_m = \frac{2\pi}{r_m} = 2\pi 2^{-m} h^{-1} \tag{3.3.27}$$

Thus the power-spectral density (per unit of wavenumber) is given by expression (3.3.26) divided by $\Delta k_m = 2\pi 2^{-m} h^{-1} \ln 2$, *i.e.*

$$\begin{aligned} E(k_m) &= N^{-1} \sum_{j=1}^{2^{M-m}} (w^{(m)}[j])^2 \frac{2^m h}{2\pi \ln 2} \overset{N=2^M}{=} \\ &= 2^{-M} \Big[\frac{1}{2^{M-m}} \sum_{j=1}^{2^{M-m}} w^{(m)}[j])^2) \Big] 2^{M-m} \frac{2^m h}{2\pi \ln 2} = \\ &= \langle (w^{(m)}[j])^2 \rangle \frac{h}{2\pi \ln 2} \end{aligned} \tag{3.3.28}$$

where $\langle \cdot \rangle$ is the spatial average on all the spatial indexes j at scale corresponding to k_m.

3.3.2 Two-dimensional case

The formulation of two-dimensional continuous wavelet transform presented in paragraph 3.2.1 can be extended to the discrete form. Let $f(\mathbf{x})$ be a function sampled on a discrete mesh, such that $f(\mathbf{x}) = f(x_1, x_2) = f[i_1, i_2]$, with $\mathbf{x} = (x_1, x_2) = (h_1 i_1, h_2, i_2)$, $1 \leq i_* \leq 2^M$ and h_1, h_2 the mesh spacing. Considering the wavelet basis function (3.2.12) with $\psi^{(m)}(\cdot)$ the Haar wavelet (3.3.21) and the smoothing function (3.2.13), such that

$$\phi(x) = \begin{cases} 1 & \text{for } 0 < x < 1 \\ 0 & \text{otherwise} \end{cases} \tag{3.3.29}$$

the two-dimensional function $f(\mathbf{x})$ can be represented, in each point of the mesh, in the following way

$$f(i_1, i_2) = \sum_{m=1}^{M} \sum_{q=1}^{3} \sum_{k_1,k_2=1}^{2^{M-m}} w^{(m,q)}[k_1, k_2] \Psi^{(m,q)}[i_1 - 2^m k_1, i_2 - 2^m k_2] \tag{3.3.30}$$

Where the position is indexed with (k_1, k_2), the basis function with q, the scale with m and the wavelet coefficients are defined such that

$$w^{(m,q)}[k_1, k_2] = \sum_{i_1,i_2=1}^{2^M} f(i_1, i_2) \Psi^{(m,q)}[i_1 - 2^m k_1, i_2 - 2^m k_2] \tag{3.3.31}$$

We observe that for every position (k_1, k_2) the total number of wavelet coefficients (without considering the total mean made on the grid) is

$$\sum_{q=1}^{3}\sum_{m=1}^{M} 2^{2(M-m)} = \sum_{q=1}^{3} 2^{2M} \sum_{m=1}^{M} \frac{1}{2^{2m}} = \sum_{q=1}^{3} 2^{2M} \sum_{m=1}^{M} \left(\frac{1}{4}\right)^m = \\ = \sum_{q=1}^{3} 2^{2M} \left(\frac{1}{3} - \frac{4^{-M}}{3}\right) = \sum_{q=1}^{3} \frac{2^{2M}-1}{3} = 2^{2M} - 1 \tag{3.3.32}$$

Thus the wavelet transform preserves the total information of the discrete two-dimensional function.

Equation (3.3.28) becomes

$$E(k_m) = N^{-2} \sum_{i_1,i_2=1}^{2^{M-m}} \sum_{q=1}^{3} (w^{(m,q)}[j_1, j_2])^2 \frac{2^m (h_1 h_2)^{1/2}}{2\pi \ln 2} \overset{N=2^M}{=} \\ = 2^{-2M} \Big[\frac{1}{2^{2M-2m}} \sum_{i_1,i_2=1}^{2^{M-m}} \sum_{q=1}^{3} (w^{(m,q)}[j_1, j_2])^2\Big] 2^{2M-2m} \frac{2^m (h_1 h_2)^{1/2}}{2\pi \ln 2} = \\ =< (w^{(m,q)}[j_1, j_2])^2 > \frac{2^{-m} (h_1 h_2)^{1/2}}{2\pi \ln 2} \tag{3.3.33}$$

Calculus of the two-dimensional wavelet coefficients: the algorithm

Let's consider the two-dimensional known function $f(\mathbf{x})$ on a mesh grid $(h_1 i_1, h_2 i_2)$ with $1 \le i_1, i_2 \le 2^M$.
We define for the scale index $m = 0$

$$S^{(0)}(i_1, i_2) = f(i_1, i_2) - \bar{f}, \quad \text{with } \bar{f} = 2^{-2M} \sum_{i_1,i_2=1}^{2^M} f(i_1, i_2) \tag{3.3.34}$$

and for $m = 1, ..., M$ the recursive sum

$$S^{(m)}(i_1, i_2) = \frac{1}{2}\Big[S^{(m-1)}(2i_1 - 1, 2i_2 - 1) + S^{(m-1)}(2i_1 - 1, 2i_2) \\ + S^{(m-1)}(2i_1, 2i_2 - 1) + S^{(m-1)}(2i_1, 2i_2)\Big] \tag{3.3.35}$$

Using relations (3.3.34) (3.3.35) (3.2.12), it is possible to compute the wavelet coefficient (3.3.31) for each scale index m, basis function index $1 \le q \le 3$ and position index $1 \le k_1, k_2 \le 2^{M-m}$ as followed

$$w^{(m,q)}[k_1, k_2] = \sigma_q \begin{bmatrix} S^{(m-1)}(2k_1 - 1, 2k_2 - 1) \\ S^{(m-1)}(2k_1 - 1, 2k_2) \\ S^{(m-1)}(2k_1, 2k_2 - 1) \\ S^{(m-1)}(2k_1, 2k_2) \end{bmatrix} \tag{3.3.36}$$

where, varying q, σ_q is the row vector

$$\sigma_q = \begin{cases} [1 & -1 & -1 & 1], & \text{for } q = 1 \\ [1 & 1 & -1 & -1], & \text{for } q = 2 \\ [1 & -1 & 1 & -1], & \text{for } q = 3 \end{cases} \tag{3.3.37}$$

Introducing the row vector $\sigma_4 = [1\ 1\ 1\ 1]$, we define a linear system that permits to compute all the wavelet coefficients at a fixed scale index m (3.3.36), and to obtain the representation in the wavelet space of the two-dimensional function under study (3.3.35). For each scale index m the associated linear system is

$$\begin{bmatrix} w^{(m,1)}[k_1,k_2] \\ w^{(m,2)}[k_1,k_2] \\ w^{(m,3)}[k_1,k_2] \\ S^{(m)}(k_1,k_2) \end{bmatrix} = \frac{1}{2} \begin{bmatrix} 1 & -1 & -1 & 1 \\ 1 & 1 & -1 & -1 \\ 1 & -1 & 1 & -1 \\ 1 & 1 & 1 & 1 \end{bmatrix} \begin{bmatrix} S^{(m-1)}(2k_1-1,2k_2-1) \\ S^{(m-1)}(2k_1-1,2k_2) \\ S^{(m-1)}(2k_1,2k_2-1) \\ S^{(m-1)}(2k_1,2k_2) \end{bmatrix} \tag{3.3.38}$$

The matrix in system (3.3.38) is invertible, so that if the wavelet coefficients $w^{(m,q)}[\cdot]$ and the sum $S^{(m)}(\cdot)$ are known at scale m and for all the index q, it is possible to calculate $S^{(m-1)}(i_1,i_2)$ for all the mesh grid and the scale index m (from M to 1). Therefore, the wavelet inverse transform of the two-dimensional function $f(\mathbf{x})$ can be obtained solving the following liner system

$$\begin{bmatrix} S^{(m-1)}(2k_1-1,2k_2-1) \\ S^{(m-1)}(2k_1-1,2k_2) \\ S^{(m-1)}(2k_1,2k_2-1) \\ S^{(m-1)}(2k_1,2k_2) \end{bmatrix} = \frac{1}{2} \begin{bmatrix} 1 & 1 & 1 & 1 \\ -1 & 1 & -1 & 1 \\ -1 & -1 & 1 & 1 \\ 1 & -1 & -1 & 1 \end{bmatrix} \begin{bmatrix} w^{(m,1)}[k_1,k_2] \\ w^{(m,2)}[k_1,k_2] \\ w^{(m,3)}[k_1,k_2] \\ S^{(m)}(k_1,k_2) \end{bmatrix} \tag{3.3.39}$$

3.3.3 Three-dimensional case

Here the formulation of three-dimensional continuous wavelet transform presented in paragraph 3.2.1 is extended to the discrete form.

Let $f(\mathbf{x})$ be a function sampled on a discrete mesh, such that $f(\mathbf{x}) = f(x_1,x_2) = f[i_1,i_2]$, with $\mathbf{x} = (x_1,x_2,x_3) = (h_1 i_1, h_2 i_2, h_3 i_3)$, $1 \le i_* \le 2^M$ and $h_1,\ h_2,\ h_3$ the mesh spacing.
Considering the wavelet basis function (3.2.18) with $\psi^{(m)}(\cdot)$ the Haar wavelet (3.3.21) and the smoothing function (3.2.13), the three- dimensional function $f(\mathbf{x})$ can be represented, in each point of the mesh, as follows

$$f(i_1,i_2,i_3) = \sum_{m=1}^{M} \sum_{q=1}^{7} \sum_{k_1,k_2,k_3=1}^{2^{M-m}} w^{(m,q)}[k_1,k_2,k_3] \Psi^{(m,q)}[i_1 - 2^m k_1, i_2 - 2^m k_2, i_3 - 2^m k_3] \tag{3.3.40}$$

with $[k_1, k_2, k_3]$ the position indexes, m the scale index and $w^{(m,q)}[\cdot]$ the wavelet coefficients such that

$$w^{(m,q)}[k_1,k_2,k_3] = \sum_{i_1,i_2,i_3=1}^{2^M} f(i_1,i_2)\Psi^{(m,q)}[i_1-2^m k_1, i_2-2^m k_2, i_3-2^m k_3] \tag{3.3.41}$$

In this case, the application of the wavelet transform guaranties the conservation of the original signal information, in fact

$$\begin{aligned}\sum_{q=1}^{7}\sum_{m=1}^{M} 2^{3(M-m)} &= \sum_{q=1}^{7} 2^{3M}\sum_{m=1}^{M}\frac{1}{2^{3m}} = \sum_{q=1}^{7} 2^{3M}\sum_{m=1}^{M}\left(\frac{1}{8}\right)^m = \\ &= \sum_{q=1}^{7} 2^{3M}\frac{\frac{1}{8}-\left(\frac{1}{8}\right)^{M+1}}{1-\frac{1}{8}} = \sum_{q=1}^{7}\frac{2^{3M}-1}{7} = 2^{3M}-1\end{aligned} \tag{3.3.42}$$

Now, equation (3.3.28) becomes

$$\begin{aligned}E(k_m) &= N^{-3}\sum_{j_1,j_2,j_3=1}^{2^{M-m}}\sum_{q=1}^{7}(w^{(m,q)}[j_1,j_2,j_3])^2\frac{2^m(h_1h_2h_3)^{1/3}}{2\pi\ln 2} \\ &\overset{N=2^M}{=} 2^{-3M}\left[\frac{1}{2^{3M-3m}}\sum_{j_1,j_2,j_3=1}^{2^{M-m}}\sum_{q=1}^{7}(w^{(m,q)}[j_1,j_2,j_3])^2\right]2^{3M-3m}\frac{2^m(h_1h_2h_3)^{1/3}}{2\pi\ln 2} \\ &=< (w^{(m,q)}[j_1,j_2,j_3])^2 > \frac{2^{-m}(h_1h_2h_3)^{1/3}}{2\pi\ln 2}\end{aligned} \tag{3.3.43}$$

Calculus of the three-dimensional wavelet coefficients: the algorithm

Using the previous notation, we define for the scale index $m = 0$

$$S^{(0)}(i_1,i_2,i_3) = f(i_1,i_2,i_3) - \bar{f}, \quad \text{with } \bar{f} = 2^{-3M}\sum_{i_1,i_2,i_3=1}^{2^M} f(i_1,i_2,i_3) \tag{3.3.44}$$

and for $m = 1, ..., M$ the recursive sum

$$\begin{aligned}S^{(m)}(i_1,i_2,i_3) = \frac{1}{2}\Big[&S^{(m-1)}(2i_1-1,2i_2-1,2i_3-1) + S^{(m-1)}(2i_1-1,2i_2-1,2i_3) \\ &+ S^{(m-1)}(2i_1-1,2i_2,2i_3-1) + S^{(m-1)}(2i_1-1,2i_2,2i_3) \\ &+ S^{(m-1)}(2i_1,2i_2-1,2i_3-1) + S^{(m-1)}(2i_1,2i_2-1,2i_3) \\ &+ S^{(m-1)}(2i_1,2i_2,2i_3-1) + S^{(m-1)}(2i_1,2i_2,2i_3)\Big]\end{aligned} \tag{3.3.45}$$

Thanks to relations (3.3.44) (3.3.45) (3.2.18), it is possible to compute the wavelet coefficient (3.3.41) for each scale index m, basis function index

$1 \leq q \leq 7$ and position index $1 \leq k_1, k_2, k3 \leq 2^{M-m}$ as followed

$$w^{(m,q)}[k_1,k_2,k_3] = \sigma_q \begin{bmatrix} S^{(m-1)}(2k_1-1,2k_2-1,2k_3-1) \\ S^{(m-1)}(2k_1-1,2k_2-1,2k_3) \\ S^{(m-1)}(2k_1-1,2k_2,2k_3-1) \\ S^{(m-1)}(2k_1-1,2k_2,2k_3) \\ S^{(m-1)}(2k_1,2k_2-1,2k_3-1) \\ S^{(m-1)}(2k_1,2k_2-1,2k_3) \\ S^{(m-1)}(2k_1,2k_2,2k_3-1) \\ S^{(m-1)}(2k_1,2k_2,2k_3) \end{bmatrix} \tag{3.3.46}$$

where for each q, σ_q is the row vector

$$\sigma_q = \begin{cases} [1 & -1 & -1 & 1 & -1 & 1 & 1 & -1], & \text{for } q=1 \\ [1 & 1 & -1 & -1 & -1 & -1 & 1 & 1], & \text{for } q=2 \\ [1 & -1 & 1 & -1 & -1 & 1 & -1 & 1], & \text{for } q=3 \\ [1 & 1 & 1 & 1 & -1 & -1 & -1 & -1], & \text{for } q=4 \\ [1 & -1 & -1 & 1 & 1 & -1 & -1 & 1], & \text{for } q=5 \\ [1 & 1 & -1 & -1 & 1 & 1 & -1 & -1], & \text{for } q=6 \\ [1 & -1 & 1 & -1 & 1 & -1 & 1 & -1], & \text{for } q=7 \end{cases} \tag{3.3.47}$$

Introducing the row vector $\sigma_8 = [1\ 1\ 1\ 1\ 1\ 1\ 1\ 1]$, all the wavelet coefficients at a fixed scale index m (3.3.46) and the three-dimensional wavelet representation (3.3.45) of the function $f(\mathbf{x})$ can be computed solving the following linear system

$$\begin{bmatrix} w^{(m,1)}[k_1,k_2,k_3] \\ w^{(m,2)}[k_1,k_2,k_3] \\ w^{(m,3)}[k_1,k_2,k_3] \\ w^{(m,4)}[k_1,k_2,k_3] \\ w^{(m,5)}[k_1,k_2,k_3] \\ w^{(m,6)}[k_1,k_2,k_3] \\ w^{(m,7)}[k_1,k_2,k_3] \\ S^{(m)}[k_1,k_2,k_3]) \end{bmatrix} = \left(\frac{1}{2}\right)^{3/2} \begin{bmatrix} 1 & -1 & -1 & 1 & -1 & 1 & 1 & -1 \\ 1 & 1 & -1 & -1 & -1 & -1 & 1 & 1 \\ 1 & -1 & 1 & -1 & -1 & 1 & -1 & 1 \\ 1 & 1 & 1 & 1 & -1 & -1 & -1 & -1 \\ 1 & -1 & -1 & 1 & 1 & -1 & -1 & 1 \\ 1 & 1 & -1 & -1 & 1 & 1 & -1 & -1 \\ 1 & -1 & 1 & -1 & 1 & -1 & 1 & -1 \\ 1 & 1 & 1 & 1 & 1 & 1 & 1 & 1 \end{bmatrix} \begin{bmatrix} S^{(m-1)}(2k_1-1,2k_2-1,2k_3-1) \\ S^{(m-1)}(2k_1-1,2k_2-1,2k_3) \\ S^{(m-1)}(2k_1-1,2k_2,2k_3-1) \\ S^{(m-1)}(2k_1-1,2k_2,2k_3) \\ S^{(m-1)}(2k_1,2k_2-1,2k_3-1) \\ S^{(m-1)}(2k_1,2k_2-1,2k_3) \\ S^{(m-1)}(2k_1,2k_2,2k_3-1) \\ S^{(m-1)}(2k_1,2k_2,2k_3) \end{bmatrix} \tag{3.3.48}$$

If the wavelet coefficients $w^{(m,q)}[\cdot]$ and the sum $S^{(m)}(\cdot)$ are known at the scale m and for all the index q, it is possible to calculate $S^{(m-1)}(i_1,i_2)$ for all the mesh grid and the scale index m from M to 1 inverting the previous system, *i.e.*

$$\begin{bmatrix} S^{(m-1)}(2k_1-1,2k_2-1,2k_3-1) \\ S^{(m-1)}(2k_1-1,2k_2-1,2k_3) \\ S^{(m-1)}(2k_1-1,2k_2,2k_3-1) \\ S^{(m-1)}(2k_1-1,2k_2,2k_3) \\ S^{(m-1)}(2k_1,2k_2-1,2k_3-1) \\ S^{(m-1)}(2k_1,2k_2-1,2k_3) \\ S^{(m-1)}(2k_1,2k_2,2k_3-1) \\ S^{(m-1)}(2k_1,2k_2,2k_3) \end{bmatrix} = 2^{3/2} \begin{bmatrix} 1 & 1 & 1 & 1 & 1 & 1 & 1 & 1 \\ -1 & 1 & -1 & 1 & -1 & 1 & -1 & 1 \\ -1 & -1 & 1 & 1 & -1 & -1 & 1 & 1 \\ 1 & -1 & -1 & 1 & 1 & -1 & -1 & 1 \\ -1 & -1 & -1 & -1 & 1 & 1 & 1 & 1 \\ 1 & -1 & 1 & -1 & -1 & 1 & -1 & 1 \\ 1 & 1 & -1 & -1 & -1 & -1 & 1 & 1 \\ -1 & 1 & 1 & -1 & 1 & -1 & -1 & 1 \end{bmatrix} \begin{bmatrix} w^{(m,1)}[k_1,k_2,k_3] \\ w^{(m,2)}[k_1,k_2,k_3] \\ w^{(m,3)}[k_1,k_2,k_3] \\ w^{(m,4)}[k_1,k_2,k_3] \\ w^{(m,5)}[k_1,k_2,k_3] \\ w^{(m,6)}[k_1,k_2,k_3] \\ w^{(m,7)}[k_1,k_2,k_3] \\ S^{(m)}[k_1,k_2,k_3]) \end{bmatrix} \tag{3.3.49}$$

Chapter 4

Coherent structure formation through nonlinear interactions in 2D magnetohydrodynamic turbulence

As shown in Chapter 1 the dynamical evolution of 2D incompressible MHD is described by the following set of equations

$$\begin{aligned} \partial_t \omega + \mathbf{v} \cdot \nabla \omega &= \mathbf{B} \cdot \nabla j + \nu \nabla^2 \omega \\ \partial_t a + \mathbf{v} \cdot \nabla a &= \eta \nabla^2 a \end{aligned} \tag{4.0.1}$$

where $\mathbf{v}$ and $\mathbf{B}$ are the fluid velocity and the magnetic field which both have zero z components. The z component of the vector potential, the electric current density and the fluid vorticity are given by a, j and ω respectively. The stream function is given by ϕ such that $\omega = -\nabla^2 \phi$, ν is the kinematic viscosity[1] and η is the magnetic diffusivity [33, 6]. Equations (4.0.1) are written in familiar Alfvén units [98] where lengths scale with l_0, typical large scale. Velocity and magnetic field scale with the root-mean-square of the Alfvén speed C_A and time scales with l_0/C_A .

In their ideal form. i.e. when $\nu = \eta = 0$, these equations conserve three global quadratic invariants (rugged invariants i.e. invariants which survive to any Galerkin truncation): the energy $E = \frac{1}{2}\int (v^2 + B^2) d^2r$, the cross-helicity $H_c = \frac{1}{2}\int \mathbf{v} \cdot \mathbf{B}\ d^2r$ and the mean square potential vector $A^2 = \int a^2\ d^2r$.

In order to study the behaviour of turbulent flows associated with these equations, numerical simulations at very low values of ν and η and periodic boundary conditions are usually performed. In such cases, the long time

[1] An isotropic kinematic viscosity is a typical assumption in the MHD mathematical model, even if in real plasmas ν can be strongly non-isotropic.

evolution of these equations has been shown to give rise to the so-called *self-organization* of turbulent flows. In this scenario large scale very correlated structures are finally obtained, whose properties can be derived from the idea that energy is minimised while holding constant cross-helicity and mean square magnetic potential [141].

Let λ and ϕ be Lagrangian multipliers and Ω an open regular and limited domain of $\mathbb{R}^2$, imposing that

$$\delta\left[\frac{1}{2}\int_{\Omega}(v^2+B^2)d^2r-\frac{\lambda}{2}\int_{\Omega}\mathbf{v}\cdot\mathbf{B}\;d^2r-\phi\int_{\Omega}a^2d^2r\right]=0 \tag{4.0.2}$$

and using the variational calculation analysis, we obtain relations

$$\begin{aligned}\mathbf{v}-\lambda\mathbf{B}&=0\\ j-\lambda\omega-2\phi\;a&=0\end{aligned} \tag{4.0.3}$$

which can be recast to the following form

$$\frac{\omega}{j}=\lambda,\qquad \frac{j}{a}=\frac{1-\lambda^2}{2\phi}=\varphi \tag{4.0.4}$$

where the presence of a correlation between ω, j and $j,\ a$ is emphasised.

In the present chapter we explore the possibility that the above equilibria, which are intended to be long time solutions of equations (4.0.1), have an influence on the cascade processes, manifesting on time-scales comparable to an eddy turnover time.
We present in detail the analysis built up in order to identify and characterise the rapid time formation of coherent structures induced by nonlinear interaction in MHD incompressible turbulent flows. These structures are characterised by the occurrence at small scales of regions where the correlations predicted by the hypothesis of quadratic rugged invariant conservations are locally present, a property which is the equivalent to the well known "Beltramisation" of the fluid flows.

Different high resolution 2D MHD simulations have been tested in order to asses the general validity of the obtained results. The implemented algorithm is based on the discrete orthogonal wavelet transform (Chapter 3).

4.1 Simulations

System of equations (4.0.1) are solved in double periodic box, in a Cartesian geometry where each side is set to $2\pi l_0$. We compute the nonlinear terms using a pseudo-spectral technique, applying a 2/3 dealiasing rule [55, 133]. The code conserves energy with high precision, and it has been tested in absence of viscous/resistive terms (the spectral Galerking representations retain high accuracy and robustness, even in ideal MHD). A standard Laplacian dissipation with constant dissipation coefficients has been employed.

The latter have been chosen high enough to guarantee the smoothness of the solutions, but also to achieve high Reynolds numbers. The values of the viscosity and the resistivity are reported in Table 4.1 together with a description of the runs performed. Time integration is achieved through a classical second-order Runge-Kutta method, which has been tested to be stable and robust, for each simulation. The number of used mesh points N^2 goes from 2048^2 to 4096^2, and results have been found to be independent of this choice.

Runs	N	$\nu = \eta$	M
$RUN1$	2048	3×10^{-4}	$M = 11$
$RUN2$	2048	2×10^{-3}	$M = 11$
$RUN3$	4096	5×10^{-4}	$M = 12$

Table 4.1: Parameters for runs: N represents the number of grid points in each direction, ν and η are the viscosity and the magnetic diffusivity respectively, M is related to N through $M = log_2(N)$

Considering the representation of magnetic and velocity fields in Fourier space, the energy is initially concentrated in the shell $1 \leq k \leq 2$ (k is the modulus of the wavenumber in units of $1/l_0$). The initial energy has been normalised such that $E = \frac{1}{2}\langle v^2 + b^2 \rangle = 1$, where the brackets denote a spatial average. Random phases are employed for the initial Fourier coefficients and uncorrelated, equipartitioned velocity and magnetic field fluctuations are imposed. This gives a negligible initial net cross helicity in the system. This choice of initial conditions corresponds in the physical space to a collection of energy containing magnetic islands and vortical flows. Therefore, the fields are a superposition of large scale fluctuations, which suddenly undergo a state of fully developed turbulence. As we have just outlined, using the normalisation described above, kinetic and magnetic Reynolds numbers of our simulations are nothing but the inverse of the kinematic viscosity and magnetic diffusivity respectively. Finally we have considered an homogeneous spatial grid (x_i, y_k), such that $x_i = i\ \delta x$ and $y_k = k\ \delta y$, with $1 \leq i, j \leq 2^M$ and $\delta x = \delta y = \delta = l_0\ 2^{-M}$ the mesh spacing.

4.2 Analysis

In order to identify the intermittent pattern formed at small scale in turbulent flow, we used a wavelet decomposition analysis, through a Haar wavelet base in two dimensions [49, 101, 44, 47, 46, 150, 151, 112] (use of the algorithm presented in section 3.3.2). In accordance with the wavelet decomposition, for $1 \leq m \leq M$, we define the scale $l_m = 2^{m-M} l_0 = 2^m \delta$ (Chapter 3).

The wavelet decomposition has been performed on both the two components of velocity and magnetic field, choosing the fields at a simulation time where the turbulence was fully developed, a time t^* which we have

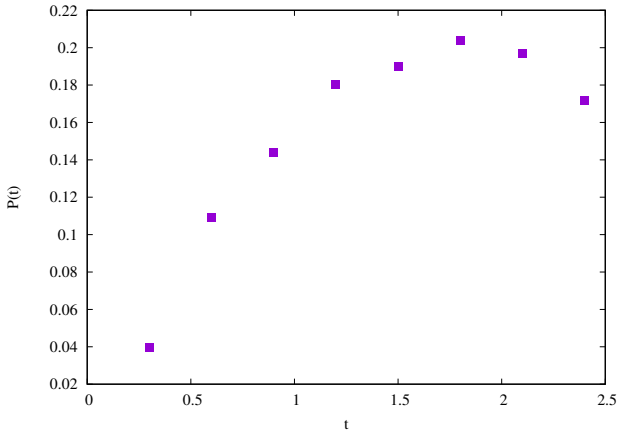

Figure 4.1: Dissipative power as a function of time, for $RUN3$. $P(t) = \eta < j^2(t) > + \nu < \omega^2(t) >$

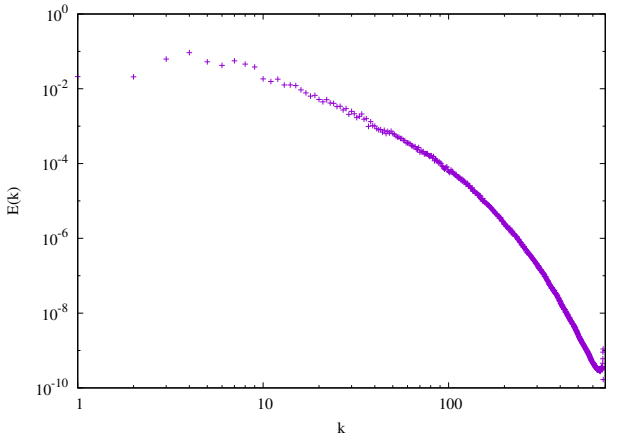

Figure 4.2: Energy spectrum in log scale for $RUN3$.

identified with the ideal time corresponding to the maximum value of the dissipated power (i.e. at this time the conditions of stationary state are valid since at the smallest scale the nonlinear effects are comparable with respect to the dissipative ones). For example, for $RUN3$ $t^* = 1.8$ (Figure 4.1) and the corresponding fully developed power spectrum is presented in Figure 4.2.

It is worth noting that at this time the field structure of the solution is completely different from that one found at the the starting time, showing that the solution of the MHD equations at this time has no particular relation with the imposed initial condition (Figure 4.5).

Figures 4.3 (a) and (b) report the invariants of the system (*i.e.* the global cross-helicity and the mean square magnetic potential) as functions of time. They both remain quasi-constant during all the rapid time evolution of the simulation ($RUN3$). Meanwhile Figure 4.4 presents the time evolution of

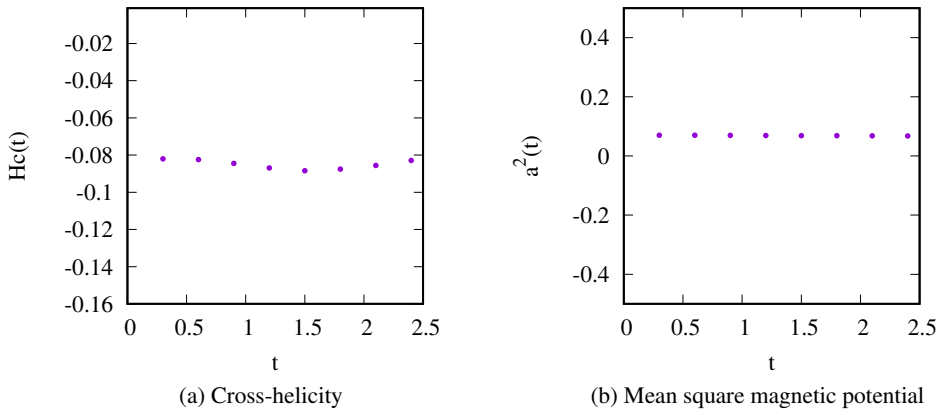

(a) Cross-helicity (b) Mean square magnetic potential

Figure 4.3: Invariants of the system in function of time for $RUN3$.

the total (magnetic and kinetic) energy, the magnetic energy and the kinetic energy. It is clearly seen that the dissipation rates for magnetic and kinetic energy are more or less the same up to the short time analysed.

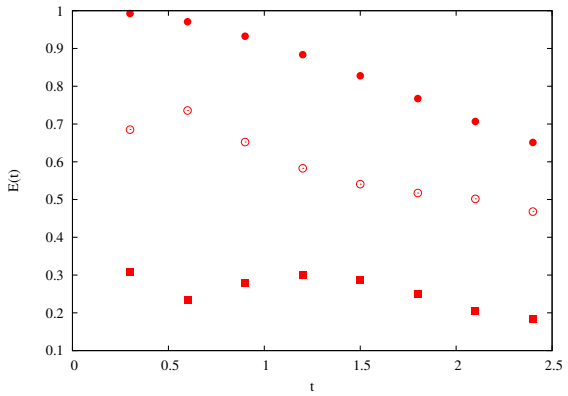

Figure 4.4: Total energy ●, kinetic energy ■, and magnetic energy ○ functions of time for $RUN3$.

As in an usual intermittent analysis [49], we have built up the PDFs of the velocity and magnetic wavelet coefficients at different scales. In Figure 4.6 the PDFs of the smallest scale (l_1) and of the largest statistically signif-

icant scale (l_8) are presented. Let us notice that, at the biggest considered scale (l_8), the PDF is almost Gaussian, while, descending to smaller scales, important non-Gaussian tails are displayed. Now the standard deviation at each scale can be used as a threshold for selecting the intermittent structures [49]. Actually, we have selected the wavelet coefficients of both the x and y components of the velocity and the magnetic field whose module is greater than four times the corresponding field standard deviation. This operation allows the identification of the grid points, at fixed scale, where coherent intermittent structures are localised (Figure 4.7).

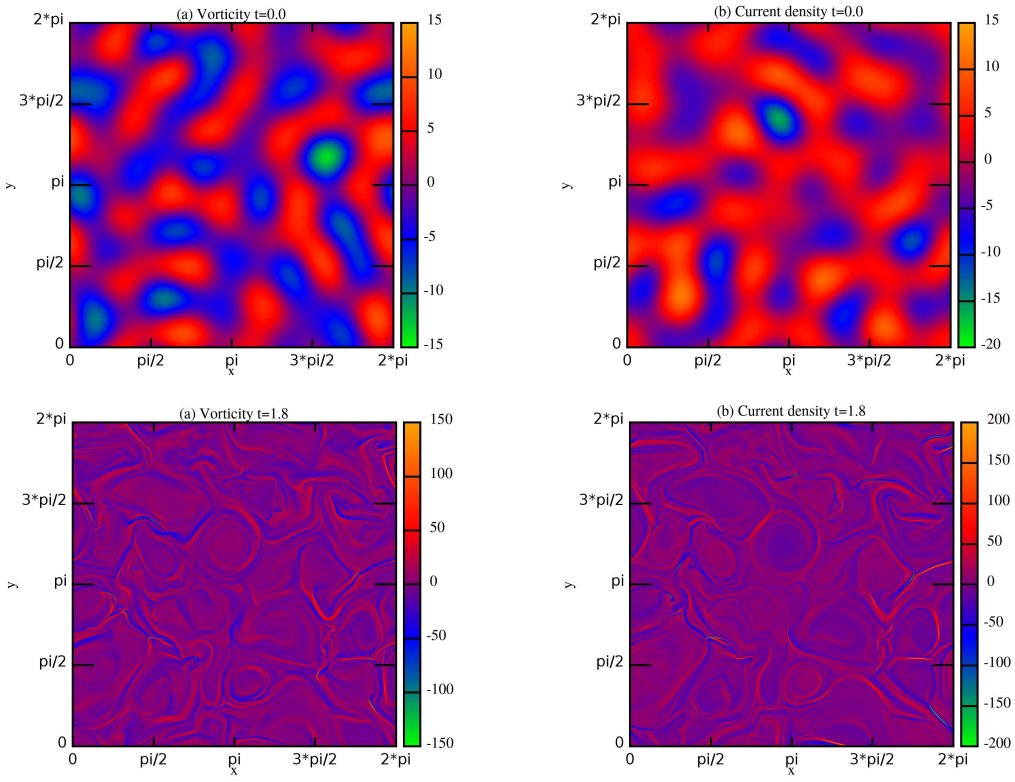

Figure 4.5: Contour plots of the vorticity field and the current field at times $t = 0.0$ and $t = 1.8$ for $RUN3$.

In order to study the properties of the correlation among the dynamical variables in the neighbor of each intermittent grid point (x_i, y_k) and for each scale l_m, we have considered such grid point as the center of a spatial window $[x_i - \Delta_m, x_i + \Delta_m] \times [y_k - \Delta_m, y_k + \Delta_m]$, with $\Delta_m = 2l_m$. Then we have restricted the vorticity field, the current density field and the magnetic potential to each selected spatial window and we have calculated the correlation coefficient between the current density field and the vorticity field $c^m_{\omega,j}(x_i, y_k)$ and correlation coefficient between the current density field and the magnetic potential $c^m_{j,a}(x_i, y_k)$ inside the above defined spatial windows.

In (Figure 4.8) the PDFs of $c^m_{\omega,j}(x_i, y_k)$ and $c^m_{j,a}(x_i, y_k)$ calculated at

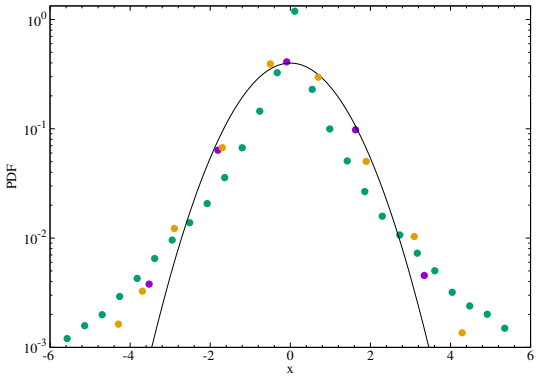

Figure 4.6: PDFs of v_x wavelet coefficients at scales l_1 •, l_7 • and l_8 • at simulation time $t = 1.8$ for $RUN3$, Gaussian Distribution −.

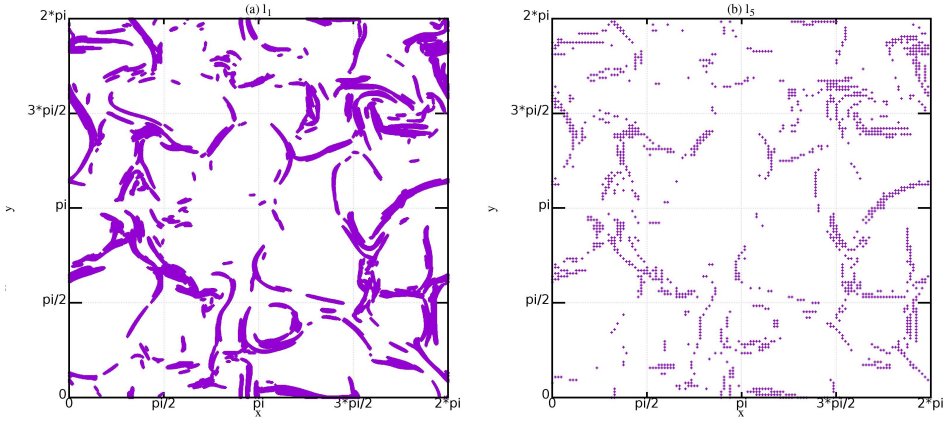

Figure 4.7: Grid points above-threshold at scales (a) l_1 and (b) l_5 at time $t = 1.8$ for $RUN3$.

$t = 1.8$ in the neighbourhood of the intermittent structures are compared with the distribution of their initial values calculated on the whole simulation domain. Looking at these distributions, we find that, in the simulation we are analysing, the correlations between the current density field and the vorticity field and the current density field and the magnetic potential(which were almost null everywhere in the simulation domain at the initial time) are displaying well defined values in the neighbourhood of the small scale intermittent structures after some ideal time. This shows that nonlinear interactions are extremely efficient in building up, rapidly in time and locally in the neighbourhood of the intermittent grid points, the correlations (4.0.4) predicted by the variational principle (4.0.2).

In addition, we have tested other correlations derived from the variation principle where quantities which do not represent quadratic rugged invariants for the system were kept constant (for example the vorticity field or $f(a) = a^n$ with $n > 2$). The obtained results have shown that these

correlations are not locally present in the flow.

The latter result has led us to repeat the same windowing analysis all over the simulation domain, i.e. for all grid points, and the previously used window of dimensions $(2\Delta_1) \times (2\Delta_1)$. Figures 4.9 display the same pattern observed in Figures 4.7, clearly identifying large scale and intermittent structures, both characterised by strong correlations between ω and j (Figure 4.9(a)) and between j and a (Figure 4.9(b)). Remarkably, the sign of the correlations in the large scale regions is the opposite of those in the more intermittent structures. Intermediate values of correlations are present only in the very tiny regions where correlations change in sign, i.e. there is a passage from -1 to $+1$ or vice versa.

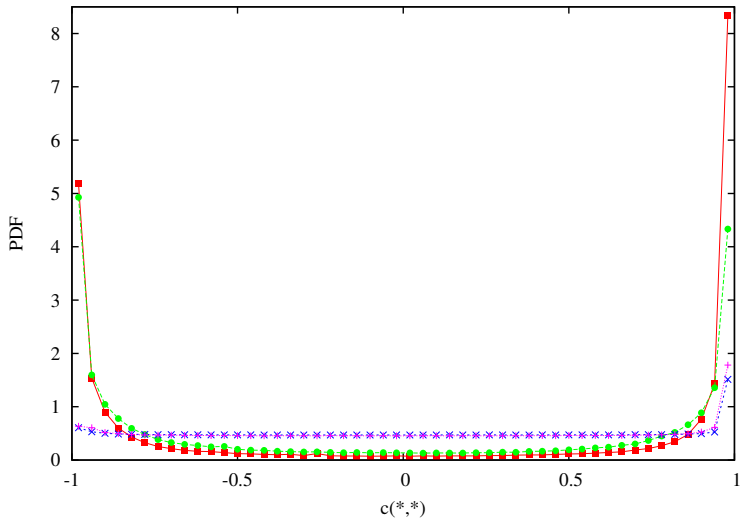

Figure 4.8: PDFs at scale l_1 of $c^m_{\omega,j}(x_i, y_k)$ ●, $c^m_{j,a}(x_i, y_k)$ ■ at time $t = 1.8$ calculated for the intermittent points and of $c^m_{\omega,j}(x_i, y_k)$ $+$, $c^m_{j,a}(x_i, y_k)$ $\times$ at time $t = 0.0$, calculated for the whole simulation domain, for $RUN3$.

It is worth noting that looking at the contour plots of the λ-values and φ-values given by relations (4.0.4) (Figures 4.10) the pattern obtained may be practically superposed on that obtained in Figures 4.9. Large regions of space where the former values are almost constant can be identified, while in the intermittent regions the values of the ratios remain almost constant on the pattern identified by the previous intermittent analysis.

These results are particularly significant since they allow us to understand what kind of role the rugged invariants' conservation plays during the nonlinear evolution of the 2D MHD equations. In the initial condition the correlations between velocity and magnetic field and between current density and magnetic potential were present nowhere. Due to the effects of nonlinear interactions the correlations calculated over the whole simulation domain remain null, but now in the flow there are regions of maximum positive correlations and regions of maximum negative correlations and

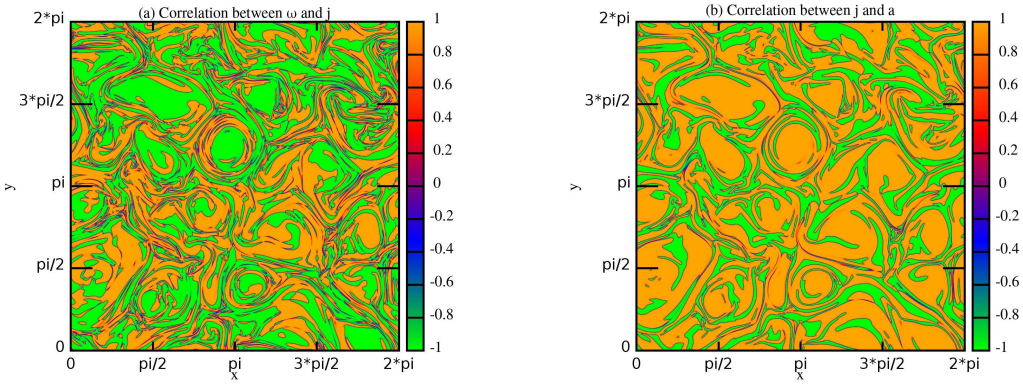

Figure 4.9: Contour plots of the correlation coefficients $c^m_{\omega,j}(x_i, y_k)$ (a) and $c^m_{j,a}(x_i, y_k)$ (b) at scale l_1 and time $t = 1.8$ for $RUN3$.

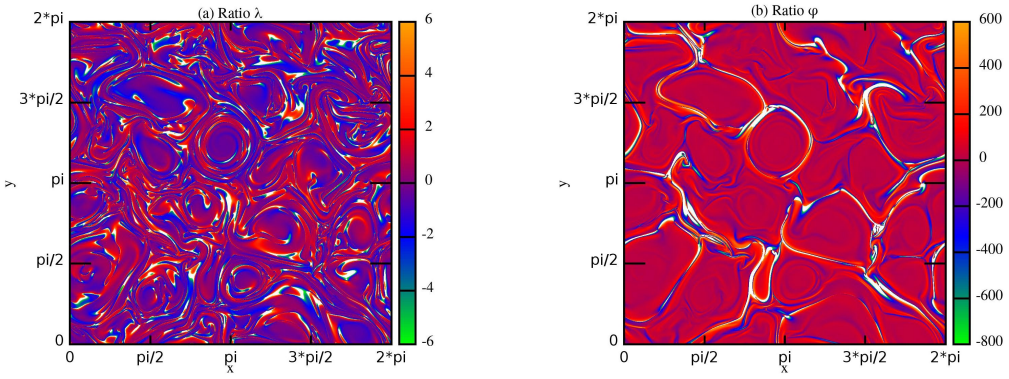

Figure 4.10: Contour plots of the ratios (4.0.4) at time $t = 1.8$ for $RUN3$.

the separation between these regions corresponds to a separation between large scale coherent structures and small scale intermittent structures. This means that the nonlinear interactions tend to segregate the structures with opposite sign of the correlations, not only in the physical space but also in the spectral space.

Starting from equations (4.0.1) for each grid point (x_i, y_k), we can define two typical evolution times for variables ω and a. The first type is the time measured by an observer located in a fixed point of the space, it is defined for the vorticity field and the magnetic potential as

$$\tilde{t}_\omega(x_i, y_k) = \left| \frac{\omega(x_i, y_k)}{\frac{\partial \omega}{\partial t}(x_i, y_k)} \right|, \qquad \tilde{t}_a(x_i, y_k) = \left| \frac{a(x_i, y_k)}{\frac{\partial a}{\partial t}(x_i, y_k)} \right|$$

The other one is the time measured by an observer moving on a flux line, hence following the motion. In this case the characteristic times associated to the dynamical evolution of the vorticity field and the magnetic potential

are

$$t_\omega(x_i, y_k) = \left| \frac{\omega(x_i, y_k)}{\frac{D\omega}{Dt}(x_i, y_k)} \right|, \qquad t_a(x_i, y_k) = \left| \frac{a(x_i, y_k)}{\frac{Da}{Dt}(x_i, y_k)} \right| \tag{4.2.5}$$

where $\frac{D*}{Dt} = \frac{\partial *}{\partial t} + \mathbf{v} \cdot \nabla *$ is the material derivative. It is worth noting that in order to identify a typical life-time of the turbulent structures under our investigation, the latter time is better suited than the former.

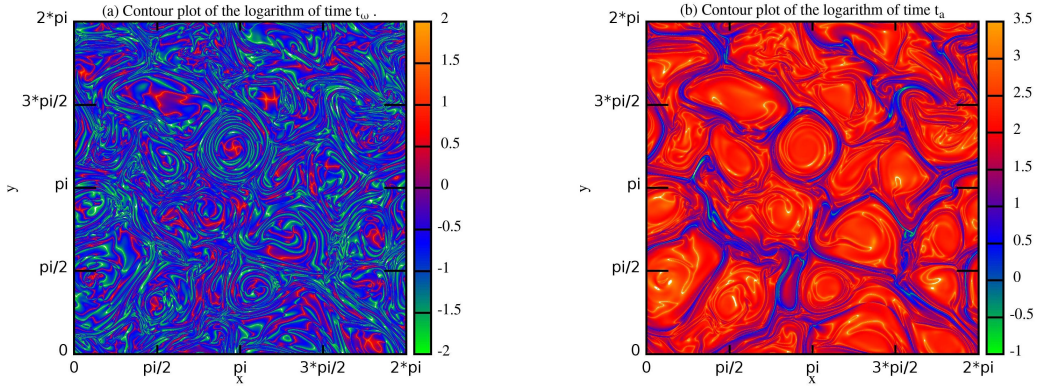

Figure 4.11: Contour plots of the characteristic times (4.2.5) at time $t = 1.8$ for $RUN3$.

In Figures 4.11 we have reported the contour plots of the life-times (4.2.5). The same pattern observed also in Figures 4.9, is displayed in Figures 4.11: large scale structures are characterised by long evolution times and may be sees as quasi-steady structures. On the contrary, the intermittent structures have rapid evolution in time, associated to their dissipation. This result together with the localization of opposite values of the correlations in the intermittent and in the quasi-steady structures can furnish a key for understanding why in decaying turbulence, on very long time, i.e. when small scale intermittent structures are finally dissipated, only one sign of the correlation at last survives on large scale structures (*self-organization*).

4.3 Discussion

Through our high resolution 2D MHD simulations we have analysed and identified the rapid time formation of coherent structures induced by nonlinear interaction in MHD incompressible turbulent flows. These structures are characterised by the occurrence at small scales of regions where the correlations predicted by the hypothesis of quadratic rugged invariant conservations are locally present, a property which is the equivalent to the well known "Beltramisation" of the fluid flows. Moreover, large scale structures and intermittent structures present a clear separation from the the

calculated correlations' point of view. In fact, the two different types of structures are characterised by opposite signs of the correlations.

Although, a limited number of simulations have been performed, we think that the peculiar initial conditions we have chosen and the high resolution we have used, allow us to be sufficiently confident about the fact that the behaviour observed and discussed represents a generic property of the 2D MHD turbulence.

Analysing the characteristic Lagrangian evolution times, other interesting properties of the coherent structures have emerged. Specifically, on very fast dynamic nonlinear time scales, local organization is observed; this is the case of intermittent structures which are formed when the small scales are produced by the nonlinear interactions and are then dissipated. Conversely, on long evolution time, global self-organization is observed. In fact, the large structures present very long evolution times, such that they can be considered quasi-steady structures. Consequently, leaving the simulation free to evolve, the rapid evolution finally destroys the intermittent structures, leaving only the large scale structures which are quasi-stable in time.

In ideal hydrodynamics the formation of singularities, i.e. the breakdown from smooth solutions, has necessary conditions given by the maximum norm of the vorticity (Beale-Kato-Majda theorem) [114, 2]. A similar behaviour is also observed for incompressible MHD equations: ideal MHD equations can be seen as the limit of the incompressible ones taking in consideration energy dissipation and magnetic helicity conservation (existence of a generalized Beale-Kato-Majda theorem) [13, 6]. Therefore it is worth speculating that the intermittent small scale structures, observed in our simulations as consequence of the rapid time evolution produced by nonlinear interactions, could give rise to singular weak solutions when letting the dissipative coefficients go to zero. In this case the properties of these structures, identified by our analysis, could give a key element for understanding which mathematical conditions characterise singularity emergence in weak solutions of the MHD ideal case.

Part II

Mode recognition in the Von-Karman Plasma experiment

Introduction

In this section a description of the data analysis performed on an ongoing experimental project, the Von-Kármán plasma (VKP) experiment, based in the Laboratoire de Physique at the Ecole Normale Supérieure de Lyon, is presented. This project is aimed at developing a Von-Kármán type flow in a weakly magnetised plasma in order to investigate the basic magnetic induction plasma-processes, with variable magnetic Prandtl number and magnetic Reynolds number. In Chapter 7 a concise description of the experimental set-up is given.

In order to get a better understanding of the internal dynamics characterising the plasma generated in the VKP experiment, the basic models for the plasma description are presented in Chapter 5. Then the low-frequency normal modes of magnetically confined plasma, the drift waves, are introduced and the equation describing the dynamics of an inhomogeneous plasma, the Hasegawa-Mima equation, is given (Chapter 6).

Finally, in Chapter 9, the data analysis built up in order to understand how the generated plasma column behaves when plasma dynamics characterised by the presence of drift wave modes occurs for magnetic field above a certain threshold is described. The extraction of the plasma modes has been obtained through the implementation of the two-dimensional variational mode decomposition analysis (Chapter 8). The results presented are still preliminary, but they show a good order of magnitude accordance between the plasma dynamic description given by the Hasegawa-Mima equation and the experimental data.

Chapter 5

Plasma description

A completely or partially ionised gas which is, however, electrically neutral on average is called plasma, and represents the forth state of the matter.
Plasmas occur vastly in nature. Examples are the non-fusion terrestrial plasmas (like neon signs, fluorescent lamps and willing arcs), the fusion-grade plasmas obtained using magnetic confinement devises (e.g. tokamaks, stellarators, reversed field pinches) and space plasmas.

The self-consistent interaction between electromagnetic fields and statistically large numbers of charged particles determines the plasma dynamics. This because charge separation between ions and electrons generates electric fields, while charged particle flow is responsible of currents and magnetic fields formation.

In principle knowing the trajectories and the velocities of all the charged particles allows to determine the time evolution of the plasma. In fact the previous informations can be used to evaluate both the electric and the magnetic fields through Maxwell's equations. Given now the instantaneous electric and magnetic fields, Lorentz equation allows to compute the forces acting on each charged particle, and to update the old trajectories and velocities.

However, it is impractical to follow this approach, due to complexity of the system described and the large number of charged particles involved. A more suited approach for describing the plasma dynamics is the introduction of appropriate simplifying approximations.
A model where a certain set of approximations are valid providing a self-consistent description is called regime. For plasmas usually two different categories of approximations can be considered involving either the electromagnetic field or the particle description.
In this part of the work we will focus on the latter, which can be either a kinetic (Vlasov theory) or a fluid (two-fluids or MHD theory) model.

Vlasov theory: an average over all the particles of a given species σ (ions or electrons) with the same velocity at a given location is performed; the plasma is characterised using the distribution function $f_\sigma(\boldsymbol{x}, \boldsymbol{v}, t)$, which is nothing but the phase-space density of particles of species σ

having velocity $\boldsymbol{v}$, position $\boldsymbol{x}$ at time t.

Two-fluids theory: an average over all particles of a given species at a given position is computed, and the plasma is characterised using the space density $n_\sigma(\boldsymbol{x}, t)$, the mean velocity $\boldsymbol{u}_\sigma(\boldsymbol{x}, t)$ and the pressure $p_\sigma(\boldsymbol{x}, t)$. This model approximates plasma as a system of two mutually interacting fluids, constituted by finite-pressure electrons and ions.

MHD theory: here the momentum is averaged over all particles of all species and the characterisation of the plasma is reached using the center-of mass density $\rho(\boldsymbol{x}, t)$, the center-of mass velocity $U(\boldsymbol{x}, t)$ and the pressure $P(\boldsymbol{x}, t)$. It is the less detailed model and it approximates plasma as a single, finite-pressure, electrically conducting fluid. The MHD theory can be obtained following a phenomenological approach as showed in Chapter 1, or through a more rigorous mathematical approach, starting from the two-fluids description.

For a more detailed description we refer to [3].

5.1 The kinetic description

In a three-dimensional space a particle, at a given time, can be identified by its position and velocity. Thus the instantaneous configuration of a large number of particles can be characterised by specifying the particles' density in each point of the phase space $(\boldsymbol{x}, \boldsymbol{v})$. The instantaneous density of particles in the phase space is the so called distribution function $f_\sigma(\boldsymbol{x}, \boldsymbol{v}, t)$. Therefore, $f_\sigma(\boldsymbol{x}, \boldsymbol{v}, t)d\boldsymbol{x}d\boldsymbol{v}$ is the number of particles at time t having positions in the volume element $d\boldsymbol{x}$ of the physical space and velocities in the volume element $d\boldsymbol{v}$ of the velocity space. If we consider the fluid description, the time evolution of f_σ gives a more detailed system description, in fact it permits the characterisation of particle classes with the same positions and velocities in phase space.

We observe that the number density of particles in the physical space is given by

$$n_\sigma(\boldsymbol{x}, t) = \int f_\sigma(\boldsymbol{x}, \boldsymbol{v}, t)d\boldsymbol{v} \tag{5.1.1}$$

and $f_\sigma(\boldsymbol{x}, \boldsymbol{v}, t)/n_\sigma(\boldsymbol{x}, t)$ can be seen as the probability that a random selected particle at position $\boldsymbol{x}$ has velocity $\boldsymbol{v}$ at time t. Consequently the mean (fluid) velocity can be defined as

$$\boldsymbol{u}_\sigma(\boldsymbol{x}, t) = \frac{1}{n_\sigma(\boldsymbol{x}, t)} \int \boldsymbol{v} f_\sigma(\boldsymbol{x}, \boldsymbol{v}, t)d\boldsymbol{v} \tag{5.1.2}$$

In general multiplying f_σ by different powers of the velocity and then integrating over the velocities gives us the moments of the distribution function.

We observe that if we consider the same frame of a particle with a phase-space trajectory $\boldsymbol{x} = \boldsymbol{x}(t)$, $\boldsymbol{v} = \boldsymbol{v}(t)$ and we measure the distribution function moving with the particle, the observed rate of change of f_σ is the quantity $\frac{D}{Dt} f_\sigma(\boldsymbol{x}(t), \boldsymbol{v}(t), t)$, where $\frac{D}{Dt}$ is the total derivative, *i.e.* the derivative measured in the moving frame. Because $\frac{D\boldsymbol{x}}{Dt} = \boldsymbol{v}$ and $\frac{D\boldsymbol{v}}{Dt}$ corresponds to the particle acceleration given by the Lorentz force, *i.e.* $\frac{D\boldsymbol{v}}{Dt} = \boldsymbol{a} = \frac{q_\sigma}{m_\sigma}(\boldsymbol{E} + \frac{1}{c}\boldsymbol{v} \times \boldsymbol{B})$ we have that

$$\begin{aligned} \frac{D}{Dt} f_\sigma(\boldsymbol{x}(t), \boldsymbol{v}(t), t)\Big|_{\text{orbit}} &= \frac{\partial f_\sigma}{\partial t} + \boldsymbol{v} \cdot \frac{\partial f_\sigma}{\partial \boldsymbol{x}} + \boldsymbol{a} \cdot \frac{\partial f_\sigma}{\partial \boldsymbol{v}} \\ &= \frac{\partial f_\sigma}{\partial t} + \boldsymbol{v} \cdot \frac{\partial f_\sigma}{\partial \boldsymbol{x}} + \frac{q_\sigma}{m_\sigma}\left(\boldsymbol{E} + \frac{1}{c}\boldsymbol{v} \times \boldsymbol{B}\right) \cdot \frac{\partial f_\sigma}{\partial \boldsymbol{v}} = 0 \end{aligned} \tag{5.1.3}$$

namely the distribution function measured when it is moving along a particle trajectory (orbit) is constant. This property is useful in the search of solutions for (5.1.3), in fact f_σ can be chosen to depend on any quantity that is constant along the orbit [78, 146].

In case of strong collisions an extra term should be added in the left side of (5.1.3), $\left(\frac{\partial f_\sigma}{\partial t}\right)_{\text{coll}}$. This term is a collision operator and it describes how the distribution function changes in time under the action of collisions (action of short-range interparticle forces). When strong collisions are included in (5.1.3), it is usually called *Boltzmann equation*.

Generally the rate of binary collisions in plasmas is relatively small, therefore in the case of sufficiently hot plasmas collisions are negligible and (5.1.3) is called *Vlasov equation*.

In order to have a closed set of equations that permits the self-consistent determination of the f_σ dynamics, equations for computing the electric and the magnetic fields present in the term $\boldsymbol{a} \cdot \frac{\partial f_\sigma}{\partial \boldsymbol{v}}$ should be added. These equations are the Maxwell's equations

$$\nabla \cdot \boldsymbol{E} = 4\pi \sum_\sigma q_\sigma \int f_\sigma d\boldsymbol{v} \tag{5.1.4}$$

$$\nabla \cdot \boldsymbol{B} = 0 \tag{5.1.5}$$

$$\nabla \times \boldsymbol{E} = -\frac{1}{c}\frac{\partial \boldsymbol{B}}{\partial t} \tag{5.1.6}$$

$$\nabla \times \boldsymbol{B} = \frac{4\pi}{c} \sum_\sigma q_\sigma \int \boldsymbol{v} f_\sigma d\boldsymbol{v} + \frac{1}{c}\frac{\partial \boldsymbol{E}}{\partial t} \tag{5.1.7}$$

Valsov-Maxwell equations represent a nonlinear system able to describe self-consistently the dynamics of a collisionless plasma analytically tractable.

5.2 The two-fluids description

The fluid approximation consists in considering the plasma composed by two or more interpenetrating fluids, one for each species (σ) forming the

plasma. The simplest case is when only one species of ions is considered and only two equations of motion are taken into account: one for the positively charged ion fluid and the second one for the negatively charged electron fluid.

Electron and ion fluids generate magnetic and electric fields (which can be described through Maxwell's equations). Therefore they interact with each other. In this plasma description the dynamic equation can be obtained considering the moments of Vlasov equation (5.1.3). Indeed integrate (5.1.3) over velocity for each species gives a set of partial differential equations where $n_\sigma(\boldsymbol{x},t)$ and $\boldsymbol{u}_\sigma(\boldsymbol{x},t)$ are also related.
The first step consists in computing the zero-th moment which corresponds to the species continuity equation

$$\frac{\partial n_\sigma}{\partial t} + \nabla \cdot (n_\sigma \boldsymbol{u}_\sigma) = 0 \tag{5.2.8}$$

Now multiplying (5.1.3) by $\boldsymbol{v}$ and integrating over velocity, we have the first moment of Vlasov equation which represents the momentum equation

$$m_\sigma \left[\frac{\partial (n_\sigma \boldsymbol{u}_\sigma)}{\partial t} + \frac{\partial}{\partial \boldsymbol{x}} \cdot (n_\sigma \boldsymbol{u}_\sigma \boldsymbol{u}_\sigma) \right] = n_\sigma q_\sigma (\boldsymbol{E} + \boldsymbol{u}_\sigma \times \boldsymbol{B}) - \frac{\partial}{\partial \boldsymbol{x}} \cdot \boldsymbol{P}_\sigma - \sum_{t \neq \sigma} \boldsymbol{R}_{\sigma\tau} \tag{5.2.9}$$

where:

- the sum is made on all the species $\tau \neq \sigma$, whose particles can collide with particles of species σ;
- $\boldsymbol{R}_{\sigma\tau} = -m_\sigma n_\sigma \nu_{\sigma\tau} (\boldsymbol{u}_\sigma - \boldsymbol{u}_\tau)$ is the momentum density transferred to species σ from species τ, with $\nu_{\sigma\tau}$ the collision frequency of species σ on species τ;
- $\boldsymbol{P}_\sigma$ is the pressure tensor defined as the second moment of Vlasov equation, *i.e.*

$$\boldsymbol{P}_\sigma = m_\sigma \int (\boldsymbol{v} - \boldsymbol{u}_\sigma) \otimes (\boldsymbol{v} - \boldsymbol{u}_\sigma) f_\sigma(\boldsymbol{x}, \boldsymbol{v}, t) d\boldsymbol{v}. \tag{5.2.10}$$

where $\otimes$ is the tensor product.

We observe that since the momentum density transferred from one species to the other one must obey momentum conservation, we have $\boldsymbol{R}_{\tau\sigma} = -\boldsymbol{R}_{\sigma\tau}$.

If f_σ is an isotropic function of $\boldsymbol{v}$, then $\boldsymbol{P}_\sigma$ is a diagonal matrix with diagonal terms all equal to

$$P_\sigma(\boldsymbol{x},t) = \frac{m_\sigma}{3} \int (\boldsymbol{v} - \boldsymbol{u}_\sigma) \cdot (\boldsymbol{v} - \boldsymbol{u}_\sigma) f_\sigma(\boldsymbol{x}, \boldsymbol{v}, t) d\boldsymbol{v} \tag{5.2.11}$$

In real system the distribution function is often anisotropic. In particular collisions drive the distribution function towards isotropy, while at the same

time competing processes tend to drive it to anisotropy. Therefore, for each system analysed one must determine if collisions are strong enough to guarantee the validity of the isotropic hypothesis.

Expanding the derivatives of the l.h.s. of (5.2.9) and using the continuity equation (5.2.8), we have that (5.2.9) is reduced to

$$n_\sigma m_\sigma \left[\frac{\partial \boldsymbol{u}_\sigma}{\partial_t} + (\boldsymbol{u}_\sigma \cdot \nabla)\, \boldsymbol{u}_\sigma\right] = n_\sigma q_\sigma \left(\boldsymbol{E} + \boldsymbol{u}_\sigma \times \boldsymbol{B}\right) - \nabla P_\sigma - \sum_{t \neq \sigma} \boldsymbol{R}_{\sigma\tau} \tag{5.2.12}$$

The term $\boldsymbol{v} \cdot \frac{\partial f_\sigma}{\partial \boldsymbol{x}}$ in (5.1.3) is responsible of the appearance of a moment of (n+1)-th order when a n-th moment of the Vlasov equation is considered. Thus, in order to obtain a closure for the fluid approximation system, an ad hoc procedure must be introduced. A typical hypothesis for the closure is to suppose that distribution functions are slightly perturbed Maxwellian.

Chapter 6

Turbulence in a plasma column

Let's consider dissipation effects in the strong-collisional plasma description. Dissipation can appear in both $\boldsymbol{v}$ space (collisional drag and velocity diffusion) and $\boldsymbol{x}$ space (Navier-Stokes-like equations). These effects are usually treated sequentially: first the effects of particle discreteness in the dissipative plasma collision operator $\left(\frac{\partial f_\sigma}{\partial t}\right)_{\text{coll}}$ (section 5.1) are introduced, then moments of the collisional kinetic equation lead to dissipative fluid equations [67].
In this configuration a generalised Boltzmann collision operator $C[f_\sigma]$ is introduced [19], in order to deal with the large-ranged nature of the Coulomb force. The form of $C[f_\sigma]$ depends mostly on whether the plasma is weakly- or strongly-coupled.

A measure of the effects of particle discreteness is represented by the plasma parameter

$$\epsilon_p = \frac{1}{n\lambda_D^3} \sim n^{\frac{3}{2}} T_e^{-\frac{3}{2}} \tag{6.0.1}$$

where n is the number density of electrons, λ_D is the Debye length and T_e is the electron temperature.
Using the plasma parameter the following distinction is possible.

- If $\epsilon_p \ll 1$, we talk of weakly coupled plasma [75]. Here the Debye sphere (sphere of radius λ_D) is populated by many particles, the ratio of both effective potential and thermal kinetic energy is small, and the plasma behaviour is similar to a continuous distribution of charge. Magnetically confined fusion plasmas are an example of weakly coupled plasmas [75].

- If $\epsilon_p \gtrsim 1$, we talk of strongly coupled plasma [76].

Before discussing plasma turbulence we present a discussion concerning the linear behaviour of plasmas (section 6.1). Then the basic low-frequency normal modes of magnetically confined inhomogeneous plasma, the drift waves,

are presented and the basic concepts of the nonlinear evolution equation for the electrostatic potential of the drift wave (the Hasegawa-Mima equation) are given (section 6.2). Finally a overview of weak turbulence description is shown (section 6.3).

6.1 Basic concepts of linear theory

Linear theory of plasmas presents more complications with respect to the neutral fluid one. In fact, in absence of background flows, for the incompressible Navier-Stokes equations the linear behaviour consists of only the viscous damping described by the linear momentum diffusion equation $\partial_t \boldsymbol{v} = \mu \nabla^2 \boldsymbol{u}$. Assuming that perturbations vary as $e^{\lambda t} = e^{-i\omega t}$ with $\omega = \Omega + i\gamma$, the previous equation asses that to each Fourier wave number $\boldsymbol{k}$ is associated the eigenvalue $\lambda_{\boldsymbol{k}} = -\mu k^2$.
In homogeneous plasmas such (fluid) eigenvalues are determined by the 3×3 dielectric tensor $\boldsymbol{D}(\boldsymbol{k}, \omega)$ [136].

Let's linearise the collisional kinetic equation (Boltzmann equation)

$$\partial_t \delta f + \boldsymbol{v} \cdot \nabla \delta f + \frac{q}{m} \left(\delta \boldsymbol{E} + \frac{1}{c} \boldsymbol{v} \times \delta \boldsymbol{B} \right) \partial_{\boldsymbol{v}} f = -\hat{C} \delta f \tag{6.1.2}$$

where f is the distribution function, $\partial_\bullet = \frac{\partial}{\partial \bullet}$, $\hat{C}$ is the linearised collisional operator, and mean fields have been ignored for simplicity. Then homogeneous self-consistent equations for the fluctuations $\delta \boldsymbol{E}$ and $\delta \boldsymbol{B}$ are sought. The corresponding dispersion relation becomes

$$\det \left[\boldsymbol{D}\left(\boldsymbol{k}, \omega\right) - \left(\frac{kc}{\omega} \right)^2 \left(\boldsymbol{I} - \hat{\boldsymbol{k}} \hat{\boldsymbol{k}} \right) \right] = 0 \tag{6.1.3}$$

where $\boldsymbol{I}$ is the 3×3 identity matrix.
In absence of a background magnetic field equation (6.1.3) presents both high-frequency solutions and a variety of low-frequency solutions. In the first case we talk of transverse ($\boldsymbol{E} \perp \boldsymbol{k}$) waves with dispersion relation $\omega^2 = k^2 c^2 + \omega_p^2$, where ω_p is the plasma frequency[1]. While in the second case the more common solutions are the longitudinal ones ($\boldsymbol{E} \parallel \boldsymbol{k}$), which are usually analysed in the electrostatic approximation $\boldsymbol{E} = -\nabla \phi$.

The presence of inhomogeneities (e.g. of density or temperature) considerably complicates the scenario. In fact in this case homogeneous modes can be strongly modified and new normal modes can appear.
Linear plasma theory suggests that the occurrence of linear waves in a plasma is a common phenomenon. Therefore, a *weak turbulence description*, *i.e.* a description in which normal modes are taken to be independent

[1] For species σ, $\omega_{p\sigma} = \left(\frac{4\pi n q^2}{m} \right)^{\frac{1}{2}}$, with n the species density, q the species charge and m the species mass; thus $\omega_p = \left(\sum_\sigma \omega_{p\sigma}^2 \right)^{\frac{1}{2}}$.

to the lowest order then coupled perturbatively, can be useful in better characterising the general plasma turbulence theory.

6.2 Drift waves and the Hasegawa-Mima equation

Real plasmas present both finite extent and gradients in different parameters, such as pressure, density, magnetic field etc. A finite-extent, magnetically confined[2] warm plasma necessarily exhibits a pressure gradient perpendicular to the magnetic field.
Let's consider an azimuthally symmetric cylindrical plasma (plasma column) immersed in a strong axial magnetic field $\boldsymbol{B} = B_0\hat{z}$ (Figure 6.1). We assume that the pressure profile is peaked on the z axis and falls off radially. Particles are free to move along the longitudinal direction, while in the perpendicular direction they are forced to make Larmor orbits (orbits of radius equals to the Larmor radius) around the magnetic field lines.

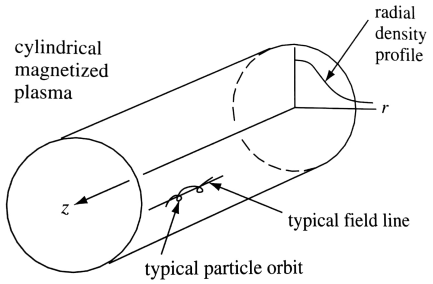

Figure 6.1: Cylindrical magnetised plasma with radial density gradient [3].

Let us analyse the system in term of a two-fluids description. From the two-fluids equation (5.2.12) the radial pressure gradient implies the following equilibrium force balance

$$0 = q_\sigma \boldsymbol{u}_\sigma \times \boldsymbol{B} - \frac{1}{n_\sigma}\nabla\left(n_\sigma k_B T_\sigma\right) \tag{6.2.4}$$

where the pressure has been computed using the ideal gas law, *i.e.* $P_\sigma = n_\sigma k_B T_\sigma$, with k_B the Boltzmann constant.
If we solve (6.2.4) for $\boldsymbol{u}_\sigma$ we have that each species has a steady-state perpendicular motion at the diamagnetic drift velocity

$$\boldsymbol{u}_{d\sigma} = -\frac{\nabla\left(n_\sigma k_B T_\sigma\right) \times \boldsymbol{B}}{q_\sigma n_\sigma B_0^2} \tag{6.2.5}$$

[2] In the presence of a magnetic filed, charged particles (ions and electrons) are forced to move into circular and helical orbits around the magnetic field lines. Thus the particles are tied to the field lines. Nevertheless, they are still free to move in the longitudinal direction of the lines. Therefore, a suitably shaped magnetic field cage can be able of confining a plasma and keeping it away from material walls.

in the azimuthal direction. In addition a corresponding diamagnetic drift current can be defined as follows

$$\boldsymbol{J}_d = \sum_\sigma n_\sigma q_\sigma \boldsymbol{u}_{d\sigma} = -\frac{1}{B_0^2}\sum_\sigma \nabla\left(n_\sigma k_B T_\sigma\right) \times \boldsymbol{B} = -\frac{1}{B_0^2}\nabla P \times \boldsymbol{B} \quad (6.2.6)$$

with $P = P_i + P_e$, P_i and P_e the ion and electron pressures respectively. This quantity is the azimuthal current associated with the MHD equation $\boldsymbol{j} \times \boldsymbol{B} = \nabla P$.

We notice that both electrons and ions exhibit a diamagnetic drift velocity providing the current necessary to establish the magnetic force that balances the MHD pressure gradient. Although, it has been observed that magnetised plasma with density and temperature (and thus pressure) gradients are unstable to a class of electrostatic modes called *drift waves* [143]. Even if these modes exist in the same frequency regime as MHD, they are not present in the standard MHD model. This because in the MHD model there is not a sufficiently detailed differentiation between electron and ion dynamics.

The study of drift waves is quite important, because these modes involve physical distinct electron and ion motions, magnetised warm plasma effects, density and pressure gradients, collisionality and Landau damping instabilities in a three-dimensional geometry [71]. In addition these waves are unstable in a lot of different configurations.

Hence the basic low-frequency normal mode of a magnetically confined plasma is represented by the electrostatic drift wave (also called universal mode), which is driven by the gradient of the backgorund density profile characteristic of a confined plasma configuration. Drift waves can also be destabilised by the presence of temperature gradients.

The basic nonlinear evolution equation for the electrostatic potential of the drift wave is the so-called *Hasegawa-Mima equation* [69, 72].

In order to derive the Hasegawa-Mima model, some assumptions are needed. Let's impose an homogeneous axial background magnetic field $\boldsymbol{B} = B_0\hat{z}$ and suppose that

- the plasma is inhomogeneous, $n_0 = n_0(x)$;
- the ion thermal balance equation is dropped, because the ions are cold and it is valid the temperature relation $T_i \ll T_e$;
- electrostatic approximation is valid, *i.e.* $\boldsymbol{E} = -\nabla\phi$;
- the background magnetic field is so strong that condition $\epsilon = \frac{1}{\omega_{ic}}\frac{\partial}{\partial t} \ll 1$[3] is valid;
- electrons follow a Boltzmann distribution, *i.e.* $n_i = n_e = n_0(x)exp\left(\frac{e\phi}{T_e}\right)$ where e is the elementary charge.

[3] $\omega_{ci} = \frac{q_i B_0}{m_i}$ is the ion cyclotron frequency.

Let's consider the continuity equation (5.2.8) and the moment equation (5.2.12) for the ions

$$\frac{\partial n_i}{\partial t} + \nabla \cdot (n_i \boldsymbol{u}) = 0 \tag{6.2.7}$$

$$n_i m_i \left[\frac{\partial n_i}{\partial t} + (\boldsymbol{u}_i \cdot \nabla) \boldsymbol{u}_i \right] = n_i q_i (\boldsymbol{E} + \boldsymbol{u}_i \times \boldsymbol{B}) - \nabla P_i - \nu_{ie} m_i n_i (\boldsymbol{u}_i - \boldsymbol{u}_e) \tag{6.2.8}$$

where anisotropy in the pressure tensor and friction have been neglected. Because we are in the electrostatic approximation and cold ions ($\nabla P_i \to 0$) have considered, we have that the ion motion equation (6.2.8) becomes

$$\frac{d\boldsymbol{u}_i}{dt} = \frac{\partial \boldsymbol{u}_i}{\partial t} + (\boldsymbol{u}_i \cdot \nabla) \boldsymbol{u}_i = -\frac{q_i}{m_i} \nabla \phi + \frac{q_i}{m_i} \boldsymbol{u}_i \times \boldsymbol{B} \tag{6.2.9}$$

Using the strong magnetic field hypothesis the term d/dt in (6.2.9) can be dropped in the first approximation, *i.e.*

$$-\frac{q_i}{m_i} \nabla \phi + \frac{q_i}{m_i} \boldsymbol{u}_i \times \boldsymbol{B} = 0 \tag{6.2.10}$$

Assuming that $\boldsymbol{u}_i \cdot \boldsymbol{B} = 0$ and taking the vector product of (6.2.10) with $\boldsymbol{B}$, we find out that the zero-order perpendicular ion motion in ϵ is just

$$\boldsymbol{u}_i^0 = -\nabla \phi \times \frac{\boldsymbol{B}}{B_0^2} \tag{6.2.11}$$

which is nothing but the $\boldsymbol{E} \times \boldsymbol{B}$ drift, $\boldsymbol{u}_E$.

In order to obtain a first-order correction in ϵ of (6.2.9), we replace the $\boldsymbol{E} \times \boldsymbol{B}$ drift in the left-hand side of (6.2.9) such that

$$\frac{\partial \boldsymbol{u}_i^0}{\partial t} + \left(\boldsymbol{u}_i^0 \cdot \nabla\right) \boldsymbol{u}_i^0 = \frac{q_i}{m_i} \boldsymbol{u}_i \times \boldsymbol{B} \tag{6.2.12}$$

and we consider the vector product of (6.2.12) with $\boldsymbol{B}$, so obtaining

$$\boldsymbol{u}_i^1 = \frac{1}{\omega_{ci} B_0} \left[-\frac{\partial}{\partial t} \nabla_\perp \phi - \left(\boldsymbol{u}_i^0 \cdot \nabla_\perp\right) \nabla_\perp \phi \right] \tag{6.2.13}$$

Thus the computed first-order correction is just the polarisation drift in the perpendicular direction, $\boldsymbol{u}_P$, where $\nabla_{||}$ has been neglected due to the fact that we assume parallel gradients much smaller than perpendicular ones.

Considering both the $\boldsymbol{E} \times \boldsymbol{B}$ drift and the polarisation drift, the total ion velocity is

$$\boldsymbol{u}_i = -\nabla \phi \times \frac{\boldsymbol{B}}{B_0^2} + \frac{1}{\omega_{ci} B_0} \left[-\frac{\partial}{\partial t} \nabla_\perp \phi - (\boldsymbol{u}_E \cdot \nabla_\perp) \nabla_\perp \phi \right] \tag{6.2.14}$$

Even if the polarisation drift is of order ϵ with respect to the $\boldsymbol{E} \times \boldsymbol{B}$ drift, it is still kept in the formulation because in the case of a uniform background magnetic field we have

$$\nabla \cdot \boldsymbol{u}_E = \nabla \cdot \left[-\nabla \phi \times \frac{\boldsymbol{B}}{B_0^2} \right] = 0, \quad \text{while } \nabla \cdot \boldsymbol{u}_P \neq 0. \tag{6.2.15}$$

In fact, it is the polarisation drift that allows changes in the ion density such that, in the electrostatic approximation, quasi-neutrality could be satisfied.

Let's now consider the continuity equation

$$\frac{\partial n}{\partial t} + n\left(\nabla \cdot \boldsymbol{u}\right) + \left(\boldsymbol{u} \cdot \nabla\right) n = 0 \;\Rightarrow \frac{dn}{dt} + n\left(\nabla \cdot \boldsymbol{u}\right) = 0 \tag{6.2.16}$$

$$\Rightarrow \frac{d\ln(n)}{dt} + \nabla \cdot \boldsymbol{u} = 0 \tag{6.2.17}$$

Using the adiabatic condition for the electrons we have $\ln(n) = \ln(n_0) + \frac{e\phi}{T_e}$, such that (6.2.16) can be written as

$$\frac{d}{dt}\left[\ln(n_0) + \frac{e\phi}{T_e}\right] + \nabla \cdot \boldsymbol{u} = 0 \tag{6.2.18}$$

We observe that the polarisation velocity can be neglected in the total derivative $\left(i.e. \frac{d}{dt}\bullet \simeq \frac{\partial}{\partial t}\bullet + (\boldsymbol{u}_E \cdot \nabla)\bullet\right)$, $\nabla \cdot \boldsymbol{u} = \nabla \cdot \boldsymbol{u}_P$ and $n_0 = n_0(x)$, thus (6.2.18) becomes

$$\frac{d}{dt}\left[\frac{e\phi}{T_e}\right] + \boldsymbol{u}_E \cdot \nabla \ln(n_0) + \nabla \cdot \boldsymbol{u}_P = 0 \tag{6.2.19}$$

Substituting both the expressions of the polarisation drift (6.2.13) and the $\boldsymbol{E} \times \boldsymbol{B}$ drift (6.2.11), and assuming a small potential $\left(\frac{e\phi}{T_e} \ll 1\right)$, we have

$$\frac{d}{dt}\left[\frac{1}{\omega_{ci} B_0}\nabla_\perp^2 \phi - \frac{e\phi}{T_e}\right] - \left(\boldsymbol{u}_E \cdot \nabla\right) \ln\left(n_0\right) = 0 \tag{6.2.20}$$

$$\Rightarrow \frac{\partial}{\partial t}\left[\frac{1}{\omega_{ci} B_0}\nabla_\perp^2 \phi - \frac{e\phi}{T_e}\right] + \left(-\nabla\phi \times \frac{\boldsymbol{B}}{B_0^2} \cdot \nabla\right)\left[\frac{1}{\omega_{ci} B_0}\nabla_\perp^2 \phi - \ln\left(n_0\right)\right] = 0 \tag{6.2.21}$$

Let's now introduce into (6.2.21) the following normalisation for the time scale, the distance scale and the potential respectively,

$$\omega_{ci}\, t \to t, \quad \frac{\boldsymbol{x}}{\rho_s} \to \boldsymbol{x}, \quad \frac{e\phi}{T_e} \to \phi \tag{6.2.22}$$

where $\rho_s^2 = \frac{T_e}{m_i \omega_{ci}^2}$ is the sound radius, consequently (6.2.21) becomes[4]

$$\frac{\partial}{\partial t}\left[\frac{1}{\omega_{ci} B_0}\frac{T_e}{e\rho_s^2}\nabla^2\phi - \phi\right] - \frac{1}{\omega_{ci}}\left[\left(\frac{T_e}{e\rho_s^2}\nabla\phi \times \frac{\hat{z}}{B_0}\right) \cdot \frac{1}{\rho_s}\nabla\right] \left[\frac{1}{\omega_{ci} B_0}\frac{T_e}{e\rho_s^2}\nabla^2\phi - \ln\left(n_0\right)\right] = 0 \tag{6.2.23}$$

Thus the Hasegawa-Mima equation is

$$\frac{\partial}{\partial_t}\left(\nabla^2\phi - \phi\right) - \left[\left(\nabla\phi \times \hat{z}\right) \cdot \nabla\right]\left[\nabla^2\phi - \ln\left(n_0\right)\right] = 0 \tag{6.2.24}$$

The latter is a non isotropic[5] second order nonlinear partial differential

[4] From now on the subscript $\perp$ will we omitted in the expression of the gradient due to the fact that the space variations are assumed to be just in the plane perpendicular to the imposed magnetic field.

[5] Since all the space derivatives are in the direction perpendicular to the $\hat{z}$-direction.

equation.

We look for plane waves solutions of the Hasegawa-Mima equations which propagate perpendicularly to both the background magnetic field and the inhomogeneous direction $\hat{x}$, *i.e.* solutions of the form $\phi = \phi(x)e^{i(k_y\ y-\omega t)}$.

Thus, neglecting the advective nonlinearity and assuming $k^2 \ll 1$, the dispersion relation of the drift wave is

$$\omega = \omega_k = -\frac{k_y \partial_x \ln(n_0)}{1+k^2} \tag{6.2.25}$$

Therefore, introducing the density gradient scale length L_n[6], the wave propagates with the diamagnetic drift speed

$$\boldsymbol{u}_d = \left[\frac{T_e}{eB_0}\left(-\partial_x \ln(n_0)\right)\right]\hat{y} = \left(\frac{1}{L_n}\frac{T_e}{eB_0}\right)\hat{y} \tag{6.2.26}$$

and electron diamagnetic frequency is

$$\omega_k = k_y\left(\frac{1}{L_n}\frac{T_e}{eB_0}\right) = k_y u_d = \omega_* \tag{6.2.27}$$

We point out that, in our case, the frequencies are real thus these waves are not unstable. Actually, it can be shown that taking into account either the collisional or the kinetic effects drift waves become unstable.

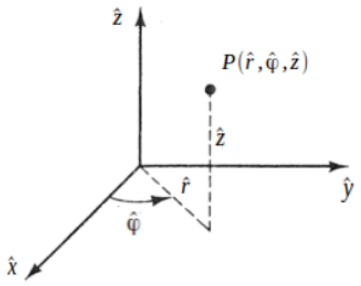

Figure 6.2: Cylindrical coordinates.

We want to redefine the obtained dispersion relation, representing the linear drift wave in a Cartesian geometry $(\hat{x}, \hat{y}, \hat{z})$, in the case of a cylindrical geometry, in order to describe the dynamics of a plasma magnetically confined in an infinite cylinder of radius $R > 0$. The new system of coordinates is individuated by $(\hat{r}, \hat{\varphi}, \hat{z})$, where $\hat{r}$ is the radial coordinate and $\hat{\varphi}$ the poloidal coordinate (Figure 6.2).

Without losing generality we can assume that on a circle of fixed radius $r < R$ in the plane $(\hat{r}, \hat{\varphi})$ (inhomogeneous direction) we have $\hat{r} \sim \hat{x}$ and $\hat{\varphi} \sim \hat{y}$ and that the fluctuations propagate only in the poloidal direction. Under these assumptions the relation between the wavenumber k_y and the

[6] $L_n^{-1} = -\partial_x \ln(n_0)$

wavelength λ is given by $\lambda = \frac{2\pi}{k_y}$. Thus, because we are in a confined geometry, we can suppose that the eigenmodes[7] are described by the following relation

$$2\pi r = n\lambda = n\frac{2\pi}{k_y} \Rightarrow k_y = \frac{n}{r} \tag{6.2.28}$$

where n is the eigennumber characterising the eigenmode (Figure 6.3).

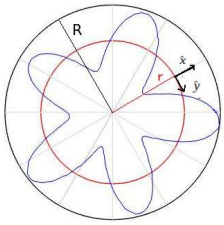

Figure 6.3: In the $(\hat{r}, \hat{\varphi})$ plane of an infinite cylinder with radius R, representation of both a circle of fixed radius r and a mode $n = 5$.

When $k_y L_n \gg 1$ we can assume that the mode profile variations in the $\hat{r}$ direction are negligible and we can suppose valid the dispersion relation (6.2.25). Therefore, using relation (6.2.28) in the dispersion relation (6.2.25) we have

$$\omega_k = \omega_n = \frac{n\, u_d}{r\left(1 + \frac{\rho_s^2}{r^2} n^2\right)} \tag{6.2.29}$$

6.3 Weak plasma turbulence

The weak plasma turbulence consists of a perturbative development of the fluctuating amplitude of the electrostatic potential ϕ in a small coupling parameter, followed by statistical averaging based on the random-phase approximation [83].

Here we don't show a straightforward derivation of the n-wave interaction theory, but we just present a phenomenological description in the case of wave-wave coupling.

Generally in linear systems the superposition principle affirms that wave modes are independent of each other, *i.e.* it is possible to excite or annihilate one mode without influencing any of the others.

In the case of confined plasmas, as soon as the drift wave perturbations reach finite amplitude, they can interact nonlinearly with perturbations of different wavenumbers, due to the presence of convective derivatives in the fluid conservation equations. As consequence disturbances develop at

[7] An eigenmode of an oscillating system is a pattern of motion in which all parts of the system move sinusoidally with the same frequency and with a fixed phase relation. The frequency for a particular mode is called the eigenfrequency. A description of the amplitudes and phases of the various parts is called the mode shape. A system will typically have discrete modal frequencies and associated mode shapes. In case of linear systems the arbitrary motion can be expressed as a linear combination of different modes [48].

other wavenumbers and, because some of them are linearly stable, they are damped. In the limit of very weak parallel electron dissipation, this process can be described through a set of coupled mode equations [143].
In fact, let's assume that the electrostatic potential in the Fourier domain is

$$\phi = \frac{1}{2} \sum_{\boldsymbol{k}} \left[\phi_{\boldsymbol{k}}(t)\, e^{i\boldsymbol{k}\cdot\boldsymbol{x}} + \text{ c.c. } \right] \tag{6.3.30}$$

where c.c. stands for the complex conjugate of the previous term. Substituting the new expression of ϕ in the Hasegawa-Mima equation (6.2.24) we have the following coupling evolution equation

$$\frac{d\phi_{\boldsymbol{k}}}{dt} + i\omega_{\boldsymbol{k}}\phi_{\boldsymbol{k}} = \sum_{\boldsymbol{k}+\boldsymbol{k}_1+\boldsymbol{k}_2=0} \Lambda^{\boldsymbol{k}}_{\boldsymbol{k}_1\boldsymbol{k}_2} \phi^*_{\boldsymbol{k}_1} \phi^*_{\boldsymbol{k}_1} \tag{6.3.31}$$

where $\phi^*_{\boldsymbol{k}_\star}$ is the complex conjugate of $\phi_{\boldsymbol{k}_\star}$ and the matrix $\Lambda^{\boldsymbol{k}}_{\boldsymbol{k}_1\boldsymbol{k}_2}$ denotes the coupling (Figure 6.4), such that

$$\Lambda^{\boldsymbol{k}}_{\boldsymbol{k}_1\boldsymbol{k}_2} = \frac{1}{2} \frac{1}{1+k^2} (\boldsymbol{k}_1 \times \boldsymbol{k}_2) \cdot \hat{z} \left[k_2^2 - k_1^2\right] \tag{6.3.32}$$

Condition $\boldsymbol{k}+\boldsymbol{k}_1+\boldsymbol{k}_2 = 0$ can be seen as a consequence of the conservation of wave momentum during the considered interaction.

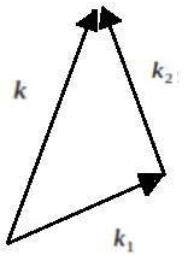

Figure 6.4: Wave-wave coupling.

The described mode coupling can exhibit a turbulent behaviour somehow similar to the case of the MHD turbulence described in Chapter 2.

Chapter 7

The Von-Kármán Plasma experiment

In this chapter we briefly present an ongoing experimental project: the Von-Kármán plasma (VKP) experiment. This project is aimed at developing a Von-Kármán type flow[1] in a weakly magnetised plasma in order to investigate the basic magnetic induction plasma-processes, with variable Prandtl number[2] and magnetic Reynolds number of the order of 10. In this case the flow is forced in a linear device by a $\boldsymbol{j} \times \boldsymbol{B}$ torque (with $\boldsymbol{j}$ the current density and $\boldsymbol{B}$ the magnetic field) using emissive cathodes[3].

This project represents a complementary work to the ongoing studies carried on at UW Madison on stirring large-scale unmagnetised plasmas in both the Plasma Couette experiment [24] and the Madison Plasma Dynamo Experiment [27].

The principal scientific objectives of the VKP project are

- extend the studies on both turbulent MHD processes and dynamo instabilities from very low Prandtl numbers ($\sim 10^{-6}$) to larger values (~ 10);
- investigate the plasma dynamics and the plasma parameter fluctuations that arise in the presence of large-scale driven flows (ex. rotation);
- a comprehensive investigation of transport plasma processes in weakly magnetised, partially ionised plasmas.

[1] Von Kármán swirling flow is a flow created by a uniformly rotating infinitely long plane disk. It is a steady flow in which vorticity generated at a solid surface is prevented from diffusing far away by an opposing convection [152].

[2] The Prandtl number P_M is defined as the ratio of the kinematic viscosity over the magnetic diffusivity.

[3] A cathode electrode in a vacuum tube consists in a metal surface which emits electrons into the tube. In a hot (emissive) cathode, the cathode surface is induced to emit electrons by heating it with a filament, a thin wire of refractory metal (ex. tungsten) with current flowing through it.

For a more detailed description of the project we refer to [117].

In the next paragraph a description of the experimental device (built up to now) is given.

7.1 The experimental set-up

The VKP experimental set-up consists of a cylindrical vacuum vessel of 0.2 m in diameter and 1 m in length, with a plasma source at one end of the cylinder. The plasma source used is a cylindrical pyrex tube with an internal diameter of 110 cm around which a 3 turns radio-frequency coil is sustained by a 13.56 MHz radio-frequency power generator. The supplied power may vary from 1 kW to 3.3 kW (no magnetic field is observed below 1 kW). A turbo-molecular pump maintains a base pressure of 10^{-5} Pa. The Argon gas plasma used here usually requires pressure in the range of $10^{-2} - 30$ Pa. A high density plasma column along the axial direction is generated by the coupled action of both the radio-frequency source and Bitter three-loops coils, which provide an axial magnetic filed up to 0.2 T. An induced electric field can be observed along the three-loops and acceleration of the electrons composing the plasma and ionizing collisions with neutrals are obtained. The gas present in the vessel is partially ($\sim 30\%$) singly ionised. Schematic images of the current set-up are shown in Figure 7.1 Typical plasma parameters of the current stage device are presented in Table 7.1.

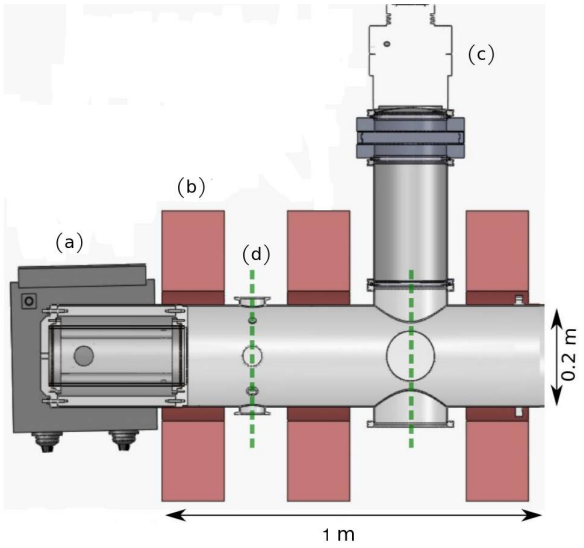

Figure 7.1: Current stage of the VKP experimental set-up: (a) radio-frequency source, (b) Bitter coils, (c) turbo pump, (d) port for the emissive cathode.

Looking at the typical radial profiles of the plasma density and the electron temperature, gradients are mainly visible at the edge of the plasma

Parameters	Values	Units
Plasma density (n)	$10^{16} - 5.0 \cdot 10^{18}$	m^{-3}
Electron temperature (T_e)	$2 - 6$	eV
Ion temperature (T_i)	$0.1 - 1$	eV
Electron density (n_e)= Ion density (n_i)	$5 \cdot 10^{17} - 15 \cdot 10^{17}$	part/m^3
Ionisation friction ($f_{\%}$)	$0.1 - 30$	%
Magnetic field (B_0)	$5 - 200$	mT
Flow velocity (U)	$0 - 3$	km/s

Table 7.1: Typical plasma parameters of the current experiment set-up.

column.

Preliminary work on the VKP experiment has been focused on both the optimisation of the flow driven by the injected current of the highly emissive cathodes, and the understanding of the physical parameters influencing the flow velocity (transport coefficients, drag from collisions between ions and neutrals).

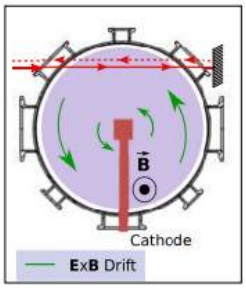

Figure 7.2: Sketch of the emissive cathode inserted in the center of the vessel [41].

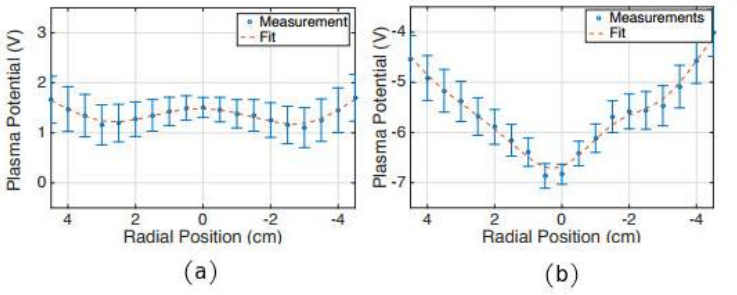

Figure 7.3: Plasma potential profile plot: (a) no emissive cathode inserted in the vessel, (b) emissive cathode inserted in the center of the vessel [41].

It is well know that the magnetised plasma columns naturally rotate due to drifts: either the $\boldsymbol{E} \times \boldsymbol{B}$ drifts, which arise from the radial gradient

of plasma potential (perpendicular to the axial magnetic field) or the diamagnetic drift, arising from the radial gradient of plasma pressure. This natural rotation of the plasma column is capable of exciting different instabilities.
The strong modification of the plasma rotation, which in the presented set-up is mainly driven by the diamagnetic current, may suppress or enhance such instabilities, usually identified as drift waves. Therefore the aim of the current experimental project is to study in details how controlled plasma flows influence such instabilities.
Some earlier tests have shown that inserting a hot emissive cathode in the center of the vessel and biased it negatively at several tens of Volts, such that is emits around 10 A in the vessel (Figure 7.2), an important modification of the plasma potential profile is displayed: from the typical w-shape plasma potential profile passes to a v-shape profile (Figure 7.3) . This causes an increase in the gradients in the center of the vessel and a modification of the natural rotation of the column into a rigid one rotation.

7.2 Plasma diagnostics

In this paragraph two different diagnostic types are shortly presented: the intrusive diagnostic and the fast imaging one.

7.2.1 Intrusive diagnostic

In order to measure the plasma parameters, intrusive probes has been used. This type of diagnostics has been introduced because the relatively low plasma density and temperatures allow a long-time exposure of the probes. A Langmuir probe permits detection of the plasma density, the electron temperature, the plasma potential and the floating potential. Emissive probes have also been used to measure the plasma potential.

A Langmuir probe is a device used to determine several fundamental parameters of a plasma, such as the electron temperature, the electron density, and the electric potential. It consists of placing one or more electrodes into a plasma with a constant time-varying electric potential between the various electrodes or between them and the surrounding vessel [20].

Let the plasma potential (space potential) be V_s, and let V_p be the potential applied to the probe. Comparing V_p and V_s different behaviours can be observed. When $V_p >> V_s$, an electron current I_e is collected and a negative probe current can be observed. Otherwise, when $V_p << V_s$, an ion current I_i is collected. It is customary to plot I–V characteristic curves with I_e positive and I_i negative.

Looking at Figure 7.4 we notice that the space potential V_s is near the knee of the curve. The ion saturation current I_{sat} is reached when all the electrons have been repelled and it can be found at the far left. When ion and electron currents are equal and the net current is zero, we have the

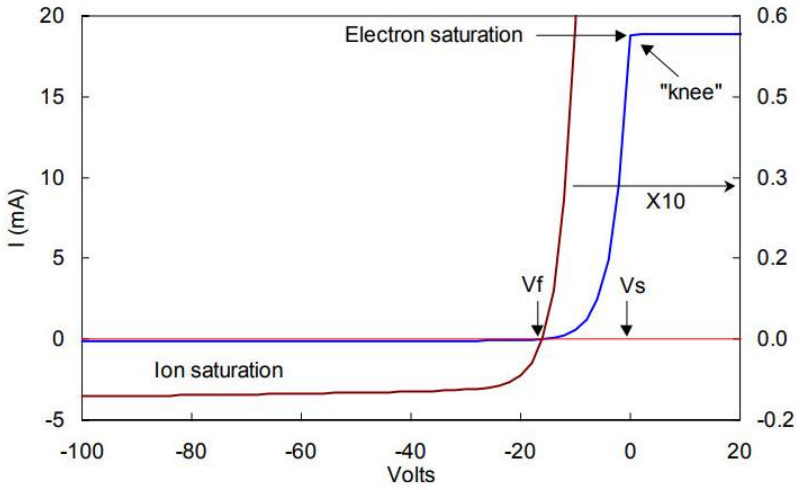

Figure 7.4: Ideal I-V curve [20].

floating potential V_f. In the transition region, the ion current is negligible, and the electrons are partially repelled by the negative potential $V_p - Vs$. In a Maxwellian plasma, this part of the curve is exponential. When V_p reaches V_s, the totality of electron random thermal flux is collected and the electron saturation region begins. In such region I_e grows slowly because of the expansion of the sheath.

Starting from the I-V curve, it is possible to determine the plasma density n, the electron temperature KT_e, and the plasma potential V_s, but not the ion temperature. The most common way to obtain the space potential is to draw straight lines through the I–V curve in the transition and electron saturation regions and call the crossing point V_s, I_{es}. Although, this technique can give raise to some problems, (ex. when I_{es} is curved this method gives wrong results, collisional case). Therefore, the best way to measure the plasma potential is to use a hot or an emissive probe.

An emissive probe is an electrostatic probe formed by an exposed electrode heated either electrically or by the direct expose to the plasma [134]. Emissive probes measure directly neither temperature nor density of the plasma but they represent the best choice for plasma potential measurements. When an emitting probe is biased more negatively than the plasma potential, the electrons can be emitted from the probe into the plasma. Instead, when it is biased more positively than the plasma potential, the majority of the electrons cannot be emitted. Taking into account the parameter ξ, which represents the probe bias normalised to the wire temperature (T_w) for the emitter graph and the plasma electron temperature (T_e) for the collector graph, it is possible to compare emitting and collection probe current vs. bias voltage. This shows why the emissive probes can determine the plasma potential more precisely. In the case of the emissive probe, if $\xi > 0$, the current decreases exponentially with the slope of the logarithmic plot proportional to $1/T_w$, and, if $\xi < 0$, all the electrons

emitted from the probe will enter the plasma and be observed as emitted current. Otherwise considering the collecting probe, if $\xi < 0$, the current exponentially increases and the semilog slope is proportional to $1/T_e$ and, when $\xi > 0$, all electrons entering the probe sheath are collected. Therefore, emissive probes have an exponential region depending on T_w, while, for collecting probe, this region depends on T_e. Since in most plasmas $T_w << T_e$, emissive probes can measure the plasma potential in a more appropriate way.

7.2.2 Fast imaging diagnostic

The intrusive diagnostic described before presents a key problem: when an electrostatic probe is inserted into the cylindrical vessel it interacts with the plasma generating disturbances and modifications in the plasma dynamics. Therefore, a less intrusive method for detecting the plasma density fluctuations is necessary. To this purpose, a high speed camera[4] has been installed in the experimental set-up. It is located on the top of the experiment, and two mirrors have been installed in order to parallelise as much as possible the line view of the emitted light (Figure 7.5). The high speed camera captures the visible light fluctuations emitted by the plasma at acquisition frequencies of several dozen kHz.

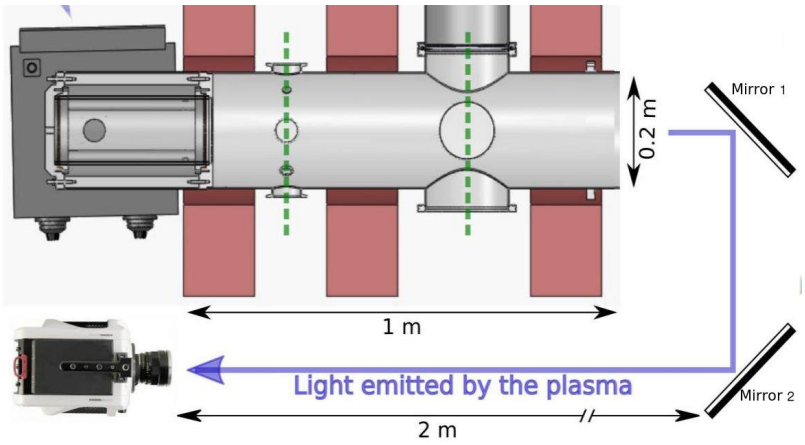

Figure 7.5: Experimental set-up improved with the fast camera and two mirrors.

[4] Model Phantom v2511. A single recorded frame is of 256×256 pixels.

Chapter 8

The two-dimensional variational mode decomposition

The two-dimensional variational mode decomposition (2D-VMD) is a method that allows to adaptively decompose an image into different modes, characterised by separate spectral bands. The 2D-VMD model permits the extraction of modes occurring simultaneously. In fact, it searches for a fixed number of 2D modes and their respective center frequencies, such that the bandlimited modes reproduce the input image (exactly or in least-squares sense) [153].

The main idea is to decompose images into ensembles of constituent modes (or components), called intrinsic mode functions (IMF), that have specific directional and oscillatory characteristics, i.e. limited bandwidth around their characteristic center frequencies. In fact, they can be seen as amplitude- and frequency-modulated (AM-FM) 2D signals. Even if several modes overlap in space or have limited spatial support (local instantaneous frequency and amplitude vary smoothly), an ensemble of modes should permit the reconstruction of a given input image up to noise and singular features.

The problem is inspired by the one-dimensional empirical mode decomposition (EMD) algorithm [74] and its successive extensions [99, 125, 138, 73], which permits the decomposition of any complex data set into a finite and often small number of intrinsic mode functions that admit well-behaved Hilbert transforms. This decomposition method can be extended to the two-dimensional case through the 2D-EMD [110]. It involves recursive sifting (extracting of oscillatory modes) of 2D spatial signals by interpolating upper and lower envelops and averaging the result with median envelopes, in order to extract image components in different frequency bands. Similarly to the EMD, the 2D-EMD has several weaknesses: the extremal point finding, the interpolation of envelops and the stopping criteria involved.

Classical decomposition methods include the discrete Fourier transform

and the continuous wavelet transform (chapter 3), where a fixed basis is imposed in order to find a sparse representation.

Other approaches more specific to directional image decomposition mainly involve rigid frames, decomposing the Fourier spectrum into mostly or strictly disjoint (quasi)-orthogonal fixed basis functions. (e.g. Gabor filter [86], wavelets [30, 38], curvelets [14]). These approaches have the problem of non-adaptation and it can happen that several different image components are contained in the same band.

In this context, important improvements have been obtained using synchrosqueezed wavelet transforms [23], where the exceeding wavelet informations are removed by energy content thresholds.

In order to obtain a model capable of providing a solution to the signal decomposition problem which guarantees both a well founded mathematical background and a sufficiently easy implementation, the one-dimensional variational mode decomposition (VMD) has been introduced [40]. The VMD method is based on the well-established concepts of Wiener filtering, 1D Hilbert transform and analytic signal, and heterodyne demodulation, in order to obtain a decomposition of an input signal into a discrete number of sub-signals (modes). Each mode has limited bandwidth in the spectral domain, i.e. each mode $u_k : \mathbb{R} \to \mathbb{R}$ is required to be compact as much as possible around a center pulsation ω_k determined along with the decomposition.

A natural extension of the VMD approach in the context of image segmentation and directional decomposition is the two-dimensional VMD [153]. From a technical point of view, the 2D-VMD algorithm is a non-recursive, fully adaptive, variational method which sparsely decomposes images with minimal parameters and no explicit interpolation in a robust mathematical manner.

Let's observe that the approach under study can be applied to any data subset whose variables are either spatial or temporal.

8.1 Basic concepts

Definition 8.1.1. *Intrinsic mode functions (IMF) are amplitude- and frequency-modulated signals (AM-FM) that can be written as*

$$u_k(t) = A_k(t)\cos\left(\phi_k(t)\right) \tag{8.1.1}$$

where the phase $\phi_k(t)$ is a non-decreasing function, i.e. $\phi_k'(t) \geq 0$*, and the envelope $A_k(t)$ is non-negative.*

It is important to observe that both the envelope and the instantaneous frequency, $\omega_k(t) := \phi_k'(t)$, vary much slower than the phase ϕ_k [31, 56]. This means that, considering an interval somewhat longer than $[t-\delta, t+\delta]$ with $\delta \approx 2\pi/\phi_k'(t)$, the mode $u_k(t)$ can be seen as a pure harmonic signal with amplitude $A_k(t)$ and instantaneous frequency $\phi_k'(t)$. An immediate consequence of this property is the limited bandwidth of the IMF.

In order to present both one- and two-dimensional VMD models, a brief review of few concepts and tools from signal processing are needed.

Consider the observed signal $f_0(t)$ to be a copy of the original signal $f(t)$, affected by additive zero-mean Gaussian noise n, *i.e.*

$$f_0 = f + n \tag{8.1.2}$$

The problem consists in recovering the original signal $f(t)$ starting from the known $f_0(t)$ (typical ill-posed inverse problem) [4]. If we assume that both the signal and the additive noise are stationary linear stochastic process, the noise-free signal can be estimated using the following Tikhonov regularised minimisation problem [140, 107]

$$\min_f \{||f - f_0||_2^2 + \alpha ||\partial_t f||_2^2\} \tag{8.1.3}$$

with $||\cdot||_2$ the L^2-norm.
This minimisation problem represents a Gaussian regularised minimum mean squares problem. The associated Euler-Lagrange equations are $f - f_0 = \alpha \partial_t^2 f$, and they are typically solved in the Fourier domain

$$\hat{f}(\omega) = \frac{\hat{f}_0}{1 + \alpha\omega^2} \tag{8.1.4}$$

where

$$\hat{f}(\omega) := \mathcal{F}\{f(\cdot)\}(\omega) = \frac{1}{\sqrt{2\pi}} \int_{\mathbb{R}} f(t) e^{-i\omega t}\, dt, \quad i^2 = -1$$

is the Fourier transform of the one-dimensional signal $f(t)$.

We observe that the recovered signal f (8.1.4) is a low-pass narrow-band selection of the input signal f_0 around the frequency $\omega = 0$. Indeed the solution corresponds to a convolution with the Weiner filter, where α is the variance of f [147, 59].

Definition 8.1.2. *The Hilbert transform of a 1D signal $f : \mathbb{R} \to \mathbb{R}$ is the linear operator*

$$\begin{aligned} \mathcal{H}\{f\}(t) &:= \left\{ \frac{1}{\pi s} * f(s) \right\}(t) = \frac{1}{\pi}\, p.v. \int_{\mathbb{R}} \frac{f(s)}{t - s}\, ds \\ &= -\frac{1}{\pi} \lim_{\epsilon \to 0} \int_{\epsilon}^{\infty} \frac{f(t+s) - f(t-s)}{s}\, ds \end{aligned} \tag{8.1.5}$$

with p.v. denoting the Cauchy principal value of the integral and $*$ the convolution [66].

One of the most important applications of the Hilbert transform is in the construction of an analytic signal starting from a purely real signal [52].

Definition 8.1.3. *The analytic signal of a purely real signal $f : \mathbb{R} \to \mathbb{R}$ is defined as*

$$\begin{aligned} f_{AS} : \quad & \mathbb{R} \to \mathbb{C} \\ & f_{AS}(t) \mapsto f(t) + i\mathcal{H}\{f\}(t) = A(t)e^{i\phi(t)} \end{aligned} \tag{8.1.6}$$

where $\mathcal{H}$ represents the 1D Hilbert transform of f.

Therefore, the real signal is recovered taking the real part of the analytic signal.
In (8.1.6) the complex exponential term $e^{i\phi(t)}$ is a phasor individuating the rotation of the complex signal in time with phase $\phi(t)$, while the envelope $A(t)$ governs the amplitude of the complex signal. This definition is useful in the analysis of time-varying amplitude and instantaneous frequency $\omega(t) = \frac{d\phi(t)}{dt}$.

It is possible to rewrite definition (8.1.6) in the spectral domain. In fact, observing that the Hilbert transform is a multiplier operator, i.e.

$$\mathcal{F}\{\mathcal{H}\{f\}\}(\omega) = (-i\ sign(\omega))\hat{f}(\omega) \tag{8.1.7}$$

the definition of the analytic signal in the spectral domain is given by the unilateral spectrum

$$\hat{f}_{AS}(\omega) = \begin{cases} 2\hat{f}(\omega) & \text{if } \omega > 0 \\ \hat{f}(\omega) & \text{if } \omega = 0 \\ 0 & \text{if } \omega < 0 \end{cases} \tag{8.1.8}$$

Thus the analytic signal in the spectral domain has the property of suppressing the negative frequencies. The single-sidedness of the analytic signal spectrum allows easy frequency shifting to baseband by complex exponential mixing.
In order to reproduce this property in the n-dimensional case, a half-space of the frequency domain needs to be suppressed. Restricting to the 2D case, this means setting one half-plane of the frequency domain to zero. This half-plane is chosen relative to a fixed vector, $\vec{\omega}_k$. Hence the analytic signal of a signal $f : \mathbb{R}^n \to \mathbb{R}$ in the frequency domain is

$$\hat{f}_{AS}(\vec{\omega}) = \begin{cases} 2\hat{f}(\vec{\omega}) & \text{if } \langle \vec{\omega}, \vec{\omega}_k \rangle > 0 \\ \hat{f}(\vec{\omega}) & \text{if } \langle \vec{\omega}, \vec{\omega}_k \rangle = 0 \\ 0 & \text{if } \langle \vec{\omega}, \vec{\omega}_k \rangle < 0 \end{cases} \tag{8.1.9}$$

where $\langle \cdot, \cdot \rangle$ denotes the scalar product in $\mathbb{R}^n$ and the n-D Fourier transform is defined as

$$\mathcal{F}\{f(\cdot)\}(\vec{\omega}) := \hat{f}(\vec{\omega}) = \frac{1}{(2\pi)^{n/2}} \int_{\mathbb{R}}^{n} f(\vec{x}) e^{-i\langle \vec{\omega}, \vec{x} \rangle}\ d\vec{x}$$

Finally the generalised analytic signal of a signal f in the real domain is given by

$$f_{AS}(\vec{x}) = f(\vec{x}) * \left(1 + \frac{i}{\pi \langle \vec{x}, \vec{\omega}_k \rangle}\right) \delta\left(\langle \vec{x}, \vec{\omega}_k \rangle\right) \tag{8.1.10}$$

where $\delta(\cdot)$ is the Dirac distribution.

Another important concept for the formulation of the VMD method is the principle of frequency mixing. By mixing we mean the process of combining two signals in a nonlinear way and introducing cross-frequency terms in the output. The simplest mixing process is the multiplicative one: by multiplying two real signals with frequencies f_1 and f_2 respectively, we create an output with mixed frequencies $f_1 - f_2$ and $f_1 + f_2$.
Therefore, the result of mixing two analytic signals,

$$e^{i2\pi f_1 t} e^{i2\pi f_2 t} = e^{i2\pi (f_1 + f_2) t} \tag{8.1.11}$$

is a mono-tone signal, constituted of only a single frequency. In the Fourier space this corresponds to the following transform pair

$$f_{AS}(t) e^{-i\omega_0 t} \longleftrightarrow_{\mathcal{F}} \hat{f}_{AS}(\omega) * \delta(\omega + \omega_0) = \hat{f}_{AS}(\omega + \omega_0) \tag{8.1.12}$$

i.e. multiplying an analytic signal with a pure exponential results in simple frequency shifting.

8.2 The variational mode decomposition

The VMD is a fully intrinsic and adaptive variational method whose minimisation leads to a decomposition of a signal into its principal modes. It determines the relevant bands adaptively and estimates the corresponding modes concurrently [40]. Using the narrow-band properties of the IMF (definition 8.1.1), the whole modes searched are capable of reconstructing the given signal optimally (exactly or at least in a square-sense) maintaining, although, the condition of being band-limited about a certain frequency estimated on-line.
For guaranteeing a certain optimality in dealing with noise the Wiener filter is used in the model.

In order to asses the bandwidth of a mode the following scheme is proposed:

1. an unilateral frequency spectrum for each mode u_k is obtained computing the associated analytic signal by means of the Hilbert transform;

2. for each mode, the mode's frequency spectrum is shifted to "baseband", by mixing with an exponential tuned to the respective estimated center frequency;

3. the bandwidth estimation is obtained through the H^1 Gaussian smoothness of the demodulated signal, *i.e.* the squared L^2-norm of the gradient.

The resulting constrained variational problem is

$$\min_{u_k,\omega_k} \left\{ \sum_k \left\| \partial_t \left[\left(\delta(t) + \frac{i}{\pi t} \right) * u_k(t) e^{-i\omega_k t} \right] \right\|_2^2 \right\} \quad s.t.\ \forall t \in \mathbb{R},\ \sum_k u_k(t) = f(t) \tag{8.2.13}$$

where δ is Dirac distribution, $i^2 = -1$, $*$ denotes the convolution, $e^{-i\omega_k t}$ is the demodulation to baseband and $||\cdot||_2$ represents the norm in L^2.

8.3 n-D VMD minimising problem

The 2D VMD model has been designed in a similarly manner as the 1D case, minimising the constituent sub-signals' bandwidth while maintaining the original data fidelity.
Thus using the previous definitions the constrained variational problem in n-D can be formulated as followed

$$\min_{u_k:\mathbb{R}^n\to\mathbb{R},\ \vec{\omega}_k\in\mathbb{R}^n} \left\{ \sum_k \left\| \nabla \left[u_{AS,k}(\vec{x}) e^{-i\langle \vec{x},\vec{\omega}_k \rangle} \right] \right\|_2^2 \right\} \quad s.t.\ \forall\ \vec{x} \in \mathbb{R}^n,\ \sum_k u_k(\vec{x}) = f(\vec{x}) \tag{8.3.14}$$

with $u_{AS,k}$ the generalised analytic signal, obtained from the mode u_k using its associated center frequency $\vec{\omega}_k$ (8.1.10). The idea behind the minimisation problem (8.3.14) is to minimise the Dirichlet energy of the modes after performing an half-space spectrum suppression, $u_k \to u_{AS,k}$, and a baseband demodulation, $e^{-i\langle \vec{x},\vec{\omega}_k \rangle}$, under the constrain of collective signal fidelity.

For $n = 2$ the reconstruction constraint is reached through the introduction of both a quadratic penalty method and a generalised Lagrangian multiplier method (the augmented Lagrangian (AL) method). The optimisation is addressed, instead, to an alternate direction minimisation method (ADMM) [5, 40, 109, 153].

8.4 Augmented Lagrangian and ADMM Optimisation

The passage from the constrained minimisation problem (8.3.14) to an unconstrained one, where the fidelity constraint is enforced, is obtained using

both a quadratic penalty argument and a Lagrangian multiplier technique. Considering the Lagrangian multiplier $\lambda : \mathbb{R}^n \to \mathbb{R}$, the augmented Lagrangian associated to problem (8.3.14) is defined as

$$\begin{aligned}\mathcal{L}\left(\{u_k\},\{\vec{\omega}_k\},\lambda\right) = &\sum_k \alpha_k \left|\left|\nabla\left[u_{AS,k}(\vec{x})e^{-i\langle\vec{x},\vec{\omega}_k\rangle}\right]\right|\right|_2^2 + \left|\left|f(\vec{x}) - \sum u_k(\vec{x})\right|\right|_2^2 \\ &+ \left\langle\lambda(\vec{x}), f(\vec{x}) - \sum u_k(\vec{x})\right\rangle\end{aligned} \tag{8.4.15}$$

Hence solving problem (8.3.14) is equivalent to solving the unconstrained saddle point problem

$$\min_{u_k:\mathbb{R}^n\to\mathbb{R},\ \vec{\omega}_k\in\mathbb{R}^n} \max_{\lambda:\mathbb{R}^n\to\mathbb{R}} \mathcal{L}\left(\{u_k\},\{\vec{\omega}_k\},\lambda\right) \tag{8.4.16}$$

In order to find the saddle point of the augmented Lagrangian $\mathcal{L}$ a sequence of iterative sub-optimisations, called alternate direction method of multipliers (ADMM), is performed [5, 70, 126]. The main idea is to iteratively update the following sequence

$$u_k^{t+1} \leftarrow \arg\min_{u_k:\mathbb{R}^n\to\mathbb{R}} \mathcal{L}\left(\{u_{i<k}^{t+1}\}, u_k, \{u_{i>k}^{t}\}, \{\vec{\omega}_i^t\}, \lambda^t\right) \tag{8.4.17}$$

$$\vec{\omega}_k^{t+1} \leftarrow \arg\min_{\vec{\omega}_k\in\mathbb{R}^n} \mathcal{L}\left(\{u_i^{t+1}\}, \{\vec{\omega}_{i<k}^{t+1}\}, \vec{\omega}_k, \{\vec{\omega}_{i>k}^{t}\}, \lambda^t\right) \tag{8.4.18}$$

$$\lambda^{t+1} \leftarrow \lambda^t + \tau\left(f - \sum u_k^{t+1}\right), \quad \text{for } 1 > \tau \geq 0 \tag{8.4.19}$$

Including the Lagrangian multiplier term λ in the quadratic penalty term, (8.4.15) can be rewritten in the following way

$$\begin{aligned}\mathcal{L}\left(\{u_k\},\{\vec{\omega}_k\},\lambda\right) = &\sum_k \alpha_k \left|\left|\nabla\left[u_{AS,k}(\vec{x})e^{-i\langle\vec{x},\vec{\omega}_k\rangle}\right]\right|\right|_2^2 \\ &+ \left|\left|f(\vec{x}) - \sum u_k(\vec{x}) + \frac{\lambda(\vec{x})}{2}\right|\right|_2^2 - \left|\left|\frac{\lambda(\vec{x})^2}{4}\right|\right|_2^2\end{aligned} \tag{8.4.20}$$

The consequent update problem derived from (8.4.20) is

$$\begin{aligned}u_k^{n+1} = \arg\min_{u_k:\mathbb{R}^n\to\mathbb{R}} \Bigg\{ &\alpha_k \left|\left|\nabla\left[u_{AS,k}(\vec{x})e^{-i\langle\vec{x},\vec{\omega}_k\rangle}\right]\right|\right|_2^2 \\ &+ \left|\left|f(\vec{x}) - \sum_i u_i(\vec{x}) + \frac{\lambda(\vec{x})}{2}\right|\right|_2^2 \Bigg\}\end{aligned} \tag{8.4.21}$$

Using the L^2-Fourier isometry and the property of the Fourier transform of frequency shifting when applied to the product of an analytic signal with a pure exponential, (8.4.21) can be written in the spectral space as

$$\begin{aligned}\hat{u}_k^{n+1} = \arg\min_{\hat{u}_k|u_k:\mathbb{R}^n\to\mathbb{R}} \Bigg\{ &\alpha_k \left|\left|j(\vec{\omega}-\vec{\omega}_k)[\hat{u}_{AS,k}(\vec{\omega})\right]\right|\right|_2^2 \\ &+ \left|\left|\hat{f}(\vec{\omega}) - \sum_i \hat{u}_i(\vec{\omega}) + \frac{\hat{\lambda}(\vec{\omega})}{2}\right|\right|_2^2 \Bigg\}\end{aligned} \tag{8.4.22}$$

Using in the latter subminimisation problem the definition of the analytic signal in the spectral domain, $\hat{u}_{AS,k}(\vec{\omega}) = (1 + sign(\langle \vec{\omega}, \vec{\omega}_k \rangle))\hat{u}_k(\vec{\omega})$, and restricting the frequency domain to the half-space $\Omega_k \subset \mathbb{R}^n : \Omega_k = \{\vec{\omega} | \langle \vec{\omega}, \vec{\omega}_k \rangle \geq 0\}$ we have

$$\hat{u}_k^{n+1} = \underset{\hat{u}_k | u_k : \mathbb{R}^n \to \mathbb{R}}{\arg\min} \left\{ 2\alpha_k \int_{\Omega_k} |\vec{\omega} - \vec{\omega}_k| |\hat{u}_k(\vec{\omega})|^2 d\vec{\omega} + \int_{\Omega_k} \left| \hat{f}(\vec{\omega}) - \sum_i \hat{u}_i(\vec{\omega}) + \frac{\hat{\lambda}(\vec{\omega})}{2} \right|^2 d\vec{\omega} \right\} \tag{8.4.23}$$

Sub-minimisation problem (8.4.23) is now solved by letting the first variation w.r.t $\hat{u}_k$ vanishes. Solving the optimality condition for $\hat{u}_k$

$$2\alpha_k |\vec{\omega} - \vec{\omega}_k| \hat{u}_k - \left(\hat{f}(\vec{\omega}) - \sum_i \hat{u}_i(\vec{\omega}) + \frac{\hat{\lambda}(\vec{\omega})}{2} \right) = 0, \quad \forall \vec{\omega} \in \Omega_k \tag{8.4.24}$$

we obtain the following Weiner-filter update for $\hat{u}_k$

$$\hat{u}_k^{n+1}(\vec{\omega}) = \left(\hat{f}(\vec{\omega}) - \sum_{i \neq k} \hat{u}_i(\vec{\omega}) + \frac{\hat{\lambda}(\vec{\omega})}{2} \right) \frac{1}{1 + 2\alpha_k |\vec{\omega} - \vec{\omega}_k|}, \quad \forall \vec{\omega} \in \Omega_k \tag{8.4.25}$$

The term in parentheses is the signal's k-th residual, that includes the explicit current residual, $\hat{f}(\vec{\omega}) - \sum_{i \neq k} \hat{u}_i(\vec{\omega})$, and the remaining term records the reconstruction error during the iterations. The second term represents a frequency filter depending on the current estimate of the mode's center pulsation, $\vec{\omega}_k$ whose bandwidth is controlled by the parameter α_k.

Starting from (8.4.20) the problem of the optimisation for $\vec{\omega}_k$ is

$$\vec{\omega}_k^{n+1} = \underset{\vec{\omega}_k \in \mathbb{R}^n}{\arg\min} \left\{ \alpha_k \left\| \nabla \left[u_{AS,k}(\vec{x}) e^{-i\langle \vec{x}, \vec{\omega}_k \rangle} \right] \right\|_2^2 \right\} \tag{8.4.26}$$

Proceeding as before the problem can be formulated in the spectral domain as

$$\vec{\omega}_k^{n+1} = \underset{\vec{\omega}_k \in \mathbb{R}^n}{\arg\min} \left\{ 4\alpha_k \int_{\Omega_k} |\vec{\omega} - \vec{\omega}_k|^2 |\hat{u}_k(\vec{\omega})|^2 d\vec{\omega} \right\} \tag{8.4.27}$$

Letting the first variation w.r.t. $\vec{\omega}_k$ vanishes

$$\int_{\Omega_k} \left(\vec{\omega} - \vec{\omega}_k^{n+1} \right) |\hat{u}_k(\vec{\omega})|^2 d\vec{\omega} = 0$$

the solution is

$$\vec{\omega}_k^{n+1} = \frac{\int_{\Omega_k} \vec{\omega} |\hat{u}_k(\vec{\omega})|^2 d\vec{\omega}}{\int_{\Omega_k} |\hat{u}_k(\vec{\omega})|^2 d\vec{\omega}} = \frac{\int_{\mathbb{R}^n} \vec{\omega} |\hat{u}_{AS,k}(\vec{\omega})|^2 d\vec{\omega}}{\int_{\mathbb{R}^n} |\hat{u}_{AS,k}(\vec{\omega})|^2 d\vec{\omega}} \tag{8.4.28}$$

The obtained solution is the center of gravity of the modes' power spectra $|\hat{u}_k(\vec{\omega})|^2$ restricted to the half-space Ω_k in the first case and extended to all the frequency domain in the second one.

Let us now consider the maximizing w.r.t. the Lagrangian multiplier. The first variation for λ is the data reconstruction error, $\hat{f}(\vec{\omega}) - \sum_k \hat{u}_k^{n+1}(\vec{\omega})$, therefore, using a standard gradient ascent with fixed time step $1 > \tau \geq 0$ the maximisation is achieved when

$$\lambda^{n+1}(\vec{x}) = \lambda^n(\vec{x}) + \tau \left(f(\vec{x}) - \sum_k u_k^{n+1}(\vec{x}) \right) \tag{8.4.29}$$

Since the Lagrangian multiplier in (8.4.23) is represented in the spectral domain, the previous dual ascent update is performed in the frequency domain

$$\hat{\lambda}^{n+1}(\vec{\omega}) = \hat{\lambda}^n(\vec{\omega}) + \tau \left(\hat{f}(\vec{\omega}) - \sum_k \hat{u}_k^{n+1}(\vec{\omega}) \right) \tag{8.4.30}$$

8.5 The 2D-VMD algorithm

The algorithm for the 2D-VMD functional optimisation problem (8.3.14) is summarised in algorithm 1.

Algorithm 1 2D-VMD

Input: image $f(\vec{x})$, number of modes K, parameters α_k, τ, ϵ
Output: extracted modes $u_k(\vec{x})$, center frequencies $\vec{\omega}_k$

Initialize $\{\omega_k^0\}$, $\{\hat{u}_k^0\} \leftarrow 0$, $\hat{\lambda}^0 \leftarrow 0$, $n \leftarrow 0$
repeat
  $n \leftarrow n + 1$
  for $k = 1 : K$ **do**
    $\mathcal{H}_k^{n+1}(\vec{\omega}) \leftarrow 1 + sign(< \vec{\omega}_k^n, \vec{\omega} >)$
    $\hat{u}_{AS,k}^{n+1}(\vec{\omega}) \leftarrow \mathcal{H}_k^{n+1}(\vec{\omega}) \left(\frac{\hat{f}(\vec{\omega}) - \sum_{i<k} \hat{u}_i^{n+1}(\vec{\omega}) - \sum_{i>k} \hat{u}_i^n(\vec{\omega}) + \frac{\hat{\lambda}^n(\vec{\omega})}{2}}{1 + 2\alpha_k |\vec{\omega} - \vec{\omega}_k^n|} \right)$
    $\vec{\omega}_k^{n+1} = \frac{\int_{\mathbb{R}^n} \vec{\omega} |\hat{u}_{AS,k}^{n+1}(\vec{\omega})|^2 d\vec{\omega}}{\int_{\mathbb{R}^n} |\hat{u}_{AS,k}^{n+1}(\vec{\omega})|^2 d\vec{\omega}}$
    $u_k^{n+1}(\vec{x}) \leftarrow \mathcal{R} \left(F^{-1} \left\{ \hat{u}_{AS,k}^{n+1}(\omega) \right\} \right)$
    $\hat{\lambda}^{n+1}(\vec{\omega}) = \hat{\lambda}^n(\vec{\omega}) + \tau \left(\hat{f}(\vec{\omega}) - \sum_k \hat{u}_k^{n+1}(\vec{\omega}) \right)$
  end for
until $\sum_k ||\hat{u}_k^{n+1} - \hat{u}_k^n||_2^2 / ||\hat{u}_k^n||_2^2 < \epsilon$

An important degree of freedom in this algorithm is represented by the initialisation of the variables. In fact, while the matrix of the extracted modes $u_k(\vec{x})$ has a natural initialisation to zero, the initialisation of the

center frequencies is more sensitive. Initial $\vec{\omega}_k^0$ can be, e.g., spread randomly, radially uniform, or initialised by user input.
The choice of a proper value for the parameter α permits to have a good performance of the Weiner filter. Qualitatively, a high α leads to a finer separation of constituent sub-signals, because the Wiener filter is more narrowly concentrated around its center frequency. However, if the filter is centred away from a non-principle frequency, it may fail to catch the significant principle frequencies. On the contrary, choosing a low α generates a wider filter, allowing the algorithm to detect and reach the correct frequencies, but on the other end yielding worse separation. Therefore, if the values to which initialise the correct frequencies are known, it is better to use a high α (more accurate results will be produced). Instead, if no *a priori* information on the frequencies initialisation is known, a low α will give more freedom of mobility to the ω_k at the expense of a proper modes separation.
The convergence is assessed using the normalised rate of change of the modes (line 11 in algorithm 1). Typically the thresholds $\epsilon > 0$ is chosen in a range of magnitude from 10^{-4} (fast) down to 10^{-7} (very accurate).

Chapter 9

Data analysis

The VKP experimental set-up (Chapter 7) can be used for studying and understanding how the interaction of drift waves in the plasma column can pass from a phase of weak mode interaction to a regime in which weak turbulence is generated (Chapter 6).

It has been seen that the insertion of a hot emissive cathode negatively biased in the center of the cylindrical vessel (Chapter 7) can cause a strong modification of both the plasma potential and the plasma density, allowing the formation of strong gradients that may drive large amplitude drift waves which, in turn, may interact in a nonlinar way. Strong gradients can also appear in the presence of large applied magnetic field. In fact, it has been observed that, increasing the applied magnetic field, modes based on drift waves are generated (Figure 9.1). In order to study the plasma density fluctuations, a non-intrusive plasma diagnostic using the fast camera described in section 7.2.2 has been preferred.

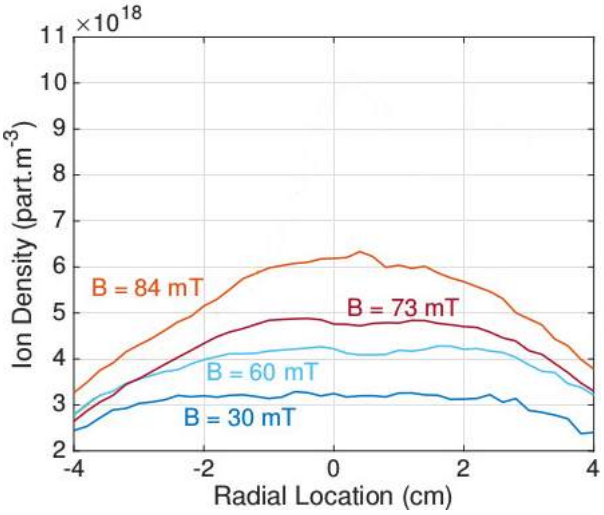

Figure 9.1: Plot of the ion density as a function of the radial position in the cylinder for different magnetic fields [41].

It is interesting to analyse the emitted plasma light because it is related to the plasma density. In particular, when a photon has an amount of energy sufficient for a change in the energy state of the system (ex. an electron changing orbital) it is absorbed. Nevertheless, it is later spontaneously re-emitted.
The plasma column under study is not in a thermodynamic equilibrium and the atomic state transition is not caused by photo-excitation but it is guided by the interaction between the electrons present in the plasma and the other plasma particles (ions and neutrals).
In particular, it can be shown that in a simplified radiative phenomena model of the plasma column, it exists a one-to-one relationship between both the plasma density and the light intensity fluctuations [113]. In fact, let's suppose that the excitation of the atoms from the state s to the state k is done by electron collisions followed by a transition from the state k to a lower state l and accompanied by the emission of a photon. Then the density n_k of excited atoms is proportional to the atom density at the state s, the electron density n_e and the interaction probability $\langle \sigma \nu_e \rangle$, where σ is the effective electron-neutral collision section and ν_e is the collision frequency, *i.e.*

$$n_k \simeq n_s n_e \langle \sigma n_e \rangle_{s \to k} \tag{9.0.1}$$

In the simplest case we can consider the fundamental state $s = 0$ of the neutrals as the only state s. Thus it is reasonable to suppose that the emitted light in the plasma column is proportional to

$$I \simeq n_0 n_e \langle \sigma \nu_e \rangle_{0 \to k} \tag{9.0.2}$$

Therefore, in this simplified description, the absorption of photons by the plasma can be neglected so that the light intensity captured by the camera corresponds to the light intensity produced by the emission which follows the extraction by electron collisions of the atom.
Looking at (9.0.2), we can see that the light fluctuations recorded by the camera can originate from fluctuations in neutral density, electron density and electron temperature (this because the electron temperature influences the interaction probability). In the plasma column under study, the distribution of neutral is uniform and temperature fluctuations are often considered negligible. Thus we can suppose that the modulation of the light intensity depends solely on electronic density fluctuations.

In order to isolate the electron transitions responsible of the intensity light fluctuations, two interference filters centred on the wavelenghts 488 and 750 nm have been placed in front of the camera. These wavelengths correspond to the main emission lines spectroscopy in the argon plasma column. The lines at 750 nm correspond to electronic transitions of neutral argon whereas the line at 488 nm corresponds to a transition of the argon ion Ar^+.
It has been seen that the ion line at 488 nm does not give a strong contribution to the fluctuations observed in the absence of filters. On the other

hand, intensity distributions, obtained using filters at 750 nm, correspond to brightness fluctuations around a value of average intensity.

In this chapter we present some preliminary results obtained through the application of the two-dimensional VMD analysis (Chapter 8) to the images recoded by the fast camera in the case of a complete scan of the plasma column with magnetic field varying in the range [30 mT − 89 mT], plasma density of 0.9 mTor, and power given to the RF source of 1 kW. Our goal is to extract the modes characterising the plasma dynamics, and to analyse how they are modified when the imposed magnetic field is increased.

9.1 Application of the two-dimensional VMD analysis

The fast camera provides a two-dimensional representation of brightness fluctuations on a complete section of the plasma column. However, these spatio-temporal variations are hardly visible on the raw films because of both the lack of plasma brightness and the low exposure time (typically $10\,\mu s$). Therefore, it is necessary to perform a filtering process on the raw images before carrying out any type of data exploitation. The treatment generally applied consists of subtracting the image average calculated on the entire film to each image of the same film (each film corresponds to one snap-shot of the plasma). This procedure permits the elimination of the constant light emission of discharge filaments and reflections due to the inner walls of the machine, resulting in the fluctuations of interest.
In addition, in order to remove the image noise, a Gaussian smoothing[1] filtering has been implemented on each image of the video. An example of this filtering method is presented in Figure 9.2. After subtracting the average image, the azimuthal structure of light fluctuations $n = 2$ is displayed in a clearer way.

The instabilities in the VKP column plasma mainly propagate in the azimuthal direction. Thus the study of dynamics in the azimuthal plane allows to analyse the azimuthal modes that take places in the plasma.
Usually in linear machines probes placed in a circular configuration are used to achieve the previous purpose [128, 149, 10]. These probes, regularly distributed in such configuration, can simultaneously measure temporal fluctuations of ion saturation current or floating potential providing direct access to wave numbers and phase velocities.

It is possible to simulate this circular configuration of probes in the images acquired with the high speed camera. In this case we refer to a virtual corona. Before extracting the time series corresponding to a virtual

[1] In image processing a Gaussian smoothing, or Gaussian blur, corresponds to the blurring of an image by a Gaussian function. Technically it consists in performing a convolution of the image with a Gaussian function. Therefore, the Gaussian blur is no more than a low pass filter.

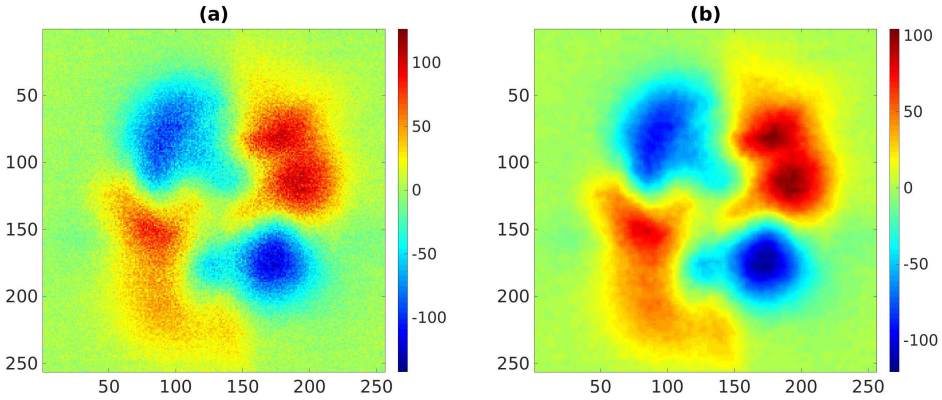

Figure 9.2: (a) Raw image. (b) Image treated with the filtering method.

probe corona, the center of the plasma column must be determined. We notice that this center doesn't necessarily correspond to the center of the image or the center of the machine. A first method for locating it is to average the fluctuations module of luminosity over all the images. This permits a better localisation of the modes and estimation of the image coordinates $[x_c, y_c]$ corresponding to the center of the plasma column.
Once that the coordinates $[x_c, y_c]$ are determined, the time series of the light fluctuations are extracted on N pixels corresponding to N virtual probes (Figure 9.3), distributed on the circle of center $[x_c, y_c]$ and radius r_0 pixels. The position on the image of the i-th virtual probe (with $i = 1, .., N$) corresponds to the coordinates $[x_i, y_i]$ defined by

$$\begin{aligned} x_i &= x_c + r_0 \cos\left(\frac{2\pi i}{N}\right) \\ y_i &= y_c + r_0 \sin\left(\frac{2\pi i}{N}\right) \end{aligned} \tag{9.1.3}$$

The virtual corona data, extracted from each image, permits the reconstruction of the spatio-temporal fluctuations diagram at a given radius r_0.

An example is shown in Figure 9.4. The spatio-temporal diagram has been extracted from the same film from which the images presented in Figure 9.2 has been selected. 200 virtual probes have been extracted from 2000 images with a fixed radius of 3 cm and a plasma column center of $[132, 128]$. Minima and maxima luminous fluctuations form regular transverse bands indicating the presence of coherent modes. For a given time, the number of maxima or minima between $\vartheta = 0$ and $\vartheta = 2\pi$ determines the spatial number n of present modes. Here mode $n = 2, 3$ are observed.
The slope of the transverse bands indicates the azimuthal velocity of instability. It can be significantly modified if the virtual corona is not well centred.

The extraction of virtual corona from fast camera films presents a certain number of advantages over mechanical probe corona. It is a non-

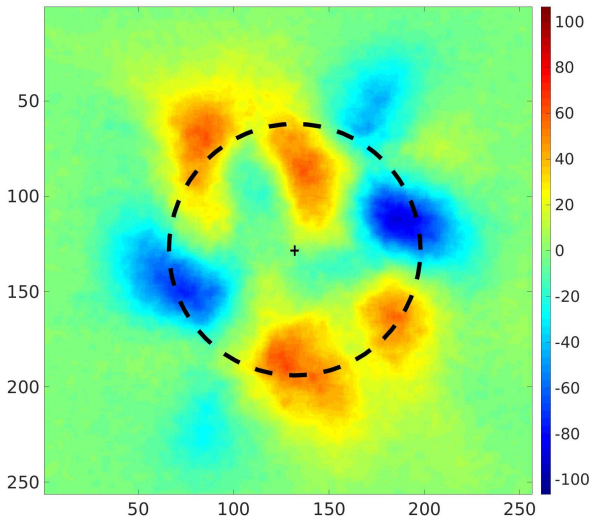

Figure 9.3: 200 virtual probes located on the circle (9.1.3) with $r_0 = 3$ cm and $[x_0, y_0] = [132, 128]$.

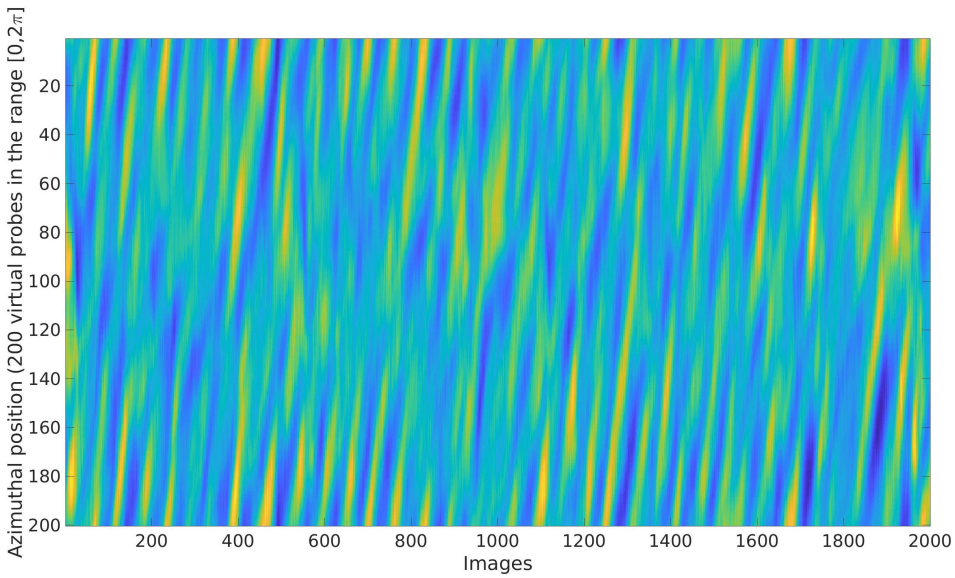

Figure 9.4: Spatio-temporal diagram of the light intensity fluctuations.

intrusive and therefore a non-perturbative diagnostic method. It permits a simple correction of centring errors and the diameter of the virtual column can be determined freely, allowing a simultaneous study of the spatio-temporal dynamics at different rays. However, it is important to point out that the use of virtual probes can be, unlike real probes, limited by the sampling frequency limit inherent in the type of camera used.

Our idea is to apply the two-dimensional VMD to the spatio-temporal diagrams extracted from the recorded film of the plasma column. As

pointed out in Chapter 8, the 2D-VMD algorithm is a non-recursive, fully adaptive (a non a-priori basis is imposed), variational method which sparsely decomposes images with minimal parameters and no explicit interpolation in a robust mathematical manner. Therefore, it represents a good tool for the mode extraction.

For the implementation of the 2D-VMD algorithm, the MATLAB® code written by Dominique Zosso[2] has been used. Although, a modification of the stopping criteria has been introduced[3]: two different tolerances (ϵ_u, ϵ_ω) for the extracted mode u_k and the center frequency ω_k are now used, such that

$$\sum_k \frac{||\hat{u}_k^{n+1} - \hat{u}_k^n||_2^2}{||\hat{u}_k^n||_2^2} < \epsilon_u \tag{9.1.4}$$

$$\sum_k \frac{||\hat{\omega}_k^{n+1} - \hat{\omega}_k^n||_2^2}{||\hat{\omega}_k^n||_2^2} < \epsilon_\omega \tag{9.1.5}$$

where $\hat{}$ identifies quantities in the Fourier space.

In fact, our input images are characterised by a strong mixture of different mode during the time evolution. Therefore, using the same threshold value for both the extracted modes and the center frequencies does not permit sufficiently good mode separation and detection of the correct frequencies. An example of 2D-VMD extraction analysis is given in Figure 9.6, where the film at magnetic field B of 39 mT has been chosen. The extraction has been performed three times in order to clearly extract non-overlapping modes (obviously the fidelity of the input data has been maintained). The input parameters used in the code are reported in Table 9.1. The method has permitted not only the extraction of the characteristic modes without using a fixed basis for the extraction algorithm, but also detects their rotation direction (clockwise or counter-clockwise).

Parameters	Values
α	13000
τ	0.25
$\mathrm{tol_u}$	$9\,10^{-5}$
tol_ω	$5\,10^{-5}$
n	300
ω_k^0	uniformly spread on a circle

Table 9.1: Input parameters for the 2D-VMD code extraction for film with imposed $B = 39$ mT.

[2] https://it.mathworks.com/matlabcentral/fileexchange/45918-two-dimensional-variational-mode-decomposition

[3] For a detailed definition of the interested quantities see Chapter 8.

In Figure 9.5 the plot of the two convergences for the mode extracted and the center frequency detected in function of the number of iterative steps operated by the code is reported. We observe that the code stops before reaching the imposed maximum number of iterations $n = 300$ with tolerance values for the mode extracted and the center frequency of $8.9\,10^{-5}$ and $8.3\,10^{-6}$ respectively.

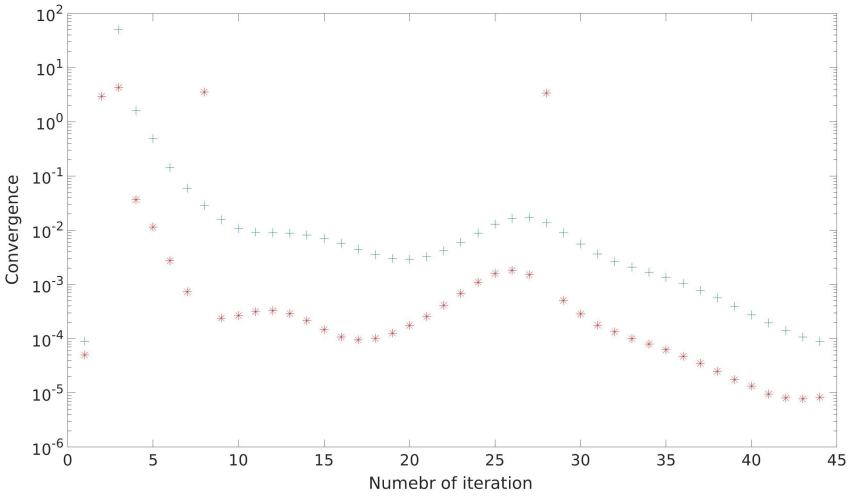

Figure 9.5: Semi-log plot of the convergence values in function of the iteration steps. $+$ extracted mode; $*$ center frequency.

We point out that for each film analysed several preliminary tests on the best choice parameters configurations has been performed in order to determine the best set of input parameters. It is very important to choose the appropriate value for the α-parameter because it influences the confidence of the algorithm (Chapter 8).

It is worth asking if the behaviour of the modes characterising the plasma column dynamics can be somehow related to the dynamics described by the Hasegawa-Mima equation (6.2.24). In section 6.2, under the assumptions that the fluctuations only propagates in the $\hat{y}$-direction and $k_y L_n \gg 1$, we have tried to rewrite the Hasegawa-Mima dispersion relation (6.2.25) (which is formulated in a Cartesian geometry) in a cylindrical geometry. We point out that equation (6.2.25) is valid in the high n-mode case, therefore it cannot be used in our analysis where we are taking into account just low modes $1 \leq n \leq 4$.
Thus only order of magnitude estimates can be performed. In particular, assuming frequencies of the order of

$$\frac{u_d}{2\pi r} = \frac{k_B T_e c}{eB}\frac{1}{L_n}\frac{1}{2\pi r} = \tilde{\omega}\Big|_{B=30\text{ mT}} = 4 \cdot 10^3\text{ Hz} \tag{9.1.6}$$

the density gradient scale length L_n, such that $L_n^{-1} = -\partial_x \ln(n_0)$, can be calculated in the cgs system of units. In fact, we have $L_n \simeq 22$ cm.

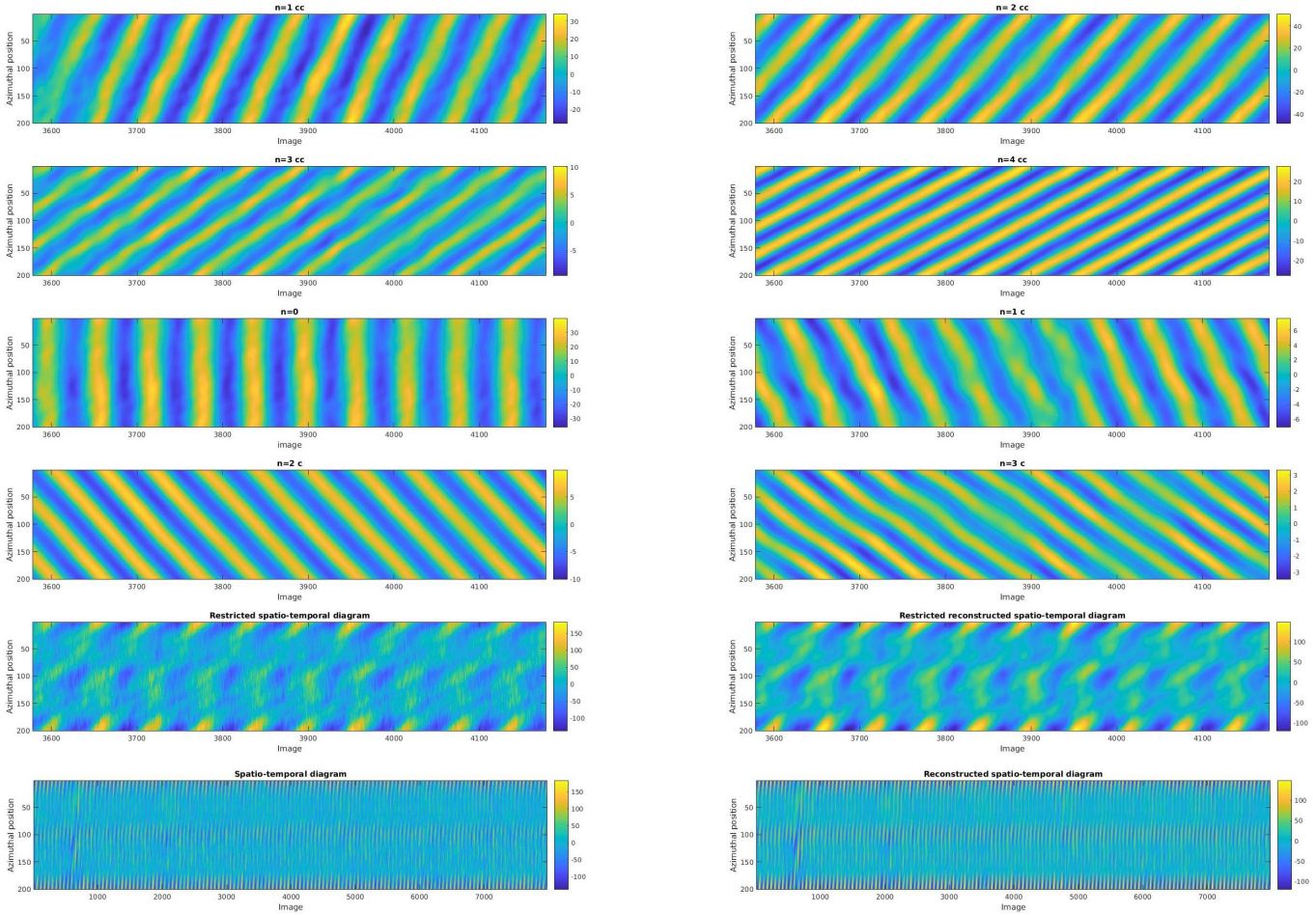

Figure 9.6: 2D-VMD mode extraction for a spatio-temporal diagram corresponding to a virtual corona of radius $r_0 = 3$ cm and column center $[132, 128]$ and magnetic field $B = 39$ mT. The symbols c. and c.c. identify clockwise and counter-clockwise modes respectively.

Considering that the diameter of the cylindrical vessel is of 20 cm, the density gradient scale length just obtained is comparable to the characteristic length scale of the experiment. This result is compatible with the density trend as a function of the radial position in the cylinder for increasing magnetic field presented in Figure 9.1, where at low values of B the density profile is almost flat, while, increasing B, strong gradient start to appear in the center.

The 2D-VMD analysis performed for a virtual corona with a fixed radius can be repeated for different radius values in order to cover all the plasma column. In this way, starting from spatio-temporal diagrams at different radii, a complete mode extraction of the entire plasma column during all the shots is obtained. It is interesting to observe that only a few number of modes are needed in order to recover the entire image (they carry the majority of the energy). Moreover, we point out that this extractive method is able to catch the time evolution of the modes' shape. This because the basis functions involved during the extraction are adaptively chosen according to the corresponding input. An example of this column mode extraction for a fixed image of a chosen film is showed in Figure 9.7. The film analysed corresponds to a magnetic field of 84 mT.

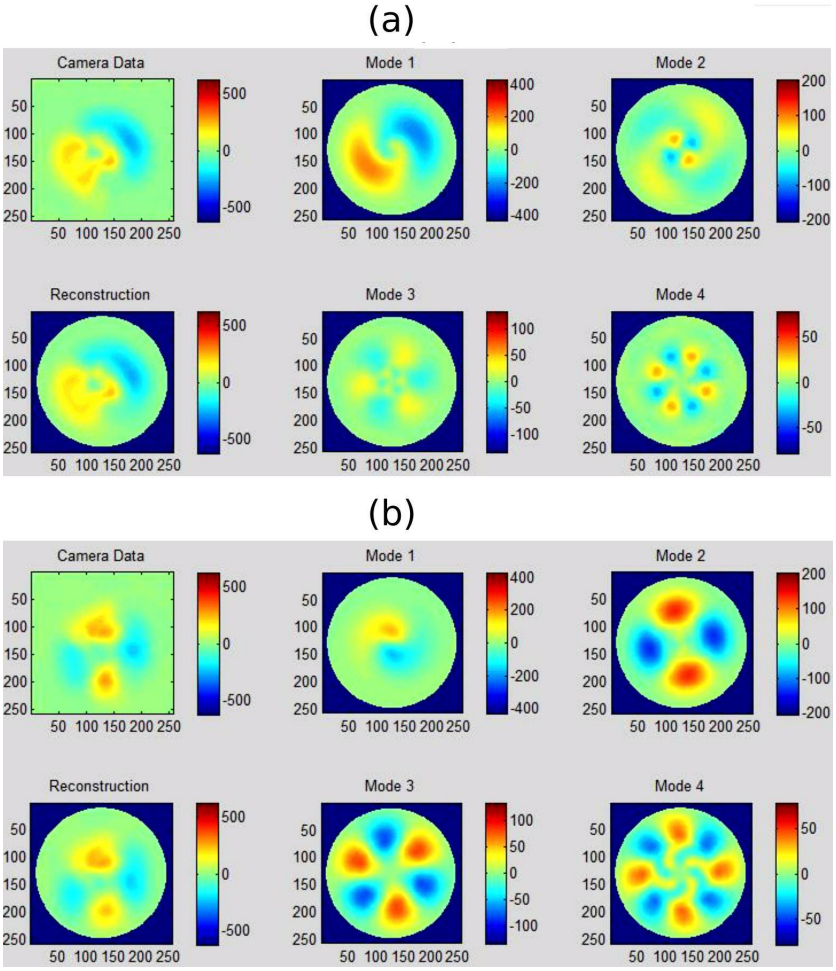

Figure 9.7: Snapshots of the reconstructed film for a magnetic field of 84 mT.

Part III

Regularity and weak solutions in nonlinear elliptic equations

Introduction

Among the most important partial differential equations there are Laplace's equation

$$\Delta u = 0 \tag{9.1.7}$$

and Poisson's equation

$$-\Delta u = f \tag{9.1.8}$$

where in both cases $\boldsymbol{x} = (x_1, ..., x_n) \in U$, with $U \subseteq \mathbb{R}^n$ a given open set, $u : \bar{U} \to \mathbb{R}$ with $u = u(\boldsymbol{x})$, $f : U \to \mathbb{R}$ is a given function and the Laplacian orator is defined such as

$$\Delta u = \sum_{i=1}^{n} u_{x_i x_i}{}^{4} \tag{9.1.9}$$

If a function $u \in C^2(U)$ satisfies 9.1.7 it is called harmonic function [42].

These two equations are particularly important for their application to different physical contexts (for example Laplace's equation arises in cases such as steadystate heat flow, irrotational fluid flow, current flow in an extended medium, and in the deflection of an elastic membrane).
A typical physical interpretation in the case of Laplace's equation is to consider the function u as the density of same quantity in equilibrium. Then, if V is a smooth subset of U, we have that the net flux of u through the boundary of V, ∂V, is zero, *i.e.*

$$\int_{\partial V} \boldsymbol{F} \cdot \boldsymbol{\nu} \, dS = 0$$

where $\boldsymbol{F}$ is the flux density and $\boldsymbol{\nu}$ is the outer normal vector to ∂V.

Applying Gauss-Green theorem we have

$$\int_V \operatorname{div}(\boldsymbol{F}) \, d\boldsymbol{x} = \int_{\partial V} \boldsymbol{F} \cdot \boldsymbol{\nu} \, dS = 0$$

But V was arbitrary chosen, hence

$$\operatorname{div}(\boldsymbol{F}) = 0, \quad \text{in } U \tag{9.1.10}$$

[4] Here we use the notation $u_{x_i} = \frac{\partial u}{\partial x_i}$ and $u_{x_i x_i} = \frac{\partial^2 u}{\partial x_i^2}$.

It is physically reasonable to suppose $\boldsymbol{F}$ proportional to the gradient ∇u but with opposite direction, this because the flow is supposed to move from regions of higher to lower concentration. Thus

$$\boldsymbol{F} = -\alpha \nabla u, \;\; \alpha > 0 \tag{9.1.11}$$

Substituting the new expression of $\boldsymbol{F}$ in (9.1.10) we get the Laplace's equation

$$div\,(\nabla u) = \Delta u = 0$$

We recall that if

- u denotes a chemical concentration, then (9.1.11) is the Fick's law of diffusion;
- u denotes a temperature, then (9.1.11) is the Fourier's law of heat conduction;
- u denotes an electrostatic potential, then (9.1.11) is the Ohm's law of electrostatic conduction.

For a better description about the physical applications of Laplace's equation we refer to [48].

Laplace's equation can also be seen as the Euler-Lagrange equation of the Dirichlet integral

$$D(u) = \int_U |\nabla u|^2 d\boldsymbol{x} \tag{9.1.12}$$

A generalisation of Laplace's equation and Poisson's equation is given by second-order elliptic partial differential equations (PDE). In fact let us consider the following boundary-value problem

$$\begin{cases} Lu = f \;\; \text{in } U \\ u = 0 \quad \text{on } \partial U \end{cases} \tag{9.1.13}$$

where U is an open bounded subset of $\mathbb{R}^n$, $u : \bar{U} \to \mathbb{R}$ with $u = u(\boldsymbol{x})$, $f : U \to \mathbb{R}$ is a known function and the requirement that $u = 0$ on ∂U is the so-called Dirichlet's boundary condition.
L denotes a second-order partial differential operator having either the divergence form

$$Lu = -\sum_{i,j=1}^{n} \left(a^{ij}\,(\boldsymbol{x})\,u_{x_i}\right)_{x_j} + \sum_{i=1}^{n} b^i\,(\boldsymbol{x})\,u_{x_i} + c\,(\boldsymbol{x})\,u \tag{9.1.14}$$

or the non-divergence form

$$Lu = -\sum_{i,j=1}^{n} a^{ij}\,(\boldsymbol{x})\,u_{x_i x_j} + \sum_{i=1}^{n} b^i\,(\boldsymbol{x})\,u_{x_i} + c\,(\boldsymbol{x})\,u \tag{9.1.15}$$

for given coefficient functions a^{ij}, b^i and c with $i, j = 1, ..., n$. Generally it is assumed valid the symmetry condition: $a^{ij} = a^{ji}, \;\; \forall i, j = 1, ..., n$.

Remark 9.1.1. *If the coefficient a^{ij} are C^2 functions, then the operator L given in the divergence form can be expressed also in the non-divergence form and vice versa.*

Definition 9.1.2. *A partial differential operator L is uniformly elliptic if there exists a constant $\vartheta > 0$ such that*

$$\sum_{i,j} a^{ij}(\boldsymbol{x})\,\xi_i\xi_j \geq \vartheta|\xi|^2 \tag{9.1.16}$$

for a.e. $\boldsymbol{x} \in U$ and for all vectors $\boldsymbol{\xi} \in \mathbb{R}^n$.

The ellipticity condition (9.1.16) implies that for each point $\boldsymbol{x} \in U$ the symmetric matrix $n \times n$, $\tilde{\boldsymbol{A}}(\boldsymbol{x}) = \left(a^{i,j}(\boldsymbol{x})\right)_{i,j}$, is positive definite, with the smallest eigenvalue greater than or equal to ϑ.

If in L $a^{ij} = \delta_{ij}$, $b^i = 0$ and $c = 0$ for all $i, j = 1, ..., n$, then the operator L is exactly the Laplacian operator and we find either Poisson's equation if $f \neq 0$, or the Laplace's equation if $f = 0$.
In general, the second-order term $\boldsymbol{A} = \sum_{i,j=1}^n a^{ij} u_{xixj}$ represents the diffusion of the density u within U, where the coefficients $\left(a^{ij}\right)_{i,j}$ describe the anisotropic, heterogeneous nature of the medium. Moreover $\boldsymbol{F} = -\boldsymbol{A}\nabla u$ is the diffusive flux density. In this case the ellipticity condition implies $\boldsymbol{F} \cdot \nabla u \leq 0$, *i.e.* the flow goes from regions of higher concentration to lower one. The first-order term $\boldsymbol{b} \cdot \nabla u = \sum_{i,j=1}^n b^i u_{x_i}$ stands, instead, for the transport within U, while the zeroth-term $c\,u$ represents the local creation or depletion of the density u.

Usually the study of the existence and the uniqueness of a weak solution to the boundary-value problem (9.1.13) is carried on using particular techniques, such as the energy methods within Sobolev spaces and the maximum principle methods [42].

An other interesting generalisation of the Laplace's equation arises from the fact that, under the appropriate hypothesis of regularity on u, it is possible to generalise the Dirichlet integral (9.1.12) to the $p^{th}-$integral

$$I_p(u) = \int_U |\nabla u|^p d\boldsymbol{x} \tag{9.1.17}$$

an thus identify the corresponding Euler-Lagrange equation as the p-Laplace equation

$$\operatorname{div}\left(|\nabla u|^{p-2}\nabla u\right) = 0 \tag{9.1.18}$$

In the latter equation the p-Laplacian operator $\Delta_p u = \operatorname{div}\left(|\nabla u|^{p-2}\nabla u\right)$ has been introduced.
Usually $p \geq 1$ and the solutions are called p-harmonic functions. At critical points, *i.e.* $\boldsymbol{x}$ such that $\nabla u = 0$, equation (9.1.18) is degenerate for $p > 2$ and singular for $p < 2$. For a dissertation about the p-Laplacian equation we refer to [29, 129, 130, 16, 102, 104, 105] and the references therein.

Of particular interest is the use of a generalisation of the p-Laplacian operator in order to describe the dynamics of generalised Newtonian fluids.

In fact a good model for generalised Newtonian fluids in a suitable smooth bounded domain Ω of $\mathbb{R}^n$ is given by the following nonlinear boundary-value system

$$\begin{cases} -\nabla \cdot \left[(\mu + |\mathcal{D}\boldsymbol{u}|)^{p-2} \mathcal{D}\boldsymbol{u} \right] + (\boldsymbol{u} \cdot \nabla)\, \boldsymbol{u} + \nabla P = \boldsymbol{f} \\ \nabla \cdot \boldsymbol{u} = 0 \end{cases} \tag{9.1.19}$$

where μ is a non-negative constant, $p > 1$, $\boldsymbol{u}$ is the velocity field, P is the pressure field, $\boldsymbol{f}$ is a known force function and

$$\mathcal{D}\boldsymbol{u} = \frac{1}{2} \left(\nabla \boldsymbol{u} + \nabla \boldsymbol{u}^T \right) \tag{9.1.20}$$

is the symmetric part of the gradient of $\boldsymbol{u}$.
If $p = 2$ system (9.1.19) corresponds to the well-know Navier-Stokes system of equation for Newtonian fluids. While, for $p \in (1, 2)$, (9.1.19) describes the dynamics of non-Newtonian fluids with shear dependent viscosity (shear thinning fluids) [89, 122, 88, 54, 28].

In this section we deal with both the local and global regularity theory for nonlinear degenerate elliptic equations in divergence form. In particular, we consider weak solutions to

$$-\operatorname{div} \left(A\left(|\nabla u| \right) \nabla u \right) + b(x) |\nabla u|^q = f(x) \tag{9.1.21}$$

in an open set $\Omega \subseteq \mathbb{R}^n$, where $A : \mathbb{R}^+ \to \mathbb{R}^+$ is a real valued function of class C^1. We point out that when $A(x) = x^{p-2}$ equation (9.1.21) reduces to a standard p-Laplacian equation.

Chapter 10

Second order regularity for degenerate nonlinear elliptic equations

We investigate the second order regularity of solutions to degenerate nonlinear elliptic equations [15].

10.1 Introduction and results

We deal with the regularity theory for nonlinear degenerate elliptic equations in divergence form. In particular we consider weak solutions to

$$-\mathrm{div}(A(|\nabla u|)\nabla u) + b(x)|\nabla u|^q = f(x) \quad \text{in } \Omega, \tag{10.1.1}$$

in a open set $\Omega \subseteq \mathbb{R}^N$. The real valued function $A : \mathbb{R}^+ \to \mathbb{R}^+$ is of class C^1, with

$$\limsup_{t\to 0^+} tA(t) < \infty \tag{10.1.2}$$

and

$$-1 < \inf_{t>0} \frac{tA'(t)}{A(t)} := m_A \le M_A := \sup_{t>0} \frac{tA'(t)}{A(t)} < \infty\,. \tag{10.1.3}$$

We also assume that

$$A(s) \ge Ks^{\tilde{\vartheta}} \qquad \text{for some } \tilde{\vartheta} \ge 0 \quad \forall\, s > 0\,. \tag{10.1.4}$$

When $b(x)$ is not identically zero, we assume that $q > \frac{\tilde{\vartheta}+1}{2}$.

We shall consider solutions of class $C^{1,\alpha}$. This natural in general according to [36, 87, 85, 139, 142]. Therefore we give the following

Definition 10.1.1. *We say that $u \in C^{1,\alpha}(\Omega)$ is a weak distributional solution to (10.1.1), if*

$$\int_\Omega A(|\nabla u|)(\nabla u, \nabla \phi)\, dx + \int_\Omega b(x)|\nabla u|^q \phi\, dx = \int_\Omega f\, \phi\, dx \tag{10.1.5}$$

for every $\phi \in C_c^\infty(\Omega)$.

We will frequently exploit the fact that the equation is no longer degenerate outside the critical set Z_u,

$$Z_u := \{\nabla u = 0\}.$$

Consequently it is also natural to assume that the solution is of class C^2 outside the critical set.

Remark 10.1.2. *We will use the notation $u_i := u_{x_i}$, $i = 1 \ldots, N$, to indicate the partial derivative of u with respect to x_i. These are the classic derivatives since u is of class C^1. The second derivatives will be indicated with u_{ij}, $i, j = 1 \ldots, N$. In this case, since u is of class C^2 only far from the singular set Z_u, we agree that u_{ij} coincides with the second derivatives far from the singular set Z_u, while $u_{ij} = 0$ on the singular set Z_u. At the beginning this is only a notation inspired by the Stampacchia's theorem but, according to our Theorem 10.1.5 below, with this definition u_{ij} will represent actually the second distributional derivatives.*

Our aim is to study the summability of the second derivatives of the solutions. When $A(t) = t^{p-2}$ the operator reduces to standard p-Laplacian. In this case, from [29, 129, 130] (see also [16, 102]), it follows that $u \in W^{2,2}_{\mathrm{loc}}(\Omega)$ if $1 < p < 3$, and that if $p \geq 3$ and the source term f is strictly positive then $u \in W^{2,q}_{\mathrm{loc}}(\Omega)$ for $q < \frac{p-1}{p-2}$. We may look at this type of regularity as an issue in the context of the Calderón-Zygmund theory for nonlinear degenerate problems. We refer the reader to [104, 105] and the references therein.

Here we shall extend the results in [29, 129, 130]. The setting described above is really more general than the case of the p-laplacian. Then the proofs in [29, 129, 130] and the results as well needs appropriate modifications. We start with the following

Theorem 10.1.3. *Let $u \in C^{1,\alpha}(\Omega) \cap C^2(\Omega \setminus Z_u)$ be a solution to (10.1.1) with $f, b \in W^{1,\infty}(\Omega)$. Assume that $B_{2\rho}(x_0) \subset \Omega$ and $y \in \Omega$. Then, for $0 \leq \beta < 1$ and $\gamma < N - 2$ for $N \geq 3$ while $\gamma = 0$ if $N = 2$, we have*

$$\int_{B_\rho(x_0)} \frac{A(|\nabla u|)|\nabla u_i|^2}{|x-y|^\gamma |u_i|^\beta} \leq \mathsf{C} \qquad \forall i = 1, ..., N \tag{10.1.6}$$

with $\mathsf{C} = \mathsf{C}(\gamma, \beta, q, f, b, ||\nabla u||_\infty, \rho, x_0)$.

The local regularity result of Theorem 10.1.3 holds without sign assumption on the source term f. If else a sign assumption on f is imposed, than we can prove a summability result regarding the inverse of the weight $A(|\nabla u|)$. We have

Theorem 10.1.4. *Let $u \in C^{1,\alpha}(\Omega) \cap C^2(\Omega \setminus Z_u)$ be a solution to (10.1.1) with $f, b \in W^{1,\infty}(\Omega)$ and $f(x) \geq c(\rho, x_0) > 0$, in $B_{2\rho}(x_0) \subset \Omega$ for some $\rho = \rho(x_0) > 0$. Then we have*

$$\int_{B_\rho(x_0)} \frac{1}{(A(|\nabla u|))^\alpha} \frac{1}{|x-y|^\gamma} \leq \mathcal{C} \tag{10.1.7}$$

with $1 < \alpha < 1 + \frac{1}{\vartheta}$, $\gamma < N - 2$, if $N \geq 3$ and $\gamma = 0$ if $N = 2$ and $\mathcal{C} = \mathcal{C}(\gamma, m_A, M_A, q, f, b, ||\nabla u||_\infty, \rho, x_0, \alpha)$.
The same result follows if we assume that $f(x) \leq c(\rho, x_0) < 0$ in $B_{2\rho}(x_0) \subset \Omega$.
In particular $\mathcal{L}(\{A(|\nabla u|) = 0\}) = 0$.

Theorem 10.1.4 is actually an estimate on the way the operator degenerate near the critical set. It might have future applications in the study of the qualitative properties of the solutions. Here, has a consequence, we shall point out a further correlated regularity result, see Theorem 10.1.5 below. Before we start observing that the estimates in Theorem 10.1.4 and in Theorem 10.1.3 (namely (10.1.6) and (10.1.7)), holds in a general compact set of Ω.The same regularity holds all over the domain once we assume that there are no critical points of the solutions up to the boundary, namely $Z_u \cap \partial\Omega = \emptyset$. This an abstract assumption always verified each time we may exploit the Hopf boundary lemma, see [121]. The global regularity results follow via a covering argument and the proofs and the statements are postponed in Section 10.4, see Theorem 10.4.1 and Theorem 10.4.2.

As mentioned here above, the estimates on the second derivatives and the estimates of the summability of the weight can be exploited jointly in order to obtain the following

Theorem 10.1.5. *Let $\Omega \subset \mathbb{R}^N$ a bounded smooth domain and let $u \in C^{1,\alpha}(\bar{\Omega}) \cap C^2(\Omega \setminus Z_u)$ be a solution to (10.1.1) with $f, b \in W^{1,\infty}(\Omega)$. Assume that f is positive in Ω (possibly vanishing on the boundary). Then*

$$u \in W^{2,s}(\mathcal{K}) \qquad \text{for any } s < \min\{2\,;\, 1 + \tilde{\vartheta}^{-1}\} \tag{10.1.8}$$

for every compact set $\mathcal{K} \subset \Omega$, with $u_{ij} = 0$ on Z_u for $ij = 1, \dots, N$. If we further assume that $Z_u \cap \partial\Omega = \emptyset$, then

$$u \in W^{2,s}(\Omega) \qquad \text{for any } s < \min\{2\,;\, 1 + \tilde{\vartheta}^{-1}\}\,. \tag{10.1.9}$$

This remaining part is organized as follows: We prove the local regularity of the second derivatives in Section 10.2, while the summability of the weight is studied in Section 10.3. The covering argument needed to obtain the global results is developed in Section 10.4, where e also prove Theorem 10.1.5.

10.2 Local regularity

We begin by remarking that, if $u \in C^{1,\alpha}(\Omega) \cap C^2(\Omega \setminus Z_u)$ is a solution of (10.1.1), then the derivatives of the solution are solutions to the linearised equation, i. e.

$$\begin{aligned} L_u(u_i, \phi) = &\int_\Omega A(|\nabla u|)(\nabla u_i, \nabla \phi) dx + \int_\Omega \frac{A'(|\nabla u|)}{|\nabla u|}(\nabla u, \nabla u_i)(\nabla u, \nabla \phi)\, dx \\ &+ \int_\Omega b_i(x)|\nabla u|^q \phi\, dx + q \int_\Omega b(x)|\nabla u|^{q-2}(\nabla u, \nabla u_i)\phi\, dx \\ &- \int_\Omega f_i, \phi\, dx = 0 \end{aligned} \tag{10.2.10}$$

for every $\phi \in C_c^\infty(\Omega \setminus Z_u)$. This follows just putting ϕ_i as test function in (10.1.1) and integrating by parts.

To exploit such equation we will use a regularization argument. For $\varepsilon > 0$ we consider $G_\varepsilon(t) = (2t - 2\varepsilon)\chi_{[\varepsilon, 2\varepsilon]}(t) + t\chi_{[2\varepsilon, \infty)}(t)$ for $t > 0$, while $G_\varepsilon(t) = -G_\varepsilon(-t)$ for $t \leq 0$ ($\chi_{[a,b]}(\cdot)$ denoting the characteristic function of a set). We will assume that the ball $B_{2\rho}(x_0)$ is contained in Ω and we will consider a cut-off function $\varphi_\rho = \varphi \in C_c^\infty(B_{2\rho}(x_0))$ such that

$$\begin{aligned} &\varphi = 1, \text{ in } B_\rho(x_0) \\ &|\nabla \varphi| \leq \frac{2}{\rho}\,. \end{aligned} \tag{10.2.11}$$

Also, for $\beta \in [0, 1)$ and $\gamma < N - 2$ if $N \geq 3$ ($\gamma = 0$ for $N = 2$) fixed, we set

$$T_\varepsilon(t) = \frac{G_\varepsilon(t)}{|t|^\beta}, \quad H_\delta(t) = \frac{G_\delta(t)}{|t|^{\gamma+1}}\,. \tag{10.2.12}$$

Proof of Theorem 10.1.3. Let us consider the test function

$$\phi = T_\varepsilon(u_i)\ H_\delta(|x - y|)\ \varphi^2 = T_\varepsilon(u_i)\ H_\delta\ \varphi^2\,. \tag{10.2.13}$$

According to (10.2.12), it follows that such a test function can be plugged in the linearised equation (10.2.10), since it vanishes in a neighbourhood of the critical set Z_u. Consequently by (10.2.10) we get

$$\begin{aligned} &\int_\Omega A(|\nabla u|)|\nabla u_i|^2\ T_\varepsilon'(u_i)\ H_\delta\ \varphi^2 + \int_\Omega \frac{A'(|\nabla u|)}{|\nabla u|}(\nabla u, \nabla u_i)^2\ T_\varepsilon'(u_i)\ H_\delta\ \varphi^2 \\ &+ \int_\Omega A(|\nabla u|)(\nabla u_i, \nabla_x H_\delta)\ T_\varepsilon(u_i)\ \varphi^2 + \int_\Omega \frac{A'(|\nabla u|)}{|\nabla u|}(\nabla u, \nabla u_i)(\nabla u, \nabla_x H_\delta)\ T_\varepsilon(u_i)\ \varphi^2 \\ &+ 2\int_\Omega A(|\nabla u|)(\nabla u_i, \nabla \varphi)\ T_\varepsilon(u_i)\ H_\delta\ \varphi + 2\int_\Omega \frac{A'(|\nabla u|)}{|\nabla u|}(\nabla u, \nabla u_i)(\nabla u, \nabla \varphi)\ T_\varepsilon(u_i)\ H_\delta\ \varphi \\ &+ q\int_\Omega b(x)|\nabla u|^{q-2}(\nabla u, \nabla u_i) \cdot T_\varepsilon(u_i) \cdot H_\delta \cdot \varphi^2 + \int_\Omega b_i(x)|\nabla u|^q \cdot T_\varepsilon(u_i) \cdot H_\delta \cdot \varphi^2 \\ &= \int_\Omega f_i \cdot T_\varepsilon(u_i) \cdot H_\delta \cdot \varphi^2\,. \end{aligned} \tag{10.2.14}$$

It is convenient to set:

$$\begin{aligned} I_1(\varepsilon,\delta) &= \int_\Omega A(|\nabla u|)|\nabla u_i|^2\ T_\varepsilon'(u_i)\ H_\delta\ \varphi^2 \\ I_2(\varepsilon,\delta) &= \int_\Omega \frac{A'(|\nabla u|)}{|\nabla u|}(\nabla u,\nabla u_i)^2\ T_\varepsilon'(u_i)\ H_\delta\ \varphi^2 \end{aligned} \tag{10.2.15}$$

and

$$\begin{aligned} I_3(\varepsilon,\delta) &= \int_\Omega A(|\nabla u|)(\nabla u_i,\nabla_x H_\delta)\ T_\varepsilon(u_i)\ \varphi^2 \\ I_4(\varepsilon,\delta) &= \int_\Omega \frac{A'(|\nabla u|)}{|\nabla u|}(\nabla u,\nabla u_i)(\nabla u,\nabla_x H_\delta)\ T_\varepsilon(u_i)\ \varphi^2 \\ I_5(\varepsilon,\delta) &= 2\int_\Omega A(|\nabla u|)(\nabla u_i,\nabla\varphi)\ T_\varepsilon(u_i)\ H_\delta\ \varphi \\ I_6(\varepsilon,\delta) &= 2\int_\Omega \frac{A'(|\nabla u|)}{|\nabla u|}(\nabla u,\nabla u_i)(\nabla u,\nabla\varphi)\ T_\varepsilon(u_i)\ H_\delta\ \varphi \\ I_7(\varepsilon,\delta) &= q\int_\Omega b(x)|\nabla u|^{q-2}(\nabla u,\nabla u_i)\cdot T_\varepsilon(u_i)\cdot H_\delta\cdot\varphi^2 \\ I_8(\varepsilon,\delta) &= \int_\Omega b_i(x)|\nabla u|^q\cdot T_\varepsilon(u_i)\cdot H_\delta\cdot\varphi^2 \\ I_9(\varepsilon,\delta) &= \int_\Omega f_i\cdot T_\varepsilon(u_i)\cdot H_\delta\cdot\varphi^2\,. \end{aligned}$$

Regarding the terms I_1 and I_2, exploiting (10.1.3), we note that

$$I_1 + I_2 \geq \int_\Omega A(|\nabla u|)|\nabla u_i|^2\ T_\varepsilon'(u_i)\ H_\delta\ \varphi^2 \tag{10.2.16}$$

when $A'(|\nabla u|)$ is nonnegative, while

$$I_1+I_2 \geq \int_\Omega A(|\nabla u|)|\nabla u_i|^2\ T_\varepsilon'(u_i)\ H_\delta\ \varphi^2 - \int_\Omega |A'(|\nabla u|)||\nabla u||\nabla u_i|^2\ T_\varepsilon'(u_i)\ H_\delta\ \varphi^2$$

when $A'(|\nabla u|)$ is negative. Therefore

$$I_1 + I_2 \geq (1+m_A)\, I_1\,. \tag{10.2.17}$$

Thence, from (10.2.14), we get

$$(1+m_A)\int_\Omega A(|\nabla u|)|\nabla u_i|^2\ T_\varepsilon'(u_i)\ H_\delta\ \varphi^2 \leq |I_3| + ... + |I_9|\,. \tag{10.2.18}$$

Now we estimate the right hand side of (10.2.18) letting $\delta \to 0$. In fact, using the fact that $|T_\varepsilon(t)| \leq t^{1-\beta}$ and the Young inequality $ab \leq \vartheta a^2 + \frac{b^2}{4\vartheta}$,

we deduce that

$$\begin{aligned}
\limsup_{\delta\to 0}(|I_3|+|I_4|) &\le \gamma\int_\Omega [A(|\nabla u|)+|A'(|\nabla u|)||\nabla u|]\ |\nabla u_i|\frac{|T_\varepsilon(u_i)|}{|x-y|^{\gamma+1}}\varphi^2\\
&\underset{by(10.1.3)}{\le} \gamma(1+|M_A|)\int_\Omega A(|\nabla u|)|\nabla u_i|\frac{|T_\varepsilon(u_i)|}{|x-y|^{\gamma+1}}\varphi^2\\
&\le \gamma(1+|M_A|)\int_\Omega \frac{\sqrt{A(|\nabla u|)}\ |\nabla u_i|}{|x-y|^{\frac{\gamma}{2}}|u_i|^{\frac{\beta}{2}}}\chi_{\{|u_i|\ge\varepsilon\}}\varphi\ \ \frac{\sqrt{A(|\nabla u|)}\ |u_i|^{\frac{2-\beta}{2}}}{|x-y|^{\frac{\gamma+2}{2}}}\varphi\\
&\le \vartheta\int_\Omega \frac{A(|\nabla u|)|\nabla u_i|^2}{|x-y|^\gamma|u_i|^\beta}\chi_{\{|u_i|\ge\varepsilon\}}\varphi^2+\frac{\gamma^2(1+|M_A|)^2}{4\vartheta}\int_\Omega\frac{A(|\nabla u|)|u_i|^{2-\beta}}{|x-y|^{\gamma+2}}\varphi^2\\
&\le \vartheta\int_\Omega \frac{A(|\nabla u|)|\nabla u_i|^2}{|x-y|^\gamma|u_i|^\beta}\chi_{\{|u_i|\ge\varepsilon\}}\varphi^2+\frac{\gamma^2(1+|M_A|)^2}{4\vartheta}\int_\Omega\frac{A(|\nabla u|)|\nabla u|^{2-\beta}}{|x-y|^{\gamma+2}}\varphi^2\\
&\le \vartheta\int_\Omega \frac{A(|\nabla u|)|\nabla u_i|^2}{|x-y|^\gamma|u_i|^\beta}\chi_{\{|u_i|\ge\varepsilon\}}\varphi^2+\frac{\gamma^2(1+|M_A|)^2M\hat{C}_1(L)}{4\vartheta},
\end{aligned}\tag{10.2.19}$$

where we also used the fact that $A(t)t$ is locally bounded and we have set

$$\begin{aligned}
&M=M(\rho,x_0,\gamma,\Omega)=\\
&=\max\Big\{\sup_{y\in\Omega}\int_{B_{2\rho}(x_0)}\frac{1}{|x-y|^\gamma}dx;\ \sup_{y\in\Omega}\int_{B_{2\rho}(x_0)}\frac{1}{|x-y|^{\gamma+1}}dx;\ \sup_{y\in\Omega}\int_{B_{2\rho}(x_0)}\frac{1}{|x-y|^{\gamma+2}}dx\Big\}\\
&L=L(\rho,x_0)=\sup_{x\in B_{2\rho}(x_0)}|\nabla u|\,.
\end{aligned}\tag{10.2.20}$$

Exploiting the fact that $|\nabla\varphi|\le\frac{2}{\rho}$, $|T_\varepsilon(t)|\le t^{1-\beta}$ and the Young inequality, we also get that

$$\begin{aligned}
\limsup_{\delta\to 0}(|I_5|+|I_6|) &\le 2\int_\Omega [A(|\nabla u|)+|A'(|\nabla u|)||\nabla u|]\ |\nabla u_i||\nabla\varphi|\frac{|T_\varepsilon(u_i)|}{|x-y|^\gamma}\varphi\\
&\underset{by(10.1.3)}{\le}\frac{4(1+|M_A|)}{\rho}\int_\Omega\frac{\sqrt{A(|\nabla u|)}\ |\nabla u_i|}{|x-y|^{\frac{\gamma}{2}}|u_i|^{\frac{\beta}{2}}}\chi_{\{|u_i|\le\varepsilon\}}\varphi\ \ \frac{\sqrt{A(|\nabla u|)}\ |u_i|^{\frac{2-\beta}{2}}}{|x-y|^{\frac{\gamma}{2}}}\\
&\le \vartheta\int_\Omega\frac{A(|\nabla u|)|\nabla u_i|^2}{|x-y|^\gamma|u_i|^\beta}\chi_{\{|u_i|\ge\varepsilon\}}\varphi^2+\frac{4(1+|M_A|)^2}{\vartheta\rho^2}\int_{B_{2\rho}(x_0)}\frac{A(|\nabla u|)|\nabla u|^{2-\beta}}{|x-y|^\gamma}\\
&\le \vartheta\int_\Omega\frac{A(|\nabla u|)|\nabla u_i|^2}{|x-y|^\gamma|u_i|^\beta}\chi_{\{|u_i|\ge\varepsilon\}}\varphi^2+\frac{4(1+|M_A|)^2M\hat{C}_2(L)}{\vartheta\rho^2}\,.
\end{aligned}\tag{10.2.21}$$

Now we set $B = \sup_{x\in B_{2\rho}(x_0)} |b(x)|$ and we get

$$\begin{aligned}
\limsup_{\delta\to 0} |I_7| &\le qB \int_\Omega |\nabla u|^{q-1} |\nabla u_i| \frac{|T_\varepsilon(u_i)|}{|x-y|^\gamma}\varphi^2 \\
&\le \int_\Omega \frac{\sqrt{A(|\nabla u|)}\ |\nabla u_i|}{|x-y|^{\frac{\gamma}{2}} |u_i|^{\frac{\beta}{2}}} \chi_{\{|u_i|\le\varepsilon\}}\varphi \quad |q|B \frac{|\nabla u|^{q-1}\ |u_i|^{\frac{2-\beta}{2}}}{\sqrt{A(|\nabla u|)}\ |x-y|^{\frac{\gamma}{2}}}\varphi \\
&\le \vartheta \int_\Omega \frac{A(|\nabla u|)|\nabla u_i|^2}{|x-y|^\gamma |u_i|^\beta}\chi_{\{|u_i|\ge\varepsilon\}}\varphi^2 + \frac{q^2B^2}{4\vartheta}\int_\Omega \frac{|\nabla u|^{2q-2}|u_i|^{2-\beta}}{A(|\nabla u|)\ |x-y|^\gamma}\varphi^2 \\
&\underset{by(10.1.4)}{\le} \vartheta \int_\Omega \frac{A(|\nabla u|)|\nabla u_i|^2}{|x-y|^\gamma |u_i|^\beta}\chi_{\{|u_i|\ge\varepsilon\}}\varphi^2 + \frac{q^2B^2}{4K\vartheta}\int_\Omega \frac{|\nabla u|^{1-\beta}}{|x-y|^\gamma}\varphi^2 \\
&\le \vartheta \int_\Omega \frac{A(|\nabla u|)|\nabla u_i|^2}{|x-y|^\gamma |u_i|^\beta}\chi_{\{|u_i|\ge\varepsilon\}}\varphi^2 + \frac{q^2B^2M\hat{C}_3(L)}{4K\vartheta}\,.
\end{aligned} \tag{10.2.22}$$

Setting $B_I = \sup_{x\in B_{2\rho}(x_0)} \sum_{i=1}^N |b_i(x)|$ we also deduce that

$$\limsup_{\delta\to 0} |I_8| \le B_I \int_\Omega |\nabla u|^q \frac{|u_i|^{1-\beta}}{|x-y|^\gamma}\varphi^2 \le B_I \int_{B_{2\rho(x_0)}} \frac{|\nabla u|^{q+1-\beta}}{|x-y|^\gamma} \le B_I M\hat{C}_4(L)\,. \tag{10.2.23}$$

Finally, setting $F = \sup_{x\in B_{2\rho}(x_0)} \sum_{i=1}^N |f_i(x)|$, we get that

$$\limsup_{\delta\to 0} |I_9| \le F \int_\Omega \frac{|u_i|^{1-\beta}}{|x-y|^\gamma}\varphi^2 \le FM\hat{C}_5(L)\,. \tag{10.2.24}$$

Taking into account (10.2.18), letting $\delta \to 0$, exploiting the above estimates and evaluating T'_ε, we get

$$\begin{aligned}
&(1+m_A)\int_\Omega \frac{A(|\nabla u|)|\nabla u_i|^2}{|x-y|^\gamma}\left(\frac{G'_\varepsilon(u_i)}{|u_i|^\beta} - \beta\frac{G_\varepsilon(u_i)}{|u_i|^{1+\beta}}\right)\varphi^2 - 3\vartheta\int_\Omega \frac{A(|\nabla u|)|\nabla u_i|^2}{|x-y|^\gamma |u_i|^\beta}\chi_{\{|u_i|\ge\varepsilon\}}\varphi^2 \\
&\quad\le \frac{\gamma^2(1+|M_A|)^2M\hat{C}_1(L)}{4\vartheta} + \frac{4(1+|M_A|)^2M\hat{C}_2(L)}{\vartheta\rho^2} + \frac{q^2B^2M\hat{C}_3(L)}{4K\vartheta} \\
&\quad + B_IM\hat{C}_4(L) + FM\hat{C}_5(L)\,.
\end{aligned} \tag{10.2.25}$$

Now we fix ϑ sufficiently small such that

$$(1+m_A)\left(G'_\varepsilon(u_i) - \beta\frac{G_\varepsilon(u_i)}{|u_i|}\right) - 3\vartheta\chi_{\{|u_i|\ge\varepsilon\}} > 0 \tag{10.2.26}$$

so that

$$\int_{B_\rho(x_0)} \frac{A(|\nabla u|)|\nabla u_i|^2}{|x-y|^\gamma |u_i|^\beta} \le \int_{B_{2\rho}(x_0)} \frac{A(|\nabla u|)|\nabla u_i|^2}{|x-y|^\gamma |u_i|^\beta}\varphi^2 \le \mathsf{C} \tag{10.2.27}$$

where $\mathsf{C} = \mathsf{C}(\gamma, \beta, q, f, b, ||\nabla u||_\infty, \rho, x_0)$. □

10.3 Local summability of the weight

We exploit here the summability properties of the second derivatives of the solution proved in Theorem 10.1.3 to obtain information on the summability of $(A(|\nabla u|))^{-1}$.

Proof of Theorem 10.1.3. Consider

$$\phi = \frac{1}{(\varepsilon + A(|\nabla u|))^{\alpha}} H_\delta(|x-y|)\varphi^2 = \frac{1}{(\varepsilon + A(|\nabla u|))^{\alpha}} H_\delta \varphi^2 \tag{10.3.28}$$

with $\varepsilon > 0$, φ and H_δ defined as in (10.2.11) and (10.2.12). Note that ϕ can be used as test function in (10.1.5), so that

$$\begin{aligned}
&\int_{B_{2\rho}(x_0)} f(x)\phi = \int_{B_{2\rho}(x_0)} f(x) \frac{1}{(\varepsilon + A(|\nabla u|))^{\alpha}} H_\delta\ \varphi^2 \\
&= -\alpha \int_{B_{2\rho}(x_0)} \frac{A(|\nabla u|)(\nabla u, \nabla |\nabla u| A'(|\nabla u|))}{(\varepsilon + A(|\nabla u|))^{\alpha+1}} H_\delta\ \varphi^2 \\
&+ \int_{B_{2\rho}(x_0)} \frac{A(|\nabla u|)(\nabla u, \nabla_x H_\delta)}{(\varepsilon + A(|\nabla u|))^{\alpha}} \varphi^2 + 2 \int_{B_{2\rho}(x_0)} \frac{A(|\nabla u|)(\nabla u, \nabla \varphi)}{(\varepsilon + A(|\nabla u|))^{\alpha}} H_\delta\ \varphi \\
&+ \int_{B_{2\rho}(x_0)} \frac{b(x)|\nabla u|^q}{(\varepsilon + A(|\nabla u|))^{\alpha}} H_\delta\ \varphi^2 .
\end{aligned} \tag{10.3.29}$$

It is convenient to set:

$$\begin{aligned}
I_o &= \int_{B_{2\rho}(x_0)} \frac{1}{(\varepsilon + A(|\nabla u|))^{\alpha} |x-y|^{\gamma}} \varphi^2 \\
I_a &= -\alpha \int_{B_{2\rho}(x_0)} \frac{A(|\nabla u|)(\nabla u, \nabla |\nabla u| A'(|\nabla u|))}{(\varepsilon + A(|\nabla u|))^{\alpha+1}} H_\delta\ \varphi^2 \\
I_b &= \int_{B_{2\rho}(x_0)} \frac{A(|\nabla u|)(\nabla u, \nabla_x H_\delta)}{(\varepsilon + A(|\nabla u|))^{\alpha}} \varphi^2 \\
I_c &= 2 \int_{B_{2\rho}(x_0)} \frac{A(|\nabla u|)(\nabla u, \nabla \varphi)}{(\varepsilon + A(|\nabla u|))^{\alpha}} H_\delta\ \varphi \\
I_d &= \int_{B_{2\rho}(x_0)} \frac{b(x)|\nabla u|^q}{(\varepsilon + A(|\nabla u|))^{\alpha}} H_\delta\ \varphi^2 .
\end{aligned} \tag{10.3.30}$$

Recalling that we are assuming that the source therm f is positive, we deduce that

$$c(\rho, x_0) \int_{B_{2\rho}(x_0)} \frac{1}{(\varepsilon + A(|\nabla u|))^{\alpha}} H_\delta\ \varphi^2 \le |I_a| + |I_b| + |I_c| + |I_d| . \tag{10.3.31}$$

In the following we let $\delta \to 0$ and exploit the Young inequality $ab \le \vartheta a^2 + \frac{b^2}{4\vartheta}$

and Theorem 10.1.3, obtaining

$$\begin{aligned}
\limsup_{\delta\to 0}|I_a| &\le \alpha\int_{B_{2\rho}(x_0)}\frac{A(|\nabla u|)|A'(|\nabla u|)||\nabla u|}{(\varepsilon+A(|\nabla u|))^{\alpha+1}}\sum_{i=1}^N|\nabla u_i|\frac{1}{|x-y|^\gamma}\ \varphi^2\\
&= \alpha\int_{B_{2\rho}(x_0)}\frac{1}{(\varepsilon+A(|\nabla u|))^{\frac{\alpha}{2}}|x-y|^{\frac{\gamma}{2}}}\varphi\ \frac{A(|\nabla u|)|A'(|\nabla u|)||\nabla u|}{(\varepsilon+A(|\nabla u|))^{\frac{\alpha}{2}+1}}\frac{\sum_{i=1}^N|\nabla u_i|}{|x-y|^{\frac{\gamma}{2}}}\ \varphi\\
&\le \alpha\vartheta I_o+\frac{1}{4\vartheta}\int_{B_{2\rho}(x_0)}\frac{(A(|\nabla u|))^2|A'(|\nabla u|)|^2|\nabla u|^2}{(\varepsilon+A(|\nabla u|))^{\alpha+2}}\Big(\sum_{i=1}^N|\nabla u_i|\Big)^2\frac{1}{|x-y|^\gamma}\ \varphi^2\\
&\le \alpha\vartheta I_o+\frac{M_A^2N}{4\vartheta}\int_{B_{2\rho}(x_0)}\frac{(A(|\nabla u|))^2}{(\varepsilon+A(|\nabla u|))^{\alpha}}\sum_{i=1}^N|\nabla u_i|^2\frac{1}{|x-y|^\gamma}\ \varphi^2\\
&\le \alpha\vartheta I_o+\frac{M_A^2\ N}{4\vartheta}\int_{B_{2\rho}(x_0)}\frac{A(|\nabla u|)|\sum_{i=1}^N|\nabla u_i|^2}{|\nabla u|^\beta|x-y|^\gamma}\varphi^2\\
&\le \alpha\vartheta I_o+\frac{M_A^2\ N^2\mathsf{C}}{4\vartheta}
\end{aligned}\tag{10.3.32}$$

with $\beta:=(\alpha-1)\tilde\vartheta$ and observing that $0\le\beta<1$ since $1<\alpha<1+\frac{1}{\tilde\vartheta}$. The constant C is the one given by Theorem 10.1.3. Now we proceed further observing that

$$\begin{aligned}
\limsup_{\delta\to 0}|I_b| &\le \gamma\int_{B_{2\rho}(x_0)}\frac{A(|\nabla u|)|\nabla u|}{(\varepsilon+A(|\nabla u|))^{\alpha}|x-y|^{\gamma+1}}\varphi^2\\
&\le \gamma\int_{B_{2\rho}(x_0)}\frac{|\nabla u|}{(A(|\nabla u|))^{\alpha-1}}\ \frac{1}{|x-y|^{\gamma+1}}\varphi^2\\
&\le \frac{\gamma}{K^{\alpha-1}}\int_{B_{2\rho}(x_0)}\frac{|\nabla u|}{|\nabla u|^{\tilde\vartheta(\alpha-1)}}\ \frac{1}{|x-y|^{\gamma+1}}\varphi^2\\
&\le \gamma\frac{M\hat C_6(L)}{K^{\alpha-1}}
\end{aligned}\tag{10.3.33}$$

where M and L are defined as in (10.2.20) and we are also using the fact that $\tilde\vartheta(\alpha-1)<1$. Similarly, recalling that $|\nabla\varphi|\le\frac{2}{\rho}$, we get

$$\begin{aligned}
\limsup_{\delta\to 0}|I_c| &\le 2\int_{B_{2\rho}(x_0)}\frac{A(|\nabla u|)|\nabla u||\nabla\varphi|}{(\varepsilon+A(|\nabla u|))^{\alpha}}\ \frac{1}{|x-y|^\gamma}\varphi\\
&\le \frac{4}{\rho K^{\alpha-1}}\int_{B_{2\rho}(x_0)}\frac{|\nabla u|}{|\nabla u|^{\tilde\vartheta(\alpha-1)}}\ \frac{1}{|x-y|^\gamma}\varphi\\
&\le \frac{4M\hat C_7(L)}{\rho K^{\alpha-1}}\,.
\end{aligned}\tag{10.3.34}$$

As above we use the notation $B = \sup_{x\in B_{2\rho}(x_0)} |b(x)|$. We have

$$\begin{aligned}
\limsup_{\delta\to 0} |I_d| &\le \int_{B_{2\rho}(x_0)} \frac{|b(x)||\nabla u|^q}{(\varepsilon + A(|\nabla u|))^\alpha} \frac{1}{|x-y|^\gamma}\varphi^2 \\
&\le \int_{B_{2\rho}(x_0)} \frac{1}{(\varepsilon + A(|\nabla u|))^{\frac{\alpha}{2}}|x-y|^{\frac{\gamma}{2}}}\varphi \; B\frac{|\nabla u|^q}{(\varepsilon + A(|\nabla u|))^{\frac{\alpha}{2}}|x-y|^{\frac{\gamma}{2}}}\varphi \\
&\le \vartheta I_o + \frac{B^2}{4\vartheta}\int_{B_{2\rho}(x_0)} \frac{|\nabla u|^{2q}}{(A(|\nabla u|))^\alpha} \frac{1}{|x-y|^\gamma}\varphi^2 \\
&\underset{Hp\ 6}{\le} \vartheta I_o + \frac{B^2}{4\vartheta K^\alpha}\int_{B_{2\rho}(x_0)} \frac{|\nabla u|^{2q}}{|\nabla u|^{\alpha\tilde{\vartheta}}} \frac{1}{|x-y|^\gamma}\varphi^2 \\
&\le \vartheta I_o + \frac{B^2 M\hat{C}_8(L)}{4\vartheta K^\alpha}
\end{aligned} \tag{10.3.35}$$

observing that $2q > \alpha\tilde{\vartheta}$ since $q > \frac{\tilde{\vartheta}+1}{2}$ and $1 < \alpha < 1 + \frac{1}{\tilde{\vartheta}}$.

Collecting the previous estimates, by (10.3.31), and letting $\delta \to 0$ we have

$$\begin{aligned}
&(c(\rho, x_0) - (\alpha+1)\vartheta)\int_{B_{2\rho}(x_0)} \frac{1}{(\varepsilon + A(|\nabla u|))^\alpha |x-y|^\gamma}\varphi^2 \\
&\le \frac{M_A^2\, N^2 \mathsf{C}}{4\vartheta} + \gamma\frac{M\hat{C}_6(L)}{K^{\alpha-1}} + \frac{4M\hat{C}_7(L)}{\rho K^{\alpha-1}} + \frac{B^2 M\hat{C}_8(L)}{4\vartheta K^\alpha}\,.
\end{aligned} \tag{10.3.36}$$

For ϑ sufficient small such that $(c(\rho, x_0) - (\alpha+1)\vartheta) > 0$, letting $\varepsilon \to 0$, we get the thesis

$$\int_{B_\rho(x_0)} \frac{1}{(A(|\nabla u|))^\alpha}\frac{1}{|x-y|^\gamma} \le \int_{B_{2\rho}(x_0)} \frac{1}{(A(|\nabla u|))^\alpha |x-y|^\gamma}\varphi^2 \le \mathcal{C} \tag{10.3.37}$$

where $\mathcal{C} = \mathcal{C}(\gamma, \beta, q, f, b, ||\nabla u||_\infty, \rho, x_0, \alpha)$. □

10.4 Global results

In this section we deduce global regularity information, starting from the local regularity results already proved. Let us define the neighbourhood $I_\delta(\partial\Omega) = \{x \in \Omega | d(x, \partial\Omega) \le \delta\}$. Without loss of generality, in all the section, we will assume that

$$\Omega\backslash I_{3\delta}(\partial\Omega) \subset \bigcup_{i=1}^{S} B_\rho(x_i)$$

and $x_i \in \overline{\Omega\backslash I_{3\delta}(\partial\Omega)}$ and $\rho < \delta$. We will state our results under the general assumption

$$Z_u \cap \partial\Omega = \emptyset\,.$$

This assumption is verified in all the situations when the Hopf boundary Lemma holds, we refer therefore to [121] .

Theorem 10.4.1. *Let $\Omega \subset \mathbb{R}^N$ a bounded smooth domain and let $u \in C^{1,\alpha}(\bar{\Omega}) \cap C^2(\Omega \setminus Z_u)$ be a solution to (10.1.1) with $f, b \in W^{1,\infty}(\Omega)$. Then for every $i = 1, ..., N$, $0 \le \beta < 1$ and $\gamma < N-2$ ($\gamma = 0$ if $N = 2$), we have*

$$\int_{\mathcal{K}} \frac{A(|\nabla u|)|\nabla u_i|^2}{|x-y|^\gamma |u_i|^\beta}\, dx \le \overline{\mathsf{C}}^*(\mathcal{K}) \qquad \forall y \in \Omega, \tag{10.4.38}$$

for any compact set $\mathcal{K} \subset \Omega$. If we also assume that $Z_u \cap \partial\Omega = \emptyset$, then

$$\int_{\Omega} \frac{A(|\nabla u|)|\nabla u_i|^2}{|x-y|^\gamma |u_i|^\beta}\, dx \le \overline{\mathsf{C}}^* \qquad \forall y \in \Omega\,. \tag{10.4.39}$$

Proof. The proof follows via a covering argument. We directly prove the estimate in (10.4.39), since the estimate in (10.4.38) follows with the same proof more easily. In all the proof the reader should take into account that we are integrating with respect the x-variable, and the center of the kernel y is varying all over the domain. Under our assumptions, we can take $\delta > 0$ such that there are no critical points of the solution in the neighbourhood $I_{3\delta}(\partial\Omega)$. It follows therefore in this case that $A(|\nabla u|) > 0$ in $I_{3\delta}(\partial\Omega)$ and $u \in \mathcal{C}^2(3\delta(\partial\Omega))$. We set

$$\begin{aligned}
&\overline{M} = \max\Big\{ \sup_{y\in\Omega} \int_\Omega \frac{1}{|x-y|^\gamma} dx;\ \sup_{y\in\Omega} \int_\Omega \frac{1}{|x-y|^{\gamma+1}} dx;\ \sup_{y\in\Omega} \int_\Omega \frac{1}{|x-y|^{\gamma+2}} dx \Big\} \\
&\overline{L} = \sup_{x\in\Omega} |\nabla u| \\
&\overline{B} = \sup_{x\in\Omega} |b(x)|, \quad \bar{B}_I = \sup_{x\in\Omega} \sum_{i=1}^N |b_i(x)| \\
&\overline{F} = \sup_{x\in\Omega} \sum_{i=1}^N |f_i(x)|
\end{aligned} \tag{10.4.40}$$

and, repeating verbatim the argument of the proof of Theorem 10.1.3 with the new notations, we get that

$$\int_{B_\rho(x_i)} \frac{A(|\nabla u|)|\nabla u_i|^2}{|x-y|^\gamma |u_i|^\beta} \le \hat{\mathsf{C}}(\gamma, \beta, q, m_A, M_A, \bar{M}, \bar{L}, \bar{B}, \bar{F})\,. \tag{10.4.41}$$

Therefore

$$\int_{\Omega\setminus I_{3\delta}(\partial\Omega)} \frac{A(|\nabla u|)|\nabla u_i|^2}{|x-y|^\gamma |u_i|^\beta} \le \sum_{i=1}^S \int_{B_\rho(x_i)} \frac{A(|\nabla u|)|\nabla u_i|^2}{|x-y|^\gamma |u_i|^\beta} \le S\hat{\mathsf{C}}\,. \tag{10.4.42}$$

Setting

$$\begin{aligned}
&\bar{A} = \sup_{x\in I_{3\delta}} A(|\nabla u|)|\nabla u|^\beta < \infty \\
&\overline{D} = \sup_{x\in I_{3\delta}(\partial\Omega)} \sum_{i,j} |u_{ij}|^2
\end{aligned} \tag{10.4.43}$$

we also have that

$$\int_{I_{3\delta}(\partial\Omega)} \frac{A(|\nabla u|)|\nabla u_i|^2}{|x-y|^\gamma |u_i|^\beta} \le \int_{I_{3\delta}(\partial\Omega)} \frac{A(|\nabla u|)|\nabla u|^{-\beta}|\nabla u_i|^2}{|x-y|^\gamma} \le \overline{A}\,\overline{D}\,\overline{M}\,. \tag{10.4.44}$$

Finally, by (10.4.42) and (10.4.44), we deduce that

$$\begin{aligned}\int_\Omega \frac{A(|\nabla u|)|\nabla u_i|^2}{|x-y|^\gamma |u_i|^\beta} &\le \int_{\Omega\setminus I_{3\delta}(\partial\Omega)} \frac{A(|\nabla u|)|\nabla u_i|^2}{|x-y|^\gamma |u_i|^\beta} + \int_{I_{3\delta}(\partial\Omega)} \frac{A(|\nabla u|)|\nabla u_i|^2}{|x-y|^\gamma |u_i|^\beta} \\ &\le S\hat{\mathsf{C}} + \overline{A}\,\overline{D}\,\overline{M} = \overline{\mathsf{C}}^*\,.\end{aligned} \tag{10.4.45}$$

□

We prove here a global summability result for $(A|\nabla u|)^{-1}$ using Theorem 10.4.1.

Let as above I_δ be the neighbourhood of $\partial\Omega$ of radius δ and consider the same covering

$$\Omega\setminus I_{3\delta}(\partial\Omega) \subset \bigcup_{i=1}^{S} B_\rho(x_i)$$

with $x_i \in \overline{\Omega\setminus I_{3\delta}(\partial\Omega)}$ and $\rho < \delta$. We set

$$\begin{aligned}\bar{\lambda} &= \inf_{x\in I_{3\delta}} A(|\nabla u|) \\ \mu &= \inf_{x\in\Omega\setminus I_\delta} f(x)\,.\end{aligned} \tag{10.4.46}$$

Theorem 10.4.2. *Let $\Omega \subset \mathbb{R}^N$ a bounded smooth domain and let $u \in C^{1,\alpha}(\bar{\Omega})\cap C^2(\Omega\setminus Z_u)$ be a solution to (10.1.1) with $f, b \in W^{1,\infty}(\Omega)$. Assume that f is positive in Ω (possibly vanishing on the boundary). Then, for every compact set $\mathcal{K} \subset \Omega$, we have*

$$\int_{\mathcal{K}} \frac{1}{(A(|\nabla u|))^\alpha} \frac{1}{|x-y|^\gamma} \le \overline{\mathcal{C}}^*(\mathcal{K}) \tag{10.4.47}$$

with $1 < \alpha < 1 + \frac{1}{\vartheta}$, $\gamma < N-2$, if $N \ge 3$ and $\gamma = 0$ if $N = 2$ and $\overline{\mathcal{C}}^* = \overline{\mathcal{C}}^*(\mathcal{K}, \gamma, \mu, \bar{\lambda}, m_A, M_A, \alpha, f, ||\nabla u||_\infty)$. If we further assume that $Z_u \cap \partial\Omega = \emptyset$, then

$$\int_{\Omega} \frac{1}{(A(|\nabla u|))^\alpha} \frac{1}{|x-y|^\gamma} \le \overline{\mathcal{C}}^*\,. \tag{10.4.48}$$

Proof. We deal directly with the more difficult case, namely we prove (10.4.48). In all the proof the reader should take into account that we are integrating with respect the x-variable, and the center of the kernel y is varying all over the domain. Under our assumptions, we can take $\delta > 0$ such that there are no critical points of the solution in the neighbourhood

$I_{3\delta}(\partial\Omega)$. It follows therefore that $\bar\lambda > 0$ in $I_{3\delta}$ and $u \in \mathcal{C}^2(3\delta(\partial\Omega))$. Furthermore, since f is positive in the interior of Ω, we can also assume that $\mu > 0$. By Theorem 10.4.2, since $\mu > 0$, we get that

$$\int_{B_\rho(x_i)} \frac{1}{(A(|\nabla u|))^\alpha} \frac{1}{|x-y|^\gamma} \le \hat{\mathsf{C}}(\gamma, \alpha, \mu, q, m_A, M_A, \bar M, \bar L, \bar B, \bar F)\,. \tag{10.4.49}$$

where $\overline{M}$, $\overline{L}$ and $\overline{B}$ are as in (10.4.40). Since $\bar\lambda > 0$ we also have that

$$\int_{I_{3\delta}} \frac{1}{(A(|\nabla u|))^\alpha} \frac{1}{|x-y|^\gamma} \le \frac{1}{\overline{\lambda}^\alpha}\ \overline{M}\,. \tag{10.4.50}$$

Consequently the thesis follows now via a standard covering argument, since we have

$$\begin{aligned}
&\int_\Omega \frac{1}{(A(|\nabla u|))^\alpha} \frac{1}{|x-y|^\gamma} \\
&\le \int_{I_{3\delta}} \frac{1}{(A(|\nabla u|))^\alpha} \frac{1}{|x-y|^\gamma} + \int_{\Omega\setminus I_{3\delta}} \frac{1}{(A(|\nabla u|))^\alpha} \frac{1}{|x-y|^\gamma} \\
&\le \frac{1}{\overline{\lambda}^\alpha}\ \overline{M} + \sum_{i=1}^S \int_{B_\rho(x_i)} \frac{1}{(A(|\nabla u|))^\alpha} \frac{1}{|x-y|^\gamma} \\
&\le \frac{1}{\overline{\lambda}^\alpha}\ \overline{M} + S\hat{\mathsf{C}} = \overline{\mathcal{C}}^*\,.
\end{aligned} \tag{10.4.51}$$

□

We are now ready to end the paper with the proof of Theorem 10.1.5.

Proof of Theorem 10.1.5. For any compact set $\mathcal{K} \subset \Omega$, we have

$$\begin{aligned}
\int_{\mathcal{K}} |\nabla u_i|^s\,dx &= \int_{\mathcal{K}} \frac{A(|\nabla u|)^{\frac{s}{2}} |\nabla u_i|^s}{|u_i|^{\frac{\beta\, s}{2}}} \frac{|u_i|^{\frac{\beta\, s}{2}}}{A(|\nabla u|)^{\frac{s}{2}}}\,dx \\
&\le \left(\int_{\mathcal{K}} \frac{A(|\nabla u|)|\nabla u_i|^2}{|u_i|^\beta}\,dx\right)^{\frac{s}{2}} \left(\int_{\mathcal{K}} \frac{|u_i|^{\frac{\beta\, s}{2-s}}}{A(|\nabla u|)^{\frac{s}{2-s}}}\,dx\right)^{\frac{2-s}{2}} \\
&\le (\overline{\mathsf{C}}^*(\mathcal{K}))^{\frac{s}{2}} K^{-\tilde\vartheta\beta\frac{2}{2}} \left(\int_{\mathcal{K}} \frac{A(|\nabla u|)^{\frac{\beta\, s}{(2-s)\tilde\vartheta}}}{A(|\nabla u|)^{\frac{s}{2-s}}}\,dx\right)^{\frac{2-s}{2}}\,.
\end{aligned} \tag{10.4.52}$$

Here we exploit (10.1.4) and $\overline{\mathsf{C}}^*(\mathcal{K})$ is the constant arising from Theorem 10.4.1. Under our assumption, namely for $s < 1 + \frac{1}{\tilde\vartheta}$, we can fix $\beta < 1$ with $1-\beta$ small such that

$$\frac{s}{2-s} - \frac{\beta\, s}{(2-s)\tilde\vartheta} < 1 + \frac{1}{\tilde\vartheta}\,.$$

This allows to use Theorem 10.4.2 to deduce that

$$\int_{\mathcal{K}} |\nabla u_i|^s \, dx \leq (\overline{\mathsf{C}}^*(\mathcal{K}))^{\frac{s}{2}} K^{-\tilde{\vartheta}\beta\frac{2}{2}} (\overline{\mathcal{C}}^*(\mathcal{K}))^{\frac{2-s}{2}} . \tag{10.4.53}$$

It remains to demonstrate that u_{ij}, which are defined as in Remark 10.1.2, are actually the distributional derivatives. To do this we note that, for $\varphi \in C_c^\infty(\mathcal{K})$, we have:

$$\int_{\mathcal{K}} u_{ij}\varphi \frac{G_\varepsilon(|\nabla u|)}{|\nabla u|} = -\int_{\mathcal{K}} u_i \varphi_j \frac{G_\varepsilon(|\nabla u|)}{|\nabla u|} - \int_{\mathcal{K}\cap\{\varepsilon<|\nabla u|<2\varepsilon\}} |\nabla u||\nabla u_j|\varphi\frac{1}{\varepsilon}, \tag{10.4.54}$$

since u is smooth outside the critical set Z_u and $\frac{G_\varepsilon(|\nabla u|)}{|\nabla u|}$ vanishes in a neighbourhood of Z_u. Taking into account (10.4.53) we can pass to the limit via the dominated convergence theorem. Since $\frac{G_\varepsilon(|\nabla u|)}{|\nabla u|} \to \chi_{\{\mathcal{K}\setminus Z_u\}}$ in $\mathcal{K}$ as ε tends to zero, we get the claim.
The same proof works to prove that $u \in W^{2,s}(\Omega)$ for any $s < \min\{2\,;\, 1 + \tilde{\vartheta}^{-1}\}$ once that (10.4.39) and (10.4.48) are in force. □

Conclusions

As we have discussed in the introduction, in order to find a key for better understanding the problem of the emergence of weak solutions in some particular type of nonlinear partial differential equations, a rigorous study is necessary. Following this perspective in this thesis, we have carried out in a systematic way both experimental data analysis and mathematical rigorous study.

In particular, it has been systematically studied the rapid time formation of coherent structures induced by nonlinear interaction in 2D MHD incompressible turbulent flows. It has been shown that these structures are characterised by the occurrence at small scales of regions where the correlations predicted by the hypothesis of quadratic rugged invariant conservations are locally present, a property which is the equivalent to the well known 'Beltramisation' of the fluid flows (Section I). Thus we have identified which are the equivalent of the fluid Beltrami flows in the 2D MHD incompressible turbulent case.
A further analysis is clearly necessary in order to understand if and how this phenomenology can be found also in the 3D MHD turbulence and how the emergence of coherent structures can influence the formation of weak solutions.

Moreover, a preliminary data analysis study on the formation and the excitation of the low-frequencies normal modes of magnetically confined plasma, the drift waves, has been described (Section II). Namely a data analysis has been built up in order to understand how the generated plasma column behaves when plasma dynamics, characterised by the presence of drift wave modes, occurs for magnetic field above a certain threshold. This analysis has been performed on experimental data coming from the Von-Kármán plasma experiment and even if the obtained results are still introductory, they show a good order of magnitude accordance with the plasma dynamic description given by the Hasegawa-Mima equation.

Finally, local and global regularity results for a particular type of nonlinear degenerate elliptic equations in divergence form have been presented in detail.

In conclusion in this thesis we have tried to built a multidisciplinary approach for facing the main problem of the study of weak solution emergency in particular nonlinear systems that can generate wide modes cascades and thus turbulence.

The results obtained through the systematically study of the rapid time formation of coherent structures in 2D MHD incompressible turbulent flows can be interesting in the perspective of understanding if and how these intermittent small scale structures could give rise to singular weak solutions, when letting the dissipative coefficients go to zero. In fact, the properties of the analysed structures could give a key element to understand which mathematical conditions characterise singularity emergence in weak solutions of the MHD ideal case.
On the other hand the analysis performed on the VKP experimental data, even if it is still in a preliminary stage, could be useful for building a model able to determine when and how the breakdown from regularity can occur in systems of equations describing plasma behaviour.
In parallel the final study on local and global regularity for a particular type of nonlinear degenerate elliptic equations in divergence form belongs to the wider problem of understanding which mathematical conditions guarantee existence and uniqueness of weak solutions for more general systems of partial differential equations that, under the appropriate conditions, can generate turbulence (ex. MHD equations and Hasegawa-Mima equation).

We conclude observing that more work has to be carried out in order to obtain an organic solution to the problem described in this work.

Bibliography

[1] J.-P. Antoine, R. Murenzi, P. Vandergheynst, and S. Twareque Ali. *Two-Dimensional Wavelets and their Relatives*. Cambridge University Press, 2004. 38

[2] J. T. Beale, T. Kato, and A. Majda. Remarks on the breakdown of smooth solutions for the 3d euler equations. *Comm. in Math. Phys.*, 94(1):61–66, 1984. 20, 21, 57

[3] P. Bellan. *Fundamentals of Plasma Physics*. Cambridge University Press, 2008. xiii, 9, 64, 71

[4] M. Bertero, T. A. Poggio, and V. Torre. Ill-posed problems in early vision. *Proceedings of the IEEE*, 76(8):869–889, 1988. 87

[5] D. P. Bertsekas. Multiplier methods: A survey. *Automatica*, 12(2):133–145, 1976. 90, 91

[6] D. Biskamp. *Nonlinear Magnetohydrodynamics*. Cambridge Monographs on Plasma Physics. Cambridge University Press, 1997. 2, 21, 47, 57

[7] D. Biskamp. *Magnetohydrodynamic turbulence*. Cambridge University Press, 2003. 9, 29, 33

[8] D. Biskamp and W. C. Muller. Decay laws for three dimensional magnetohydrodynamic turbulence. *Phys. Rev. Lett.*, 83(11):2195–2198, 1999. 28

[9] S. I. Braginskii. Transport processes in a plasma. *Reviews of Plasma Physics*, 1:205, 1965. 9

[10] C. Brandt. *Active control of drift wave turbulence*. PhD thesis, Ernst-Moritz-Arndt-Universität Greifswald, 2003. 97

[11] T. Buckmaster, C. De Lellis, P. Isett, and L. Székelyhidi Jr. Anomalous dissipation for 1/5 hölder euler flows. *Ann. of Math. (2)*, 182:127–172, 2015. 1, 7, 21

[12] T. Buckmaster, C. De Lellis, J. László Székelyhidi, and V. Vicol. Onsager's conjecture for admissible weak solutions. *ArXiv e-prints*, 01 2017. 1, 21

[13] R. E. Caflisch, I. Klapper, and G. Steele. Remarks on singularities, dimension and energy dissipation for ideal hydrodynamics and mhd.

Communications in Mathematical Physics, 184(2):443–455, 1997. 21, 57

[14] E. J. Candes and D. L. Donoho. Curvelets: A surprisingly effective nonadaptive representation for objects with edges. *Curve and Surface Fitting*, page 105–120, 1999. 86

[15] A. Canino, E. De Giorgio, and B. Sciunzi. Second order regularity for degenerate nonlinear elliptic equations. *Discrete Contin. Dyn. Syst.*, Accepted, April 2018. 111

[16] A. Canino, P. Le, and B. Sciunzi. Local $w^{2,m(\cdot)}_{loc}$ regularity for $p(\cdot)$-laplace equations. *Manuscripta Mathematica*, 140(3-4):481–496, 2013. 109, 112

[17] V. Carbone and P. Veltri. A simplified cascade model for mhd turbulence. *Astron. Astrophys.*, 188:239–250, 1987. 7, 25

[18] V. Carbone and P. Veltri. A shell model for anisotropic magnetohydrodynamic turbulence. *Geophys. Astrophys. Fluid Dynamics*, 52(1-3):153–181, 1990. 7, 24

[19] C. Cercignani. *Ludwig Boltzmann: The man who trusted atoms.* Clarendon Press - Oxford, 1998. 69

[20] F. F. Chen. *Lecture Notes on Langmuir Probe Diagnostics, in "Mini-Course on Plasma Diagnostics".* IEEE-ICOPS meeting, Jeju, Korea, 2003. xiv, 82, 83

[21] A. J. Chorin. The evolution of a turbulent vortex. *Comm. Math. Phys.*, 83(4):517–535, 1982. 21

[22] C. K. Chui. *An Introduction to Wavelets.* Academic Press, Inc., 1992. 36, 39

[23] M. Clausel, T. Oberlin, and V. Perrier. The monogenic synchrosqueezed wavelet transform: A tool for the decomposition/demodulation of am-fm images. *Applied and Computational Harmonic Analysis*, 39(3):450–486, 2015. 86

[24] C. Collins, N. Katz, J. Wallace, J. Jara-Almonte, I. Reese, E. Zweibel, and C. B. Forest. Stirring unmagnetized plasma. *Phys. Rev. Lett.*, 108(115):001, 2012. 79

[25] P. Constantin and A. Majda. The beltrami spectrum for incompressible fluid flows. *Comm. in Math. Phys.*, 115(3):435–456, 1988. 7

[26] P. Constantin, E. Weinan, and E. S. Titi. Onsager's conjecture on the energy conservation for solutions of euler's equation. *Communications in Mathematical Physics*, 165(1):207–209, Oct 1994. 1, 21

[27] C. M. Cooper and et all. The madison plasma dynamo experiment: a facility for studying laboratory plasma astrophysics. *Phys. Plasmas*, 21(013):505, 2014. 79

[28] F. Crispo and C. R. Grisanti. On the existence, uniqueness and $c^{1,\gamma}(\bar{\Omega})\cap w^{2,2}(\omega)$ regularity for a class of shear-thinning fluids. *Journal of Mathematical Fluid Mechanics*, 10(4):455–487, 2008. 110

[29] L. Damascelli and B. Sciunzi. Regularity, monotonicity and symmetry of positive solutions of m-laplace equations. *J. Differential Equations*, 206(2):483–515, 2004. 109, 112

[30] I. Daubechies. Orthonormal bases of compactly supported wavelets. *Communications on Pure and Applied Mathematics*, 41(7):909–996, 1988. 36, 39, 40, 86

[31] I. Daubechies, J. Lu, and H. T. Wu. Synchrosqueezed wavelet transforms: An empirical mode decomposition-like tool. *Applied and Computational Harmonic Analysis*, 30(2):243–261, 2011. 86

[32] G. David. *Wavelets and Singular Integrals on Curves and Surfaces*. Springer-Verlag, 1991. 36

[33] P. A. Davidson. *Turbulence in Rotating, Stratified and Electrically Conducting Fluids*. Cambridge University Press, 2013. 47

[34] E. De Giorgio, S. Servidio, and P. Veltri. Coherent structure formation through nonlinear interactions in 2d magnetohydrodynamic turbulence. *Scientific Reports*, 7(1):13849, 2017. 8

[35] C. De Lellis and L. Székelyhidi Jr. The euler equations as a differential inclusion. *Ann. of Math. (2)*, 170:1417–1436, 2009. 1, 7, 21

[36] E. Di Benedetto. $c^{1+\alpha}$ local regularity of weak solutions of degenerate elliptic equations. *Nonlinear Anal.*, 7(8):827–850, 1983. 111

[37] P. H. Diamond and G. G. Craddock. On the alfven effect in mhd turbulence. *Comments Plasma Phys. Control. Fusion*, 16(6):287–297, 1990. 27

[38] M. Do and M. Vetterli. Pyramidal directional filter banks and curvelets. *In Proceedings 2001 International Conference on Image Processing*, 2:158–161, 2001. 86

[39] M. Dobrowolny, A. Mangeney, and P. Veltri. Fully developed anisotropic hydromagnetic turbulence in interplanetary space. *Phys. Rev. Lett.*, 45:144–147, 1980. 7

[40] K. Dragomiretskiy and D. Zosso. Variational mode decomposition. *IEEE Transactions on Signal Processing*, 62(3):531–544, 2014. 86, 89, 90

[41] V. Désangles, E. De Giorgio, G. Bousselin, A. Poyé, M. Moulin, and N. Plihon. Stirring a slightly magnetized plasma column. In *From laboratories to astrophysics: the expanding universe of plasma physics*, Les Huoches, 2017. Poster session. xiv, 81, 95

[42] L. C. Evans. Partial differential equations. In *Graduate studies in Mathematics*, volume 19. American Mathematical Society, 2010. 20, 107, 109

[43] G. L. Eyink. Energy dissipation without viscosity in ideal hydrodynamics i. fourier analysis and local energy transfer. *Physica D: Nonlinear Phenomena*, 78(3):222 – 240, 1994. 1, 21

[44] M. Farge. Wavelet transforms and their applications to turbulence. *Ann. Rev. of Fluid Mech.*, 24(1):395–458, 1992. 35, 49

[45] M. Farge, G. Pellegrino, and K. Schneider. Coherent vortex extraction in 3d turbulent flows using orthogonal wavelets. *Phys. Rev. Lett.*, 87:054501–054505, 2001. 7

[46] M. Farge, K. Schneider, and P. Devynck. Extraction of coherent bursts from turbulent edge plasma in magnetic fusion devices using orthogonal wavelets. *Physics of Plasmas*, 13(4):042304, 2006. 35, 49

[47] M. Farge, K. Schneider, and N. Kevlahan. Non-gaussianity and coherent vortex simulation for two-dimensional turbulence using an adaptive orthogonal wavelet basis. *Physics of Fluids*, 11(8):2187–2201, 1999. 35, 49

[48] R. Feynman, R. Leighton, and M. Sands. *The Feynman lectures in physics, Vol. II.* Addison-Wesley, 1966. 76, 108

[49] E. Foufoula-Georgiou and P. Kumar. *Wavelets in Geophysics*, volume 4. ACADEMIC PRESS, 1994. 35, 40, 49, 51, 52

[50] U. Frisch. *Turbulence: The Legacy of A. N. Kolmogorov*. Cambridge University Press, 1995. xiii, 7, 19, 20, 23, 26, 30, 33

[51] U. Frisch, P.-L. Sulem, and M. Nelkin. A simple dynamical model of intermittent fully developed turbulence. *J. of Fluid Mech.*, 87(4):719–736, 1978. 21

[52] D. Gabor. Theory of communication. *J. of the Inst. of Electrical Engineers, ParIII: Radio and Communication Engineering*, 93(26):429–457, 1946. 87

[53] Y. Gagne. *Contribution à l'étude expérimentale de l'intermittence de la turbulence à petite échelle.* PhD thesis, Université de Grenoble, 1980. xiii, 31

[54] G. P. Galdi. Mathematical problems in classical and non-newtonian fluid mechanics. In G. P. Galdi, A. M. Robertson, R. Rannacher, and S. Turek, editors, *Hemodynamical Flows: Modeling, Analysis and Simulation (Oberwolfach Seminars)*. Birkhäuser Verlag, 2007. 110

[55] S. Ghosh and W. M. Hossain, Matthaeus. The application of spectral methods in simulating compressible fluid and magnetofluid turbulence. *Computer Physics Communications*, 74(1):18–40, 1993. 48

[56] J. Gilles. Empirical wavelet transform. In *IEEE Transactions on Signal Processing*, volume 61, page 3999. IEEE, 2013. 86

[57] C. Gloaguen, J. Léorat, A. Pouquet, and R. Grappin. A scalar model for mhd turbulence. *Physica D: Nonlinear Phenomena*, 17(2):154 – 182, 1985. 7, 24, 25

[58] R. Gonzales, A. Costa, and E. S. Santini. On a variational principle for beltrami flows. *Phs. of Fluids*, 22(7):074102–074102, 2010. 23

[59] R. C. Gonzalez and R. E. Woods. *Digital Image Processing*. Addison Wesley, 1992. 87

[60] R. Grappin. Onset and decay of two dimensional magnetohydrodynamic turbulence with velocity magnetic field correlation. *Phys. Fluids.*, 29(8):2433–2443, 1986. 7, 25

[61] R. Grappin, U. Frisch, A. Pouquet, and J. Leorat. Alfvenic fluctuations as asymptotic states of mhd turbulence. *Astron. Astrophys.*, 105:6–14, 1982. 7, 24

[62] R. Grappin, J. Leorat, and A. Pouquet. Dependence of mhd turbulence spectra on the velocity field-magnetic field correlation. *Astron. Astrophys.*, 126:51–58, 1983. 7, 24

[63] R. Grauer and C. Marliani. Current sheet formation in 3d ideal incompressible magnetohydrodynamics. *Phys. Rev. Lett.*, 84:4850–4853, 2000. 22

[64] A. Grossmann, R. Kronland-Martinet, and J. Morlet. Reading and understanding continuous wavelet transforms. In J. M. Combes, A. Grossmann, and P. Tchamitchian, editors, *Wavelets: Time-Frequency Methods and Phase Space*, pages 2–20. Springer-Verlag, 1989. 35

[65] A. Grossmann and J. Morlet. Decomposition of hardy functions into square integrable wavelets of constant shape. *SIAM J. on Math. Analysis*, 15:723–736, 1984. 36

[66] S. L. Hahn. *Hilbert transforms in signal processing*. Artech House Inc., 1996. 87

[67] G. W. Hammett and F. W. Perkins. Fluid moment models for landau damping with application to the ion-temperature-gradient instability. *Phys. Rev. Lett.,*, 64:3019, 1990. 69

[68] J. P. Hans Goedbloed and S. Poedt. *Principles of Magnetohydrodynamics: With Applications to Laboratory and Astrophysical Plasmas*. Cambridge University Press, 1nd edition, 2004. 9

[69] A. Hasegawa and K. Mima. Pseudo-three-dimensional turbulence in magnetized nonuniform plasma. *Physics of Fluids*, 21:87–92, 1978. 72

[70] M. R. Hestenes. Multiplier and gradient methods. *J. of Optimization Theory and Applications*, 4(5):303–320, 1969. 91

[71] W. Horton. Drift waves and transport. *Rev. Mod. Phys.,*, 71(735), 1999. 72

[72] W. Horton and A. Hasegawa. Quasi-twodimensional dynamics of plasmas and fluids. *Chaos*, 4(227), 1994. 72

[73] T. Y. Hou and Z. Shi. Sparse time-frequency decomposition for multiple signals with same frequencies. *Philos Trans A Math Phys Eng Sci.*, 374(2065):20150192, 2016. 85

[74] N. E. Huang, Z. Shen, S. R. Long, M. C. Wu, H. H. Shih, Q. Zheng, N. C. Yen, C. C. Tung, and H. H. Liu. The empirical mode decomposition and the hilbert spectrum for nonlinear and non-stationary time series analysis. *Proceedings of the Royal Society A: Mathematical Physical and Engineering Sciences*, 454(1971):903–995, 1998. 85

[75] S. Ichimaru. *Statistical Plasma Physics - Volume I: Basic Principles*. Addison-Wesley, Reading, Massachusetts, 1992. 69

[76] S. Ichimaru. *Statistical Plasma Physics - Volume II: Basic Principles*. Addison-Wesley, Reading , Massachusetts, 1992. 69

[77] P. S. Iroshnikov. Turbulence of a conducting fluid in a strong magnetic field. *Sov. Astron.*, 7:566–571, 1964. 28

[78] J. H. Jeans. On the theory of star-streaming and structure of the universe. *Mon. Not. R. Astron. Soc.*, 76:70, 1915. 65

[79] A. N. Kolmogorov. Energy dissipation in locally isotropic turbulence. *Dokl. Akad. Nauk.*, 32:19–22, 1941. 28, 31

[80] A. N. Kolmogorov. The local structure of turbulence in incompressible viscous fluid for very large reynolds numbers. *Dokl. Akad. Nauk.*, 30:299–303, 1941. 27, 31

[81] R. H. Kraichnan. Inertial range spectrum of hydromagnetic turbulence. *The Physics of Fluids*, 8(7):1385–1387, 1965. 28

[82] R. H. Kraichnan. Lagrangian history closure approximation for turbulence. *The Physics of Fluids*, 8(4):575–598, 1965. 27

[83] J. A. Krommes. *Analytical Descriptions of Plasma Turbulence*, chapter 4, pages 115–232. Word Scientific, 2012. 76

[84] P. Kumar and E. Foufoula-Georgiou. A multicomponent decomposition of spatial rainfall fields: 1. segregation of large and small scale features using wavelet transforms. *Water Resources Research*, 29(8):2515–2532, 1993. 40

[85] T. Kuusi and G. Mingione. Universal potential estimates. *J. Funct. Anal.*, 262(10):4205–4269, 2012. 111

[86] T. S. Lee. Image representation using 2d gabor wavelets. *IEEE Transactions on Pattern Analysis and Machine Intelligence*, 18(10):959–971, 1994. 86

[87] G. M. Lieberman. Boundary regularity for solutions of degenerate elliptic equations. *Nonlinear Anal.*, 12(11):1203–1219, 1988. 111

[88] J. Málek, J. Nečas, M. Rokyta, and M. Ružička. Weak and measure-valued solutions to evolutionary pdes. *1997*, 10(1):109–111., Journal of Applied Mathematics and Stochastic Analysis. 110

[89] J. Málek, J. Nečas, and M. Ružička. On the non-newtonian incompressible fluids. *Math. Models Methods Appl. Sci.*, 3:35–63, 1993. 110

[90] L. Mahrt. Eddy asymmetry in the sheared heated boundary layer. *J. Atmos. Sci.*, 48:472–492, 1991. 40

[91] S. G. Mallat. Multiresolution approximations and wavelet orthonormal bases of $L^2(\mathbb{R})$. *Trans. Amer. Math. Soc.*, 315:69–87, 1989. 40

[92] S. G. Mallat. A theory for multiresolution signal decomposition: the wavelet representation. *IEEE Transactions on Pattern Analysis and Machine Intelligence*, 11(7):674–693, 1989. 36

[93] W. Matthaeus and D. Montgomery. *Statistical Physics and Chaos in Fusion Plasmas*. C. W. Horton, Jr. and L. E. Reichl, Wiley, New York, 1984. 7, 24

[94] W. H. Matthaeus. Reconnection in two dimensions: Localization of vorticity and current near magnetic x-points. *Geophysical Research Letters*, 9(6):660–663, 1982. 22

[95] W. H. Matthaeus, M. L. Goldstein, and D. C. Montgomery. Turbulent generation of outward-traveling interplanetary alfvénic fluctuations. *Phys. Rev. Lett.*, 51:1484–1487, 1983. 7

[96] W. H. Matthaeus, A. Pouquet, P. D. Mininni, P. Dmitruk, and B. Breech. Rapid alignment of velocity and magnetic field in magnetohydrodynamic turbulence. *Phys. Rev. Lett.*, 100:085003, 2008. 7, 25

[97] W. H. Matthaeus, W. T. Stribling, D. Martinez, S. Oughton, and D. Montgomery. Selective decay and coherent vortices in two-dimensional incompressible turbulence. *Phys. Rev. Lett.*, 66:2731–2734, 1991. 23

[98] W. M. Matthaeus and S. L. Lamkin. Turbulent magnetic reconnection. *The Physics of Fluids*, 29(8):2513–2534, 1986. 22, 47

[99] S. Meignen and V. Perrier. A new formulation for empirical mode decomposition based on constrained optimization. *IEEE Signal Processing Letters*, 14(12):932–935, 2007. 85

[100] M. Meneguzzi, U. Frisch, and A. Pouquet. Helical and nonhelical turbulent dynamos. *Phys. Rev. Lett.*, 47:1060–1064, 1981. 7, 24

[101] C. Meneveau. Analysis of turbulence in the orthonormal wavelet representation. *J. of Fluid Mech.*, 232:469–520, 1991. 35, 36, 37, 38, 49

[102] C. Mercuri, G. Riey, and B. Sciunzi. A regularity result for the p-laplacian near uniform ellipticity. *Siam J. Math. Anal.*, 48(3):2059–2075, 2016. 109, 112

[103] Y. Meyer. Orthonormal wavelets. In J. Combes, A. Grossmann, and P. Tchamitchian, editors, *Wavelets: Time-Frequency Methods and Phase Space*, pages 21–37. Springer Berlin Heidelberg, 1989. 40

[104] G. Mingione. Regularity of minima: an invitation to the dark side of the calculus of variations. *Applications of Mathematics*, 51(4):355–426, 2006. 109, 112

[105] G. Mingione. The calderon-zygmund theory for elliptic problems with measure data. *Ann. Scuola Norm. Sup. Pisa Cl. Sci. (5)*, 6:195–261, 2007. 109, 112

[106] H. K. Moffatt. Magnetostatic equilibria and analogous euler flows of arbitrarily complex topology. part 1. fundamentals. *J. Fluids Mech.*, 159:359–378, 1985. 7

[107] V. A. Morozov. Linear and nonlinear ill-posed problems. *Journal of Mathematical Sciences*, II(6):706–736, 1975. 87

[108] G. Nigro and V. Carbone. Finite-time singularities and flow regularization in a hydromagnetic shell model at extreme magnetic prandtl numbers. *New J. of Phys.*, 17(7):073038, 2015. 7

[109] J. Nocedal and S. Wright. *Numerical optimization*. Springer, Berlin, 2nd edition, 2006. 90

[110] J. Nunes, Y. Bouaoune, E. Delechelle, O. Niang, and P. Bunel. mage analysis by bidimensional empirical mode decomposition. *Image and Vision Computing*, 21(12):1019–1026, 2003. 85

[111] A. Obukhov. On the distribution of energy in the spectrum of turbulent flow. *Izv. Akad. Nauk. SSSR, Ser. Geofiz.*, 5(4-5):453–466, 1941. 25, 27

[112] N. Okamoto, K. Yoshimatsu, K. Schneider, and M. Farge. Small-scale anisotropic intermittency in magnetohydrodynamic turbulence at low magnetic reynolds numbers. *Phys. Rev. E*, 89:033013–033023, 2014. 35, 49

[113] S. Oldenbürger, C. Brandt, F. Brochard, N. Lemoine, and G. Bonhomme. Spectroscopic interpretation and velocimetry analysis of fluctuationsin a cylindrical plasma recorded by a fast camera. *Rev. Sci. Instrum.*, 81(063505):1–7, 2010. 96

[114] L. Onsager. Statistical hydrodynamics. *Il Nuovo Cimento Series 9*, 6(2 Supplement):279–287, 1949. 1, 7, 20, 21, 57

[115] G. Parisi and U. Frisch. *On the singularity structure of fully developed turbulence*, pages 84–87. North-Holland, 1985. 7

[116] J. C. Perez, J. Mason, S. Boldyrev, and F. Cattaneo. On the energy spectrum of strong magnetohydrodynamic turbulence. *Phys. Rev. X*, 2(4):041005, 2012. 29

[117] N. Plihon, G. Bousselin, F. Palermo, J. A. Morales, W. Bos, F. S. Godeferd, M. Bourgoin, J. Pinton, M. Moulin, and A. Aanesland. Flow dynamics and magnetic induction in the von-kármán plasma experiment. *J. Plasma Phys.*, 81(1), 2015. 80

[118] H. Politano, A. Pouquet, and P. Sulem. Inertial ranges and resistive instabilites in two dimensional magnetohydrodynamic turbulence. *Phys. Fluids B: Plasma Phys.*, 1(12):2330–2339, 1989. 22

[119] H. Politano, A. Pouquet, and P. Sulem. Current and vorticity dynamics in three dimensional magnatohydrodynamic turbulence. *Phys. of Plasma*, 2(8):2931–2939, 1995. 22

[120] A. Pouquet, M. Meneguzzi, and U. Frisch. Growth of correlations in magnetohydrodynamic turbulence. *Phys. Rev. A*, 33:4266–4276, 1986. 7, 25

[121] P. Pucci and J. Serrin. *The maximum principle*. Birkhauser, Boston, 2007. 113, 120

[122] K. R. Rajagopal. Mechanics of non-newtonian fluids. In G. P. Galdi and J. Nečas, editors, *Recent Developments in Theoretical Fluid Mechanics*, page 129–162. Research Notes in Mathematics Series, 291, Longman, 1993. 110

[123] R. Ricca. Nato science series ii. In R. Ricca, editor, *An Introduction to the Geometry and Topology of Fluid Flows*, volume 47, page 347. Springer Netherlands, 2001. 23

[124] L. F. Richardson. Atmospheric diffusion shown on a distance neighbour graph. *Proc. R. Soc. London A*, 110:709–737, 1922. 26

[125] G. Rilling and P. Flandrin. Sampling effects on the empirical mode decomposition. *Advances in Adaptive Data Analysis*, 01(01):43–59, 2009. 85

[126] R. T. Rockafellar. A dual approach to solving nonlinear programming problems by unconstrained optimization. *Mathematical Programming*, 5(1):354–373, 1973. 91

[127] V. Scheffer. An inviscid flow with compact support in space-time. *The Journal of Geometric Analysis*, 3(4):343–401, 1993. 21

[128] C. Schröder. *Experimental investigations on drift waves in linear magnetized plasmas*. PhD thesis, Ernst-Moritz-Arndt-Universität Greifswald, 2003. 97

[129] B. Sciunzi. Some results on the qualitative properties of positive solutions of quasilinear elliptic equations. *NoDEA. Nonlinear Differential Equations and Applications*, 14(3-4):315–334, 20078. 109, 112

[130] B. Sciunzi. Regularity and comparison principles for p-laplace equations with vanishing source term. *Comm. Cont. Math.*, 16(6):1450013, 20, 2014. 109, 112

[131] S. Servidio, W. H. Matthaeus, and V. Carbone. Ergodicity of ideal galerkin three-dimensional magnetohydrodynamics and hall magnetohydrodynamics models. *Phys. Rev. E*, 78:046302, 2008. 15

[132] S. Servidio, W. H. Matthaeus, and P. Dmitruk. Depression of nonlinearity in decaying isotropic mhd turbulence. *Phys. Rev. Lett.*, 100:095005, 2008. 7, 25

[133] S. Servidio, W. H. Matthaeus, M. A. Shay, P. Dmitruk, P. A. Cassak, and P. A. Wan. Statistics of magnetic reconnection in two-

dimensional magnetohydrodynamic turbulence. *Phys. of Plasma*, 17:032315, 2010. 48

[134] J. P. Sheehan and N. Hershkowitz. Emissive probes. *Plasma Sources Science and Technology*, 20(6):063001, 2011. 83

[135] A. Shnirelman. Weak solutions with decreasing energy of incompressible euler equations. *Communications in Mathematical Physics*, 210(3):541–603, 2000. 20

[136] T. H. Stix. *Waves in Plasmas*. Am. Inst, of Phys., New York, 1992. 70

[137] T. Stribling and W. H. Matthaeus. Relaxation processes in a low-order three-dimensional magnetohydrodynamics model. *Physics of Fluids B: Plasma Physics*, 3(8):1848–1864, 1991. 7

[138] P. Tavallali, T. Y. Hou, and Z. Shi. Extraction of intrawave signals using the sparse time-frequency representation method. *Multiscale Modeling and Simulation*, 12(4):1458–1493, 2014. 85

[139] E. Teixeira. Regularity for quasilinear equations on degenerate singular sets. *Math. Ann.*, 358(1-2):241–256, 2014. 111

[140] A. N. Tichonov. Solution of incorrectly formulated problems and the regularization method. *Soviet Mathematics*, 4:1035–1038, 1963. 87

[141] A. Ting, W. H. Matthaeus, and D. Montgomery. Turbulent relaxation processes in magnetohydrodynamics. *The Physics of Fluids*, 29(10):3261–3274, 1986. 7, 15, 25, 48

[142] P. Tolksdorf. Regularity for a more general class of quasilinear elliptic equations. *J. Differential Equations*, 51(1):126 – 150, 1984. 111

[143] G. R. Tynan, A. Fujisawa, and G. McKee. A review of experimental drift turbulence studies. *PLasma Phys. Contro. Fusion*, 51(113001), 2009. 72, 77

[144] M. K. V. Statistical theory of magnetohydrodynamic turbulence: recent results. *Phys. Rep.*, 401:229–380, 2004. 29

[145] P. Veltri, V. Carbone, F. Lepreti, and G. Nigro. Self organization in magnetohydrodynamic turbulence. In R. A. Meyers, editor, *Encyclopedia of Complexity and Systems Science*, pages 8009–8028. Springer New York, 2009. 7, 23, 24, 25

[146] K. M. Watson. Use of boltzmann equation for the study of ionized gases of low density 1. *Phys. Rev.*, 102:12, 1956. 65

[147] N. Wiener. *Extrapolation, Interpolation, and Smoothing of Stationary Time Series*. MIT Press Ltd, 1949. 87

[148] M. Yamada and K. Ohkitani. Orthonormal wavelet analysis of turbulence. *Fluid Dynamics Research*, 8(1-4):101, 1991. 40

[149] T. Yamada and et all. Anatomy of plasma turbulence. *Nature physics*, 4, 2008. 97

[150] K. Yoshimatsu and et all. Wavelet-based coherent vorticity sheet and current sheet extraction from three-dimensional homogeneous magnetohydrodynamic turbulence. *Physics of Plasmas*, 16(8):082306, 2009. 35, 49

[151] K. Yoshimatsu, K. Schneider, N. Okamoto, Y. Kawahara, and M. Farge. Intermittency and geometrical statistics of three-dimensional homogeneous magnetohydrodynamic turbulence: A wavelet viewpoint. *Physics of Plasmas*, 18(9):092304, 2011. 7, 35, 49

[152] P. J. Zandbergen and D. Dijkstra. von-kármán swirling flows. *Annu. Rev. Fluid Mech.*, 19(465), 1987. 79

[153] D. Zosso, K. Dragomiretskiy, A. L. Bertozzi, and P. S. Weiss. Two-dimensional compact variational mode decomposition. *J. of Math. Imaging and Vision*, 58(2):294–320, 2017. 85, 86, 90